GEM TN-92-199

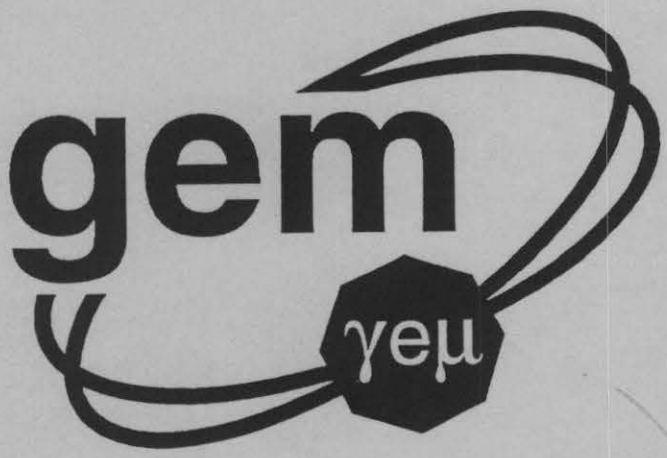

The GEM Muon System Based on Cathode Strip Chambers

Beijing Institute for High Energy Physics
Boston University
Brookhaven National Laboratory
Draper Laboratory
Hofei University
Institute for Theoretical and Experimental Physics, Moscow
Joint Institute of Nuclear Research/Dubna
Minsk Institute of Nuclear Problems
Oak Ridge National Laboratory
Princeton University
St. Petersburg Nuclear Physics Institute
SSC Laboratory, Dallas
State University of New York at Stony Brook
Tsinghua University
University of Houston

September 28, 1992

Abstract:

This document proposes to show that the Cathode Strip Chambers (CSC) Technology represents the best choice for the GEM muon system.

THE GEM MUON SYSTEM

BASED ON CATHODE STRIP CHAMBERS

GEM Muon System CSC participants:
Beijing Institute for High Energy Physics
Boston University
Brookhaven National Laboratory
Draper Laboratory
Hofei University
University of Houston
ITEP, Moscow
JINR/Dubna
Minsk Institute of Nuclear Problems
Oak Ridge National Laboratory
Petersburg Nuclear Physics Institute
Princeton University
SSC Lab, Dallas
SUNY Stony Brook
Tsinghua University

28 September 1992

TABLE OF CONTENTS

1. Introduction

1.1 Overview

In this document we show that Cathode Strip Chamber (CSC) technology represents the best choice for the GEM muon system. This chapter includes a review of the main requirements for that system, a brief description of the principle of operation of CSC's, an overview of the baseline system layout, and a summary of the reasons that have led us to conclude that CSC's are in fact the best option. Chapters 2 through 5 provide additional detail on the mechanical design of the chambers, the readout electronics, the alignment system, and the expected system performance. In chapters 6 and 7, we discuss the practical issues of cost and manufacture.

1.2 Requirements

The muon system for GEM must

- Provide a precision coordinate measurement in the muon's bend direction with a precision of 100 μm in the barrel and 75 μm in the endcaps.
- Provide a mechanism for monitoring global alignment to a precision of 25 μm
- Determine the non-bend coordinate (z in the barrel, r in the endcaps) with a resolution at the few cm level.
- Provide Level 1 trigger information with sufficiently fine spatial granularity to identify muons with transverse momenta up to 50 GeV/c and sufficiently good timing resolution to allow assignment of a given signal to the correct proton bunch crossing.
- Be of a design compatible with economical mass-production techniques.

Cathode strip chambers meet these requirements in the endcap *and* the barrel regions through the application of a single technology.

1.3 CSC Principle of Operation

The basic construction of a CSC is that of a conventional wire chamber. However, rather than reading the anode wires, a position coordinate measurement is obtained by determining the center-of-gravity of the charge distribution induced on a segmented strip cathode. By orienting the strips at right angles to the anode wires, the mean position of the charge distribution can vary in a continuous way, permitting a precise determination of the particle's position of incidence. For example, with a cathode strip pitch of 5 mm and a signal-to-noise ratio of order 100:1, position resolutions in the range 50--100 μm are obtainable. Although far less precise, the resolution of the anode wires is more than adequate for the orthogonal (non-bend) coordinate readout. It is also possible to measure the second coordinate using coarse strips oriented parallel to the wires etched on the cathodes opposite to those used for the precision measurement.

1.4 Baseline System Layout

Figures 1.1 and 1.2 show the layout of the CSC barrel system. We have chosen a 32-fold azimuthal segmentation so as to minimize the degradation in resolution resulting from non-normal angles of incidence. The chambers of the middle and outer superlayers are tilted by 8 and 11 degrees, respectively. This reduces the Lorentz-angle effect on resolution, as discussed in GEM TN-92-137. Figure 1.3 shows a layout for the endcap region. Although figure 1.4 shows a "4/4/4" configuration—i.e. a configuration with four chambers in each superlayer—recent studies have led us to choose an 8/4/4 configuration throughout the barrel and endcap regions.

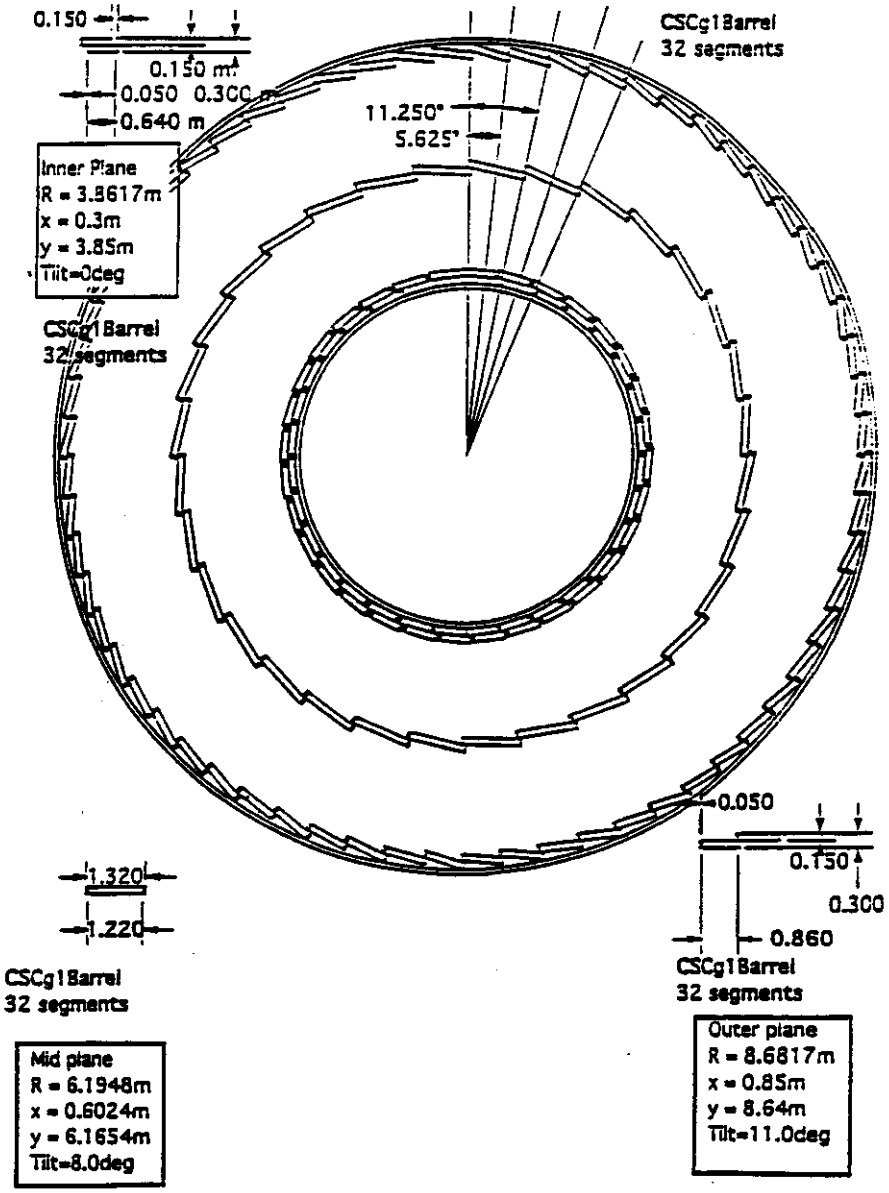

Figure 1.1 End (x-y) view of the barrel CSC system.

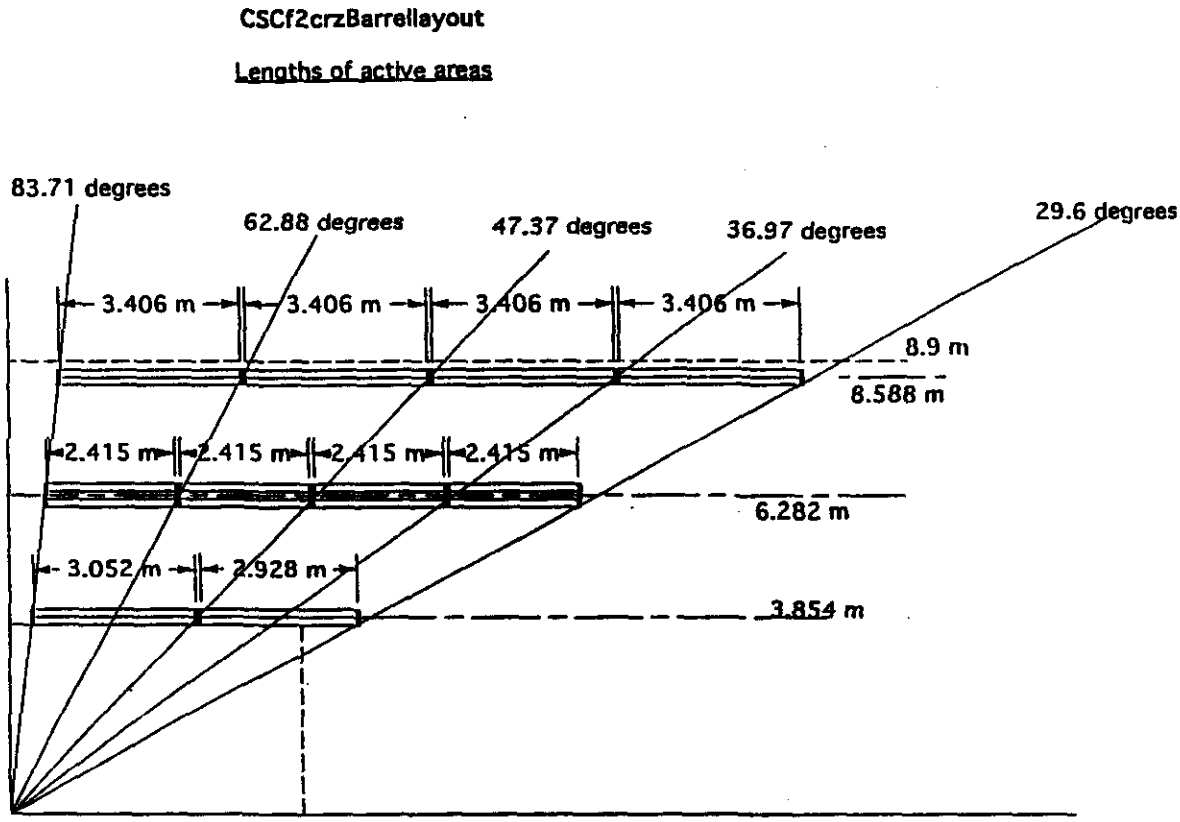

Figure 1.2 Side (r-z) view of the barrel CSC system.

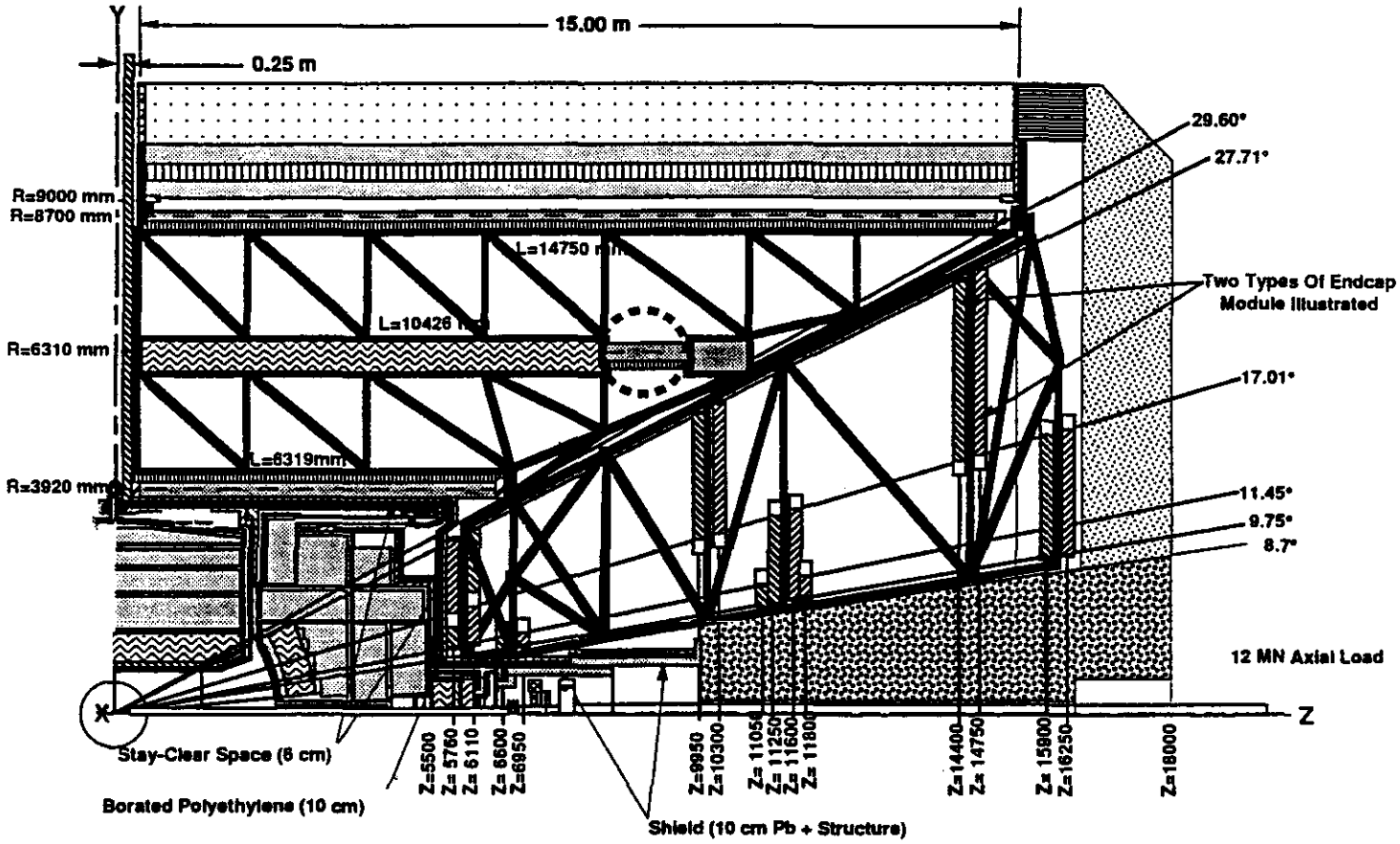

GEM MUON SYSTEM (BASELINE)

With Baseline LAr Calorimeter Illustrated

Figure 1.3 Side (r-z) view of the endcap CSC system.

Dimensional and channel count data for the barrel and endcap systems are tabulated in tables 1.1 and 1.2, respectively. Altogether there are 1050 K cathode strip readout channels, 30% of which are in the endcaps. In addition there are 160 K anode (or coarse-cathode) readout channels.

Table 1.1 Dimensional and channel count data for the barrel CSC system.

1/2 Barrel = 32 segments
1 precise channel (φ) = 5 mm
1 coarse channel (Z) = 100 mm

Inner Layer: Type A and Type B
Middle Layer: Type C
Outer Layer: Type D

	A	B	C	D
Sensitive Area mm × mm	640 × 3,052	640 × 2,928	1,220 × 2,415	860 × 3,406
Outside dimensions mm × mm	740 × 3,152	740 × 3.028	1,320 × 2,515	960 × 3,506
N Chambers in sector	2	2	4	8
N Chambers in barrel	128	128	256	512
Total sensitive area M^2	250	240	850	1500
N precise channels in chamber	512	512	1,024	704
N coarse channels in chamber	120	116	96	136
Total N precise channels	65,536	65,536	262,144	360,448
Total N coarse channels	15,360	14,848	24,576	69,632

Total Number of 4-gap chambers: 1,024
Total sensitive area of 4-gap chambers: 2,840m^2
Total Number of precise channels: 753,664
Total Number of coarse channels: 124,416

Table 1.2 Dimensional and channel count data for the endcap CSC system.

Endcap CSC Layout — Open Magnet Geometry
Structure at 10.5° and 28.45°; active coverage 9.75° to 27.71° — 9/27/92
module border (nonreadout) 10 cm; module thickness 20 cm; intermodule space 15 cm — SW

Nsectors= 16
wires ganged by 20 = 5.00 cm
Strip width at middle = 5.00 mm

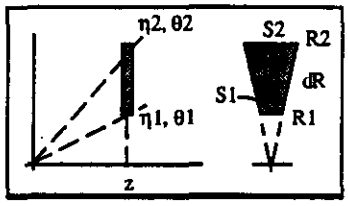

Configuration: number of planes in 1st / 2nd / 3rd module
8 / 8 / 4 for eta > 2.3
8 / 4 / 4 elsewhere

Nomenclature
Note: modules (a) occupy even-numbered sectors
modules (b) occupy odd-numbered sectors

Total channel counts:

	z	η1	θ1	η2	θ2	R1	R2	dR	S1	S2	area	# strips	strip occ	# r-chans	# strip chan	# r-chan	wt/mod
	m		deg		deg	m	m	m	m	m	m^2	/pl/sctr	/sec	/pl/sctr			Kg
Inner modules																	
1a)	5.76	2.30	11.45	1.90	17.01	1.17	1.76	0.60	0.46	0.69	0.33	114	98	12	14629	1,525	25
1b)	6.11	2.30	11.45	1.90	17.01	1.24	1.87	0.63	0.48	0.73	0.38	121	104	13	15518	1,618	27
2a)	6.11	1.90	17.01	1.40	27.71	1.87	3.21	1.34	0.73	1.25	1.30	198	36	27	25361	3,428	65
2b)	5.76	1.90	17.01	1.40	27.71	1.76	3.02	1.26	0.69	1.18	1.16	187	34	25	23909	3,231	59
3a)	6.60	2.46	9.75	2.30	11.45	1.13	1.34	0.20	0.44	0.52	0.10	96	103	4	12339	520	14
3b)	6.95	2.46	9.75	2.30	11.45	1.19	1.41	0.21	0.47	0.55	0.11	102	108	4	12993	548	14
Middle modules																	
4a)	11.25	2.46	9.75	1.90	17.01	1.93	3.44	1.51	0.75	1.34	1.55	210	77	30	13422	1,933	75
4b)	11.60	2.46	9.75	1.90	17.01	1.99	3.55	1.56	0.78	1.38	1.65	216	80	31	13839	1,993	78
5a)	9.95	1.90	17.01	1.40	27.71	3.04	5.23	2.18	1.19	2.04	3.45	323	13	44	20650	2,791	144
5b)	10.30	1.90	17.01	1.40	27.71	3.15	5.41	2.26	1.23	2.11	3.70	334	14	45	21377	2,889	153
8a)	11.05	2.46	9.75	2.30	11.45	1.90	2.24	0.34	0.74	0.87	0.27	161	39	7	10329	435	23
8b)	11.80	2.46	9.75	2.30	11.45	2.03	2.39	0.36	0.79	0.93	0.31	172	41	7	11030	465	25
Outer modules																	
6a)	15.90	2.46	9.75	1.90	17.01	2.73	4.87	2.13	1.07	1.90	3.10	296	36	43	18969	2,731	132
6b)	16.25	2.46	9.75	1.90	17.01	2.79	4.97	2.18	1.09	1.94	3.24	303	37	44	19387	2,791	137
7a)	14.40	1.90	17.01	1.40	27.71	4.41	7.56	3.16	1.72	2.95	7.23	467	6	63	29886	4,039	275
7b)	14.75	1.90	17.01	1.40	27.71	4.51	7.75	3.23	1.76	3.02	7.58	478	7	65	30612	4,137	287
													Total =>		294251	35,075	24,536

total area of strip cathodes (m^2) 2484
total volume of chambers (m^3) 12.4
Total number of modules 352

1.5 Beneficial Features of CSC's

Resolution

The instrinsic position resolution capabilities of the CSC technique greatly exceed the requirements of GEM. For example, using a xenon-isobutane gas mixture and cathode readout elements consisting of six cathode wires spaced by 500 μm , Charpak et al (see NIM 148 (1978)471) obtained 35 μm resolution for 1.5 KeV x-rays . In beam tests resolutions in the 70–80 μm range were measured by L.S. Barabash et al, (see NIM A236 (1985)271) and A. Korytov et al (to be published). In chapter 2 we show that the resolution expected for devices suitable for GEM is 75 μm.

Alignment

The inherent precision of the CSC's comes from the lithographic process used in the etching of the cathode strips. With this technique the strips can be internally aligned with a global precision of 20 μm. Moreover, the cathode-plane printed circuit boards can be made stiff through the use of HEXCEL plane supports. Global alignment data are obtained via a single transfer from the measurement strips to survey marks photoetched on the planes and made visible to the external alignment system. The structure of the cathode planes allows for the use of several alignment technologies including LED-lens and floating wire.

Non-bend Coordinate Measurement

By reading the anode wires, or by reading signals from coarsely segmented cathode strips oriented parallel to the wires, the required non-bend coordinate resolution of 10 cm can be achieved without introducing additional detector layers.

Triggering

Fast timing and position information for use in the Level 1 trigger can be extracted from the CSC's in a natural way using simple electronics.

Although simulations indicate that at standard luminosity of 10^{33} cm^{-2} s^{-1} muon P_T thresholds in the 10–20 GeV/c range will suffice, the ability to set higher P_T thresholds provides design margin, which could be of particular importance for running at high luminosity. The 5 mm cathode strip pitch is more than sufficient to define transverse momentum thresholds of up to 50 GeV/c.

The combination of a fast gas (e.g. 50% CO_2-50% CF_4) and closely spaced anode wires results in a maximum drift time of about 25 nsec. Simulations indicate that by selecting the earliest arrival of signals from the four layers of a given superlayer, the timing of 99% of all tracks is determined to within 12 ns.

Two-Track Resolution

The CSC's remain viable in the presence of two-track backgrounds. Studies show (see chapter 2) that the spatial resolution remains below the specified 100 μm level for two-track separations as small as 7.5 mm. For smaller separations, the resolution degrades but always remains below 450 μm. Moreover, by analysing the higher moments of the induced charge distribution, it is possible to detect the presence of a second track to separations as small as 1 mm. Thus one can eliminate spurious data points from tracks at the hit level.

Rate Handling Capability

The large number of channels in the CSC system results in excellent rate-handling capability. Specifically, with shaping times of 300 ns the readout electronics can handle rates of up to 75 kHz, which for the 300 x 0.5 cm 2 strips employed in the barrel region corresponds to a detected particle fluence of 500 cm^{-2} s^{-1}. We note that this rate represents a serious challenge to any of the technologies thus far discussed for GEM. In the endcaps where the strips are smaller even higher larger fluences can be accomodated.

Aging

CSC's operating in proportional mode will have excellent longevity. Assuming a detected particle fluence of 500 cm^{-2} s^{-1}, and a gas gain of 2 x 10^4, the total integrated current drawn by 1 cm of anode wire in 10 SSC-years will be .004 C. This is well within accepted limits for wire-chamber aging.

Simplified Gas Handling

A number of aspects of the CSC design reduce the requirements placed on the gas handling and delivery system. In particular, the center-of-gravity readout is insensitive to moderate changes in gain or drift velocity brought about by changing gas composition or variations in temperature. Moreover, with CSC's the active volume to be filled with gas is over five times smaller than the volume required for drift technologies.

Industrial Production

The measurement precision of CSC's derives from a single component—i.e. the cathode planes. These important components can be mass-produced in industry. The remainder of the fabrication and assembly steps are well within the capabilities of traditional high-energy physics facilities. These two considerations ensure that the approximately 3500 m^2 of four-gap CSC area can be assembled and tested in a timely and controlled fashion.

Single Technology Solution

As noted, CSC technology meets the requirements of the GEM muon system in both the barrel and the endcap regions. Moreover, the need for a second coordinate readout and the need to produce information for the Level 1 trigger can be met without the introduction of additional detectors and without the addition of complicated electronics. This will allow GEM to focus its manpower and material resources by reducing the scope of the muon R&D program to the greatest possible extent.

1.6 Outstanding Issues

As with any technology, there are a number of causes for concern. These include the large number of electronic channels (approximately 1.2 M in total) and the limited experience with CSC devices of this size. The channel count is mainly a question of cost. As discussed in chapter 3, the per-channel cost can be reduced to an acceptable level by taking full advantage of custom integrated circuits, modern production techniques, and economies of scale.

Although direct experience with large CSC type devices is limited, there is a considerable body of experience with cathode readout devices of more modest dimensions. Moreover, despite its relatively recent start, the contingent of the GEM R&D effort working towards a barrel-size module is well along in its work. Specifically, large cathode planes have been etched and delivered to BNL and Dubna, wires have been strung, and the chambers are in the final stages of assembly. Finally we note that in addition to the GEM R&D efforts there is a vigorous R&D effort at CERN (e.g. by H. Van de Graaf).

2. CSC Design Parameters and Optimization

2.1 Cathode Strip Chambers — Design Parameters and Chamber Construction

2.1.1 Introduction

This section will start with a discussion of the chamber parameters and their effect on performance and an analysis of some of the processes limiting chamber resolution. Many of these issues are common to both the barrel and the endcap chambers; differences for the two regions will be addressed where appropriate. Following the parameter analysis there is a description of chamber construction to realize the optimal parameters in an affordable and constructable design. Issues of chamber manufacturing — production plans, quality assurance, scheduling, etc — are addressed in section 6.

Satisfactory performance could be achieved through several different realizations of the cathode strip concept. The designs presented here are one approach; further work will be necessary to determine the relative merits of different options for chamber construction. Alternative designs are discussed at various points in the text and in a concluding section.

2.1.2 Basic cell parameters, field calculations, some useful formulae

The Cathode Strip Chambers (CSC) are fundamentally multiwire proportional chambers operating on the same principles as those widely in use not only in high energy physics experiments but also in a variety of other fields such as X-ray crystalography, astrophysics and medical imaging. A schematic diagram of a multiwire proportional chamber is shown in Figure 2.1 where its basic parameters are indicated. In a conventional symmetric chamber the two cathodes are located at a distance h which is usually~3s where s is the anode wire pitch. In such a chamber the wires are read out to obtain position information in a direction normal to the direction of the anode wires. In the case of the cathode strip readout, E. Gatti et al. have shown that optimum spatial resolution obtained by interpolation of the induced charge is achieved when $h/s=1$[1].

In order to understand and optimize the performance of the CSCs a detailed Monte Carlo simulation progrma has been written. This program generates minimum ionizing tracks in a chamber of a given geometry. It produces the primary ionization electrons consistent with the operating gas. It simulates the avalanche multiplication process and calculates the charge induced by the avalanche on the strip cathodes. An appropriate charge interpolation algorithm can then be applied in order to study the spatial resolution of the chamber. The following effects influencing the spatial resolution have been included:

- Electronic noise contribution.
- Channel-to-channel intercalibration.
- Diffusion of the electrons.
- Range of δ–electrons.

- The Lorentz effect.
- The differential non-linearity
- The effect of anode wires that are not at right angles with respect to the cathode strips (relevant only for application of the CSCs in the Endcaps).

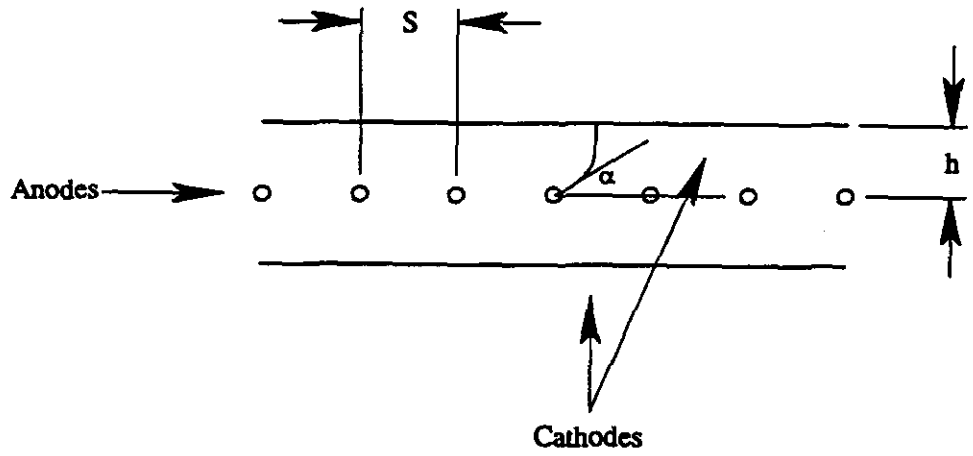

Fig. 2.1 Schematic diagram of a multiwire proportional chamber

In the remaining of this section the underlying principles of the CSC operation are reviewed along with the mathematical tools used in the Monte Carlo simulation and the calculation of the operating parameters of the current CSC design. Values of parameters are summarized in a table at the end of this section.

To calculate the electric field components and other parameters useful for the understanding of the operation of the CSCs we use the Weber approximation[2] as described in the monograph by E. Mathieson[3]. This approximation is generally valid when

$$r_a << s \text{ and } \cosh \frac{2\pi h}{s} >> 1$$

where r_a is the radius of the anode wires. For the cathode charge distributions the parametrization of E. Gatti et al.[4] is used as described later in this section. The potential function $Pw(x,y)$ at a given point x,y of the chamber is given by:

$$Pw(x,y) = 1 - C1n\frac{2(\cosh 2\pi y/s - \cos 2\pi x/s)}{(2\pi r_a/s)^2}$$

where the anodes are assumed at unit potential, the cathodes at ground, and C is defined, in analogy to the formula for the case of cylindrical geometry, as

$$C = 1/1n\,(r_c/r_a)^2$$

and

$$r_c = (s / 2\pi)e^{\pi h/s}$$

where r_c can be considered as the effective radius of a cylindrical cell approximating a cell in the planar geometry. Then the capacitance of an anode wire per unit length, C_1, is given by:

$$C_1 = 4\pi\varepsilon_0 C$$

Partial differentiation of Pw(x,y) yields the electric field components:

$$Ex = -\frac{V_a \partial P_w}{\partial_x} = 2CVa\frac{\pi}{s}\frac{\sin 2\pi x / s}{\cosh 2\pi y / s - \cos 2\pi x / s}$$

$$Ey = -\frac{V_a \partial P_w}{\partial y} = 2CVa\frac{\pi}{s}\frac{\sin 2\pi y / s}{\cosh 2\pi y / s - \cos 2\pi x / s}$$

the equation for the field lines is:

$$\tanh / s = \tan \pi x / s \tan \alpha$$

where α is defined in Figure 2.1.

2.1.3 Gas Gain

The avalanche multiplication in wire chambers is a rather complex phenomenon with no simple description. Knowledge of its dependence on chamber parameters is, however, quite useful in optimizing the detector design. There exist several empirical formulae that describe the chamber's gas gain accurately enough for this purpose. They differ primarily on the choice for the parametrization of the Townsend first ionization coefficient, α, as a function of the electric field, E, and the gas pressure, p. For the Monte Carlo simulation we used the following empirical formula developed by Zastawny[4] for a coaxial counter:

$$1nM = 2CV_a B\left[1n(r_0 / r_a) - 1 + r_a / r_0\right]$$

where

$$r_0 = 2CV_a / pS_0$$

is the radius at which the avalanche starts. V_a is the anode potential in kV, p the gas pressure pS_0 = 52.4 kV/cm in Torr, and B, and S_0 are gas constants determined experimentally. This formula also $M = 5 \times 10^4$, V_a = 3.4 kV applies to multiwire proportional chambers if one uses C as defined above.

2.1.4 Cathode Charge Distribution

The knowledge of the cathode charge distribution for a given chamber geometry is essential in determining the chamber parameters for optimum spatial resolution. It is convenient to express the

induced charge distributions in terms of the variable $\lambda=x/h$ where x is the coordinate along the anode wire direction (which is the direction of charge interpolation). Furthermore the distribution is normalized to the total anode charge q_a. Then one can write

$$\Gamma(\lambda,t) = \rho(\lambda,t) / q_a(t)$$

Since the total charge induced on either cathode is 1/2 of the total anode charge, one has the constraint:

$$\int_{-\infty}^{+\infty} \Gamma(\lambda) d\lambda = \frac{1}{2}$$

Although the induced charge distributions can be calculated exactly, in practical applications one uses average, time independent distributtions[5] which adequately described the distributions observed in chambers of various geometries. For our Monte Carlo studies we have used the single parameter formula developed by E. Gatti et al.[5]:

$$\Gamma(\lambda) = K1 \frac{1 - \tanh^2 K_2 \lambda}{1 + K_3 \tanh^2 K_2 \lambda}$$

The constants K_2, K_3 can be expressed in terms of K_1 using the constraint 4 and the empirical formula[6]

$$K_2 = \frac{\pi}{2}(1 - \frac{1}{2} K_3^{1/2})$$

This expression was derived by examining a variety of chambers with different geometries. K_3 is a function of the chamber geometry. It depends on the ratios r_a/s and h/s. For our design K_3 = 0.53. Figure 2.2 shows the calculated cathode charge distribution for the parameters of the prototype.

Values for the cell parameters are chosen taking into account the required performance in time and position measurement and recognizing practical mechanical constraints. For our current studies we are using a wire pitch $s = 2.5$ mm, a half gap h=2.5 mm, and an anode radius r_a=0.015mm. These choices yield an effective cathode radius (for the equivalent cylindrical cell) of 9.2mm and a capacitance per wire of C_1=8.7pf/m. Using the mobility of CO_2 ions, 1.09cm^2/v-sec, we then have a characteristic time of $t_0 \sim 2$ns. The fraction of total charge collected is 20% for 30 ns peaking time appropriate for the anode readout and fast cathode pickoffs, and 40% or 50% respectively for 300 ns or 1 μsec integration for the cathode strip readout.

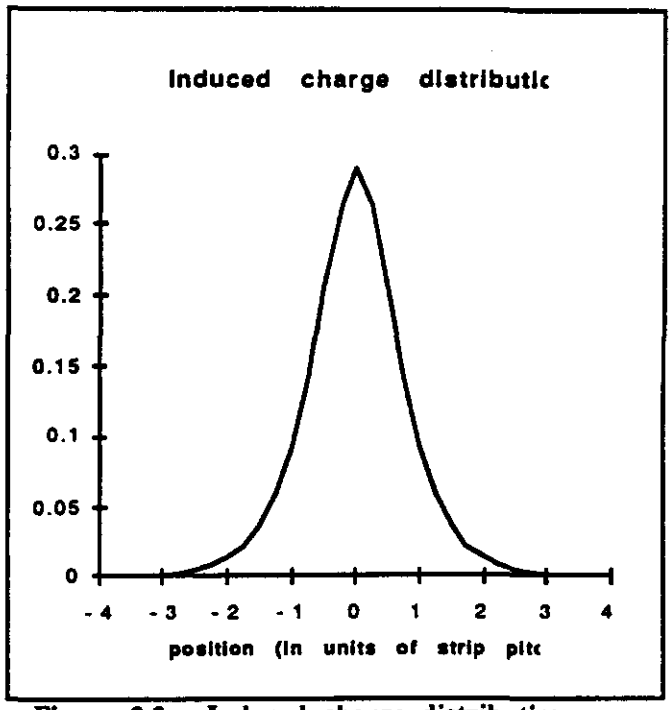

Figure 2.2: Induced charge distribution

2.1.5 Time development of the anode charge

The time development of the anode charge is given by:

$$Q_a(t) = Q_0 C \ln(1 + t/t_0)$$

where:

$$C = 1/\ln(r_c/r_a)^2$$

This formula is easily derived for the case of a cylindrical counter. It applies in our case too if the equivalent cathode radius defined above. $t_0 = ra/2\mu E_a$ is the chamber characteristic time, μ is the positive ion mobility and E_a is the surface field at anode wires.

2.1.6 Spatial Resolution of the Cathode Strip Chambers

The primary contribution to the resolution achievable by the CSCs is the electronic noise of the amplifiers. The precision of the center of gravity calculation depends linearly on the signal to noise ratio. This is shown in Figure 2.3 where the resolution as a function of the total anode charge is plotted for a prototype chamber for a system built for Experiment 814 at the BNL AGS. Notice that eventually other effects set a limit to the achievable resolution. One would like to be limited by noise and keep the gain of the chamber such that the total anode charge does not exceed 0.5--1.0 pC. Extensive studies of the limits of the achievable resolution have been reported by Smith, Fisher and Radeka (NIM, A252 (1986) 239-245).

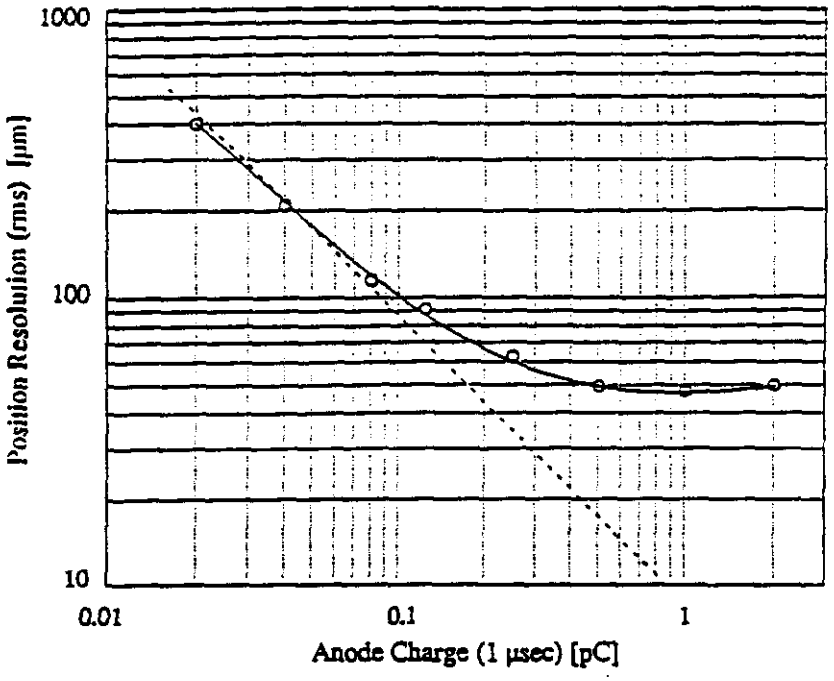

Fig. 2.3 Resolution vs total anode charge

Assume that the projection of the avalanche position on the cathode strip plane is at a point x=0. Then, in a standard manner, the position of the center of gravity is given by the ratio of the 1st and 0th moments of the charge distribution on the strip plane:

$$x_{CG} = \frac{\sum_{i=1}^{N} x_i q_i}{\sum_{i=1}^{N} q_i}$$

where $x_i = i l_a$ and l_a is the pitch of the cathode readout.

If the charges q_i are measured with an rms error of σ_{noise} then the uncertainty in x_{CG} is

$$\sigma_{CG} = \frac{\sigma}{Q}\sqrt{2\sum_i x_i^2}$$

or

$$\sigma_{CG} = \frac{\sigma}{Q}\sqrt{2l_a^2 + 2(4l_a^2) + 2(9l_a^2) + \ldots}$$

One can see that the resolution depends on the number of strips used. For example, for three strips it is

$$\sigma_{CG} = l_a \frac{\sigma}{Q}\sqrt{2}$$

and for five strips.

$$\sigma_{CG} = l_a \frac{\sigma}{Q}\sqrt{10}$$

Using the Monte Carlo simulation we find that the optimum is 3–5 strips. The resolution deteriorates rapidly for one or two (not enough information) and increases slowly when more than 5 strips are used because the electronic noise of more channels is added in quadrature. We can then calculate the required gas gain in order to maintain the contribution from the electronic noise below a certain level. Using three strips the total induced charge for a contribution to the resolution σ_x should be

$$Q > \frac{l_a \sigma_{noise}/\sqrt{2}}{\sigma_x}$$

For an estimated noise σ_{noise} =2000e at an integration time of 300 nsec, l_a =5mm, and for σ_x =50 μm, this yields Q>2.8 × 10^5e. Taking into consideration that only 40% of the charge is collected in 300 ns and that 0.5 of the induced charge goes to the uninstrumented cathode, the total charge seen by the cathode is 1.4 × 10^6e. For a 50% CO_2, 50% CF_4 mixture at atmospheric pressure there are ≈ 90 primary electrons. Therefore the true chamber gain should be M > 1.5 10^4.

2.1.7 The effect of the inclined tracks and the Lorentz angle

The next most significant contribution to the resolution of the CSCs is the effect of the inclined tracks and the Lorentz angle. These effects are extensively covered in a GEM note (V. A. Polychronakos and V. Tcherniatine, GEM TN-92-137, July 1992). Here we will summarize the main results.

The charge interpolation is optimum when the avalanche is formed on a single point along the wire. A finite spatial extend of the anode charge results in a resolution degradation. Such non-local charge deposition can be caused by a number of factors such as diffusion of the drifting electrons, absorption of δ-electrons, inclined tracks, and a Lorentz force along the anode wires in the presence of a magnetic field which is not collinear with the electric field of the chambers. The last two effects are, by far, the most important for both the Barrel and Endcap chambers. We used both simple geometrical arguments as well as results of the Monte Carlo to study in detail these effects.

It should be noted here that the Lorentz effect in the CSCs does not result in a systematic shift of the measured coordinate. It does not, therefore, require a correction. Simply, the resolution degrades because of the spread of the charge along an anode wire. The effect of the inclined tracks is minimized by adopting a 32-fold symmetry of the chamber structure limiting, thus, the maximum angle of incidence to ±5.6°. The Lorentz effect is compensated by tilting the chambers about the axial magnetic field by an amount equal to the Lorentz angle of the gas. Note that this tilt angle has to be consistent with the maximum tolerable angle of incidence. This results in choosing a gas with a Lorentz angle in the neighborhood of 6°. The 50% CO_2-50%CF_4 mixture

has a measured Lorentz angle of 8° at E=6 kV while exhibiting high enough drift velocity (60μm/nsec). In Figure 4 is shown (solid line) the resolution degradation as a function of angle of incidence within a barrel sector with the magnetic field on and the chambers tilted by 8°. It is assumed that the resolution smearing due to this effect is added in quadrature to an intrinsic resolution of 50 μm. The two dashed lines bracket the resolution curve when the field varies by (or is unknown to) ±20% from the nominal value of 0.8 T.

The basic cell in the Endcap orientation is shown in Figure 2.5a. The dominant contribution still comes from the axial component of the field especially for electrons drifting from the outer regions of the cell. In Figure 2.5b is shown an additional effect arising from the fact that the Endcap modules are trapezoidal and therefore the strips are not at right angles with the wires. This can cause a systematic shift which is proportional to the product of the tangent of the angle ϕ between the strips and the anode wires and the distance between the track and the nearest anode wire as shown in Figure 2.5b. Note that for tracks with a sufficiently large polar angle θ, the primary ionization electrons could be collected by two adjacent anodes. Such a track is shown in Figure 2.5a.

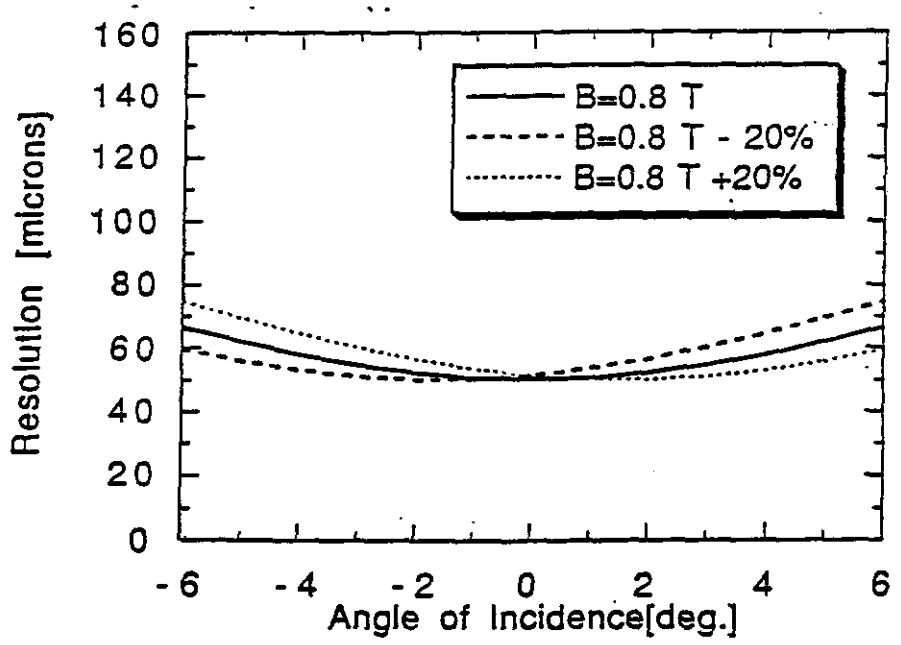

Fig 2.4 Resolution degradation vs angle of incidence

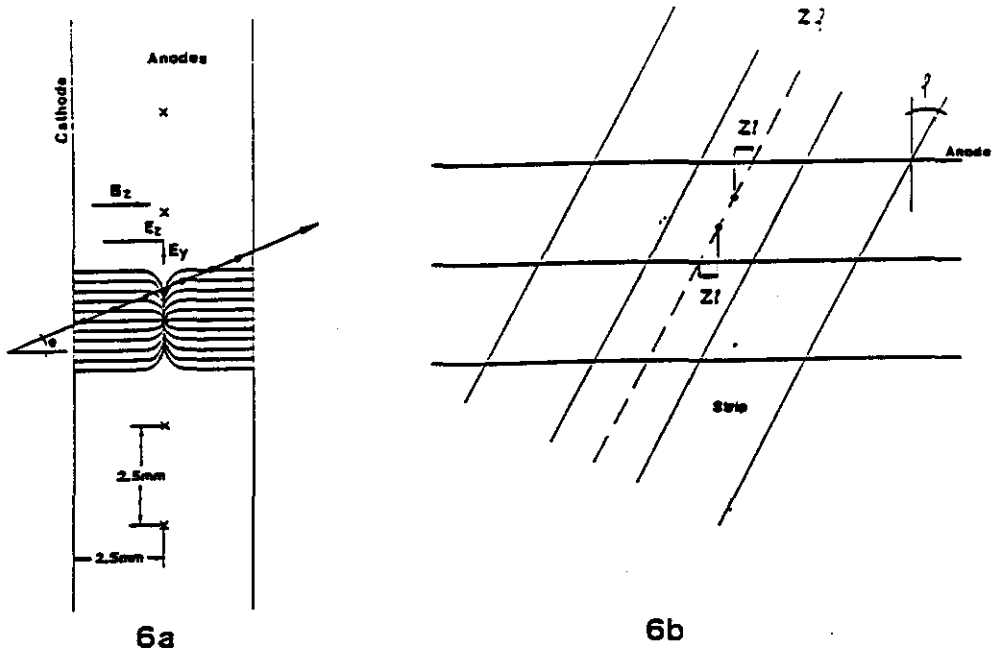

Fig. 2.5 a) The basic PWC cell in the Endcap b) The effect of the angle ϕ between the anodes and strips

The design of the endcap modules has a 16-fold symmetry imposed by the overall muon system. However internally the symmetry is 32-fold reducing the effect of this angle. This is accomplished by supporting the wires at the symmetry axis of the trapezoidal sectors as shown in Figure 2.6. In any case this support is necessary for electrostatic stability as the anode wire especially in the outer two superlayers, can be much longer than the approximately 1m maximum length for stable operation. Recall that to compensate for the Lorentz effect in the Barrel one has to rotate the wires about an axis along the magnetic field by an amount equal to the Lorentz angle. For the Barrel this resulted in "tilting" the modules. The same principle applied to the Endcap module results in rotating the anode wires about the axial component of the magnetic field in the plane of the anodes. The wire placement to take into account both of the effects discussed above is shown in Figure 2.7. The resulting improvement of resolution is shown in Figure 2.7 where the resolution is shown with (lower curve) and without compensation for the Lorentz effect. These represent an average over all the modules of the Endcaps. The module-to-module difference is less than approximately 10%.

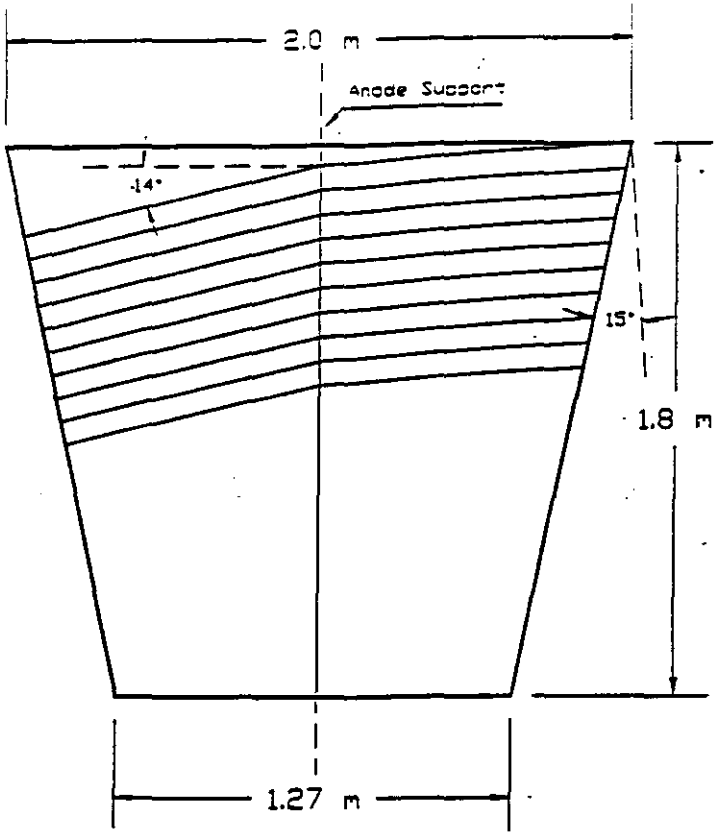

Fig 2.6 Wire placement for optimal resolution

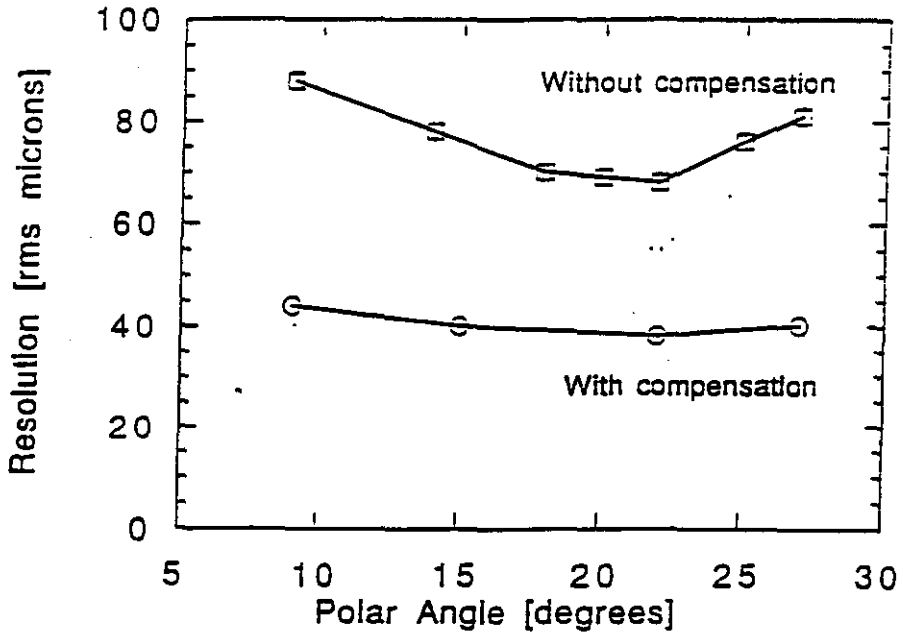

Fig 2.7 Resolution vs azimuthal angle in the endcap, with and without compensation of Lorentz and angle effects

2.2 Overview of CSC Module Construction

The position and timing resolution requirements are met by constructing modules with multiple chambers in a common package. Internal, relative alignment of the individual chambers is mechanically stable and precision of each chamber is controlled and monitored so that the position resolution of N chambers is $1/\sqrt{N}$ times the single chambers resolution. Timing resolution is approximately 1/N times that of a single chamber. Modules will combine four chambers. Each module has common utilities, control, and DAQ connections. The module is the fundamental unit for further alignment, relative to other modules in the muon system and relative to the detector coordinate system.

Modules in the barrel are rectangular. In the endcaps, the modules are trapezoidal, reflecting the requirement for the momentum trigger that the cathode strips be radial. The width (anode direction) of the module is limited by several factors. Lorentz effects and angle-dependent resolution, were described earlier in this section. Electrostatic instability of the 30μm diameter tungsten wires limits the unsupported anode wire length to roughly 1.2 to 1.5 meters, depending on operating voltage and gas gap. The availability of cathode materials and the limitations of technologies for applying the strip pattern provide a practical limit on the width also in the range of 1.2 to 1.5 meters. The length (strip direction) of the CSC's in the barrel is 3 to 4 meters, set by noise due to strip capacitance and by material and process limitations. In the endcaps, the charged particle flux below $\theta \sim 17°$ further limits the strip length. A detailed spreadsheet showing module sizes, weights, channel counts, and occupancy due to charged particles was given in Table 1.2.

A plausible module design is shown in various sections in Figures 2.8 to 2.10; another design showing some different features is shown in figure 2.11 These designs have been developed from several generations of prototype chambers that have been constructed and are now under test. Protptypes will be discussed in more detail later in this section. The central idea in the design is to meet requirements of flatness and rigidity of the chambers by using panels made by laminating the cathodes onto a lightweight cellular core (e.g. Nomex at 1.8 lb/ft^3). With a core thickness of order 1" the laminated panels will have acceptable sag in any orientation. In the endcaps, gravity-induced sag is not an issue and core thickness could be reduced.

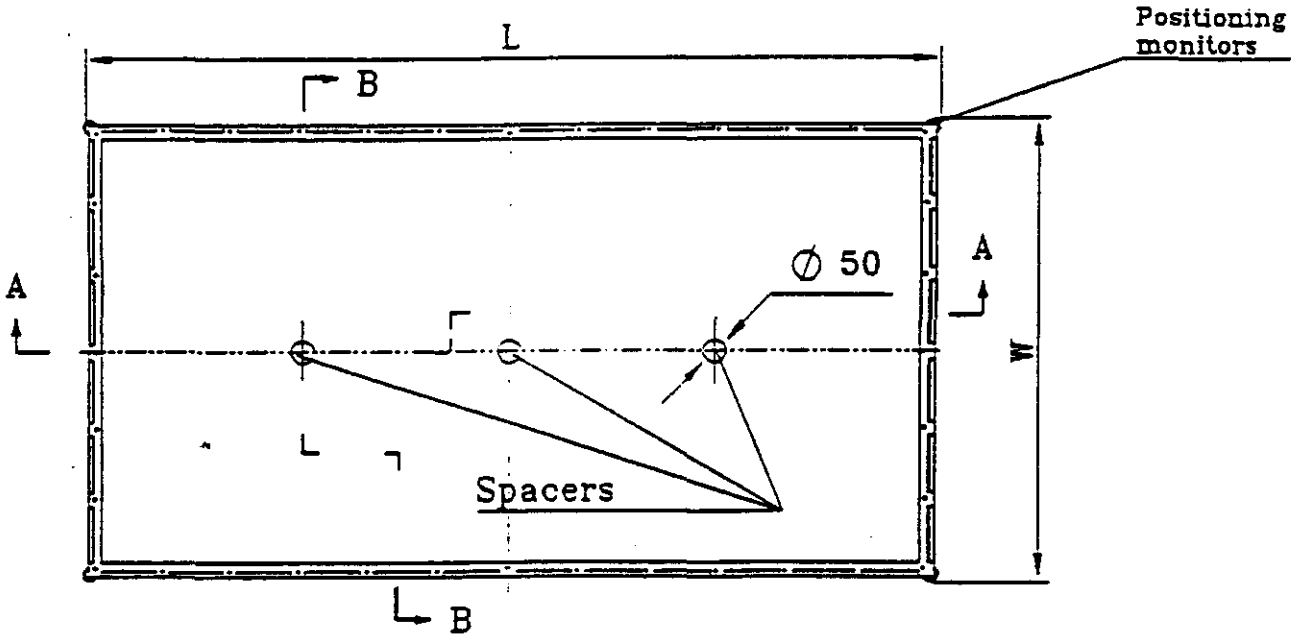

A-A (B-B)

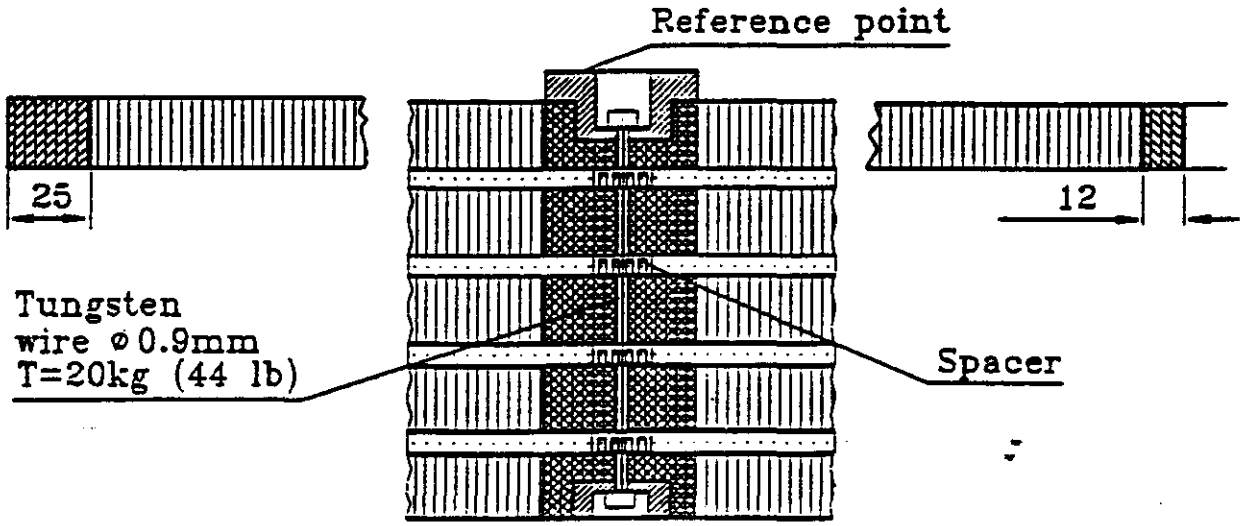

	Outer Layer	Middle Layer	Inner Layer
L	3.506m	2.515m	3.152/3.028m
W	0.960m	1.320m	0.740m

Fig. 2.8

Y.Ershov
I.Golutvin
V.Lysiacov
S.Movchan

BARREL CSC

CROSS SECTION ALONG THE STRIPS (A–A)

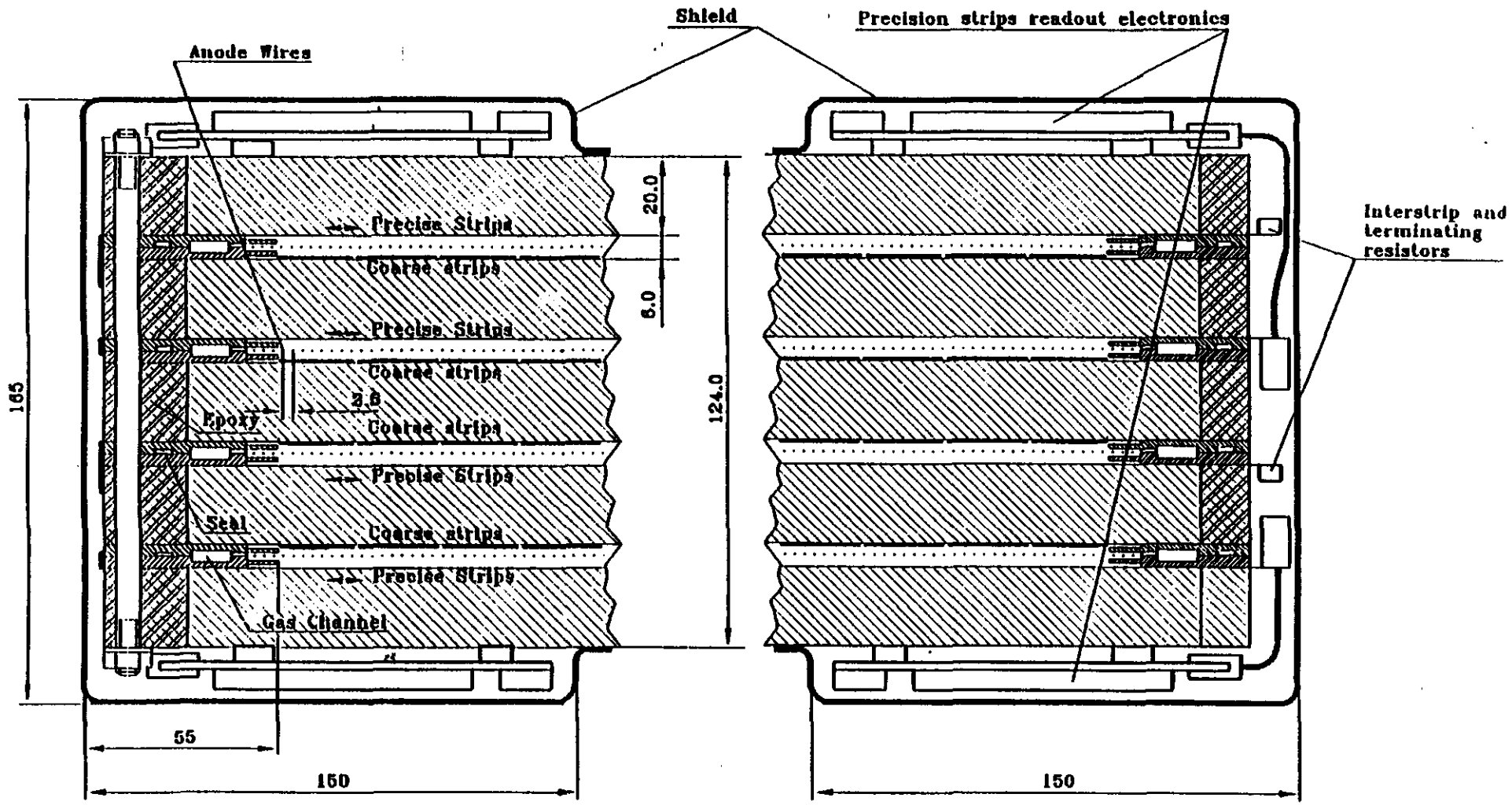

Y.Ershov
I.Golutvin
V.Lysiakov
S.Movchan

Fig.2.9

BARREL CSC

CROSS SECTION ALONG THE WIRES (B–B)

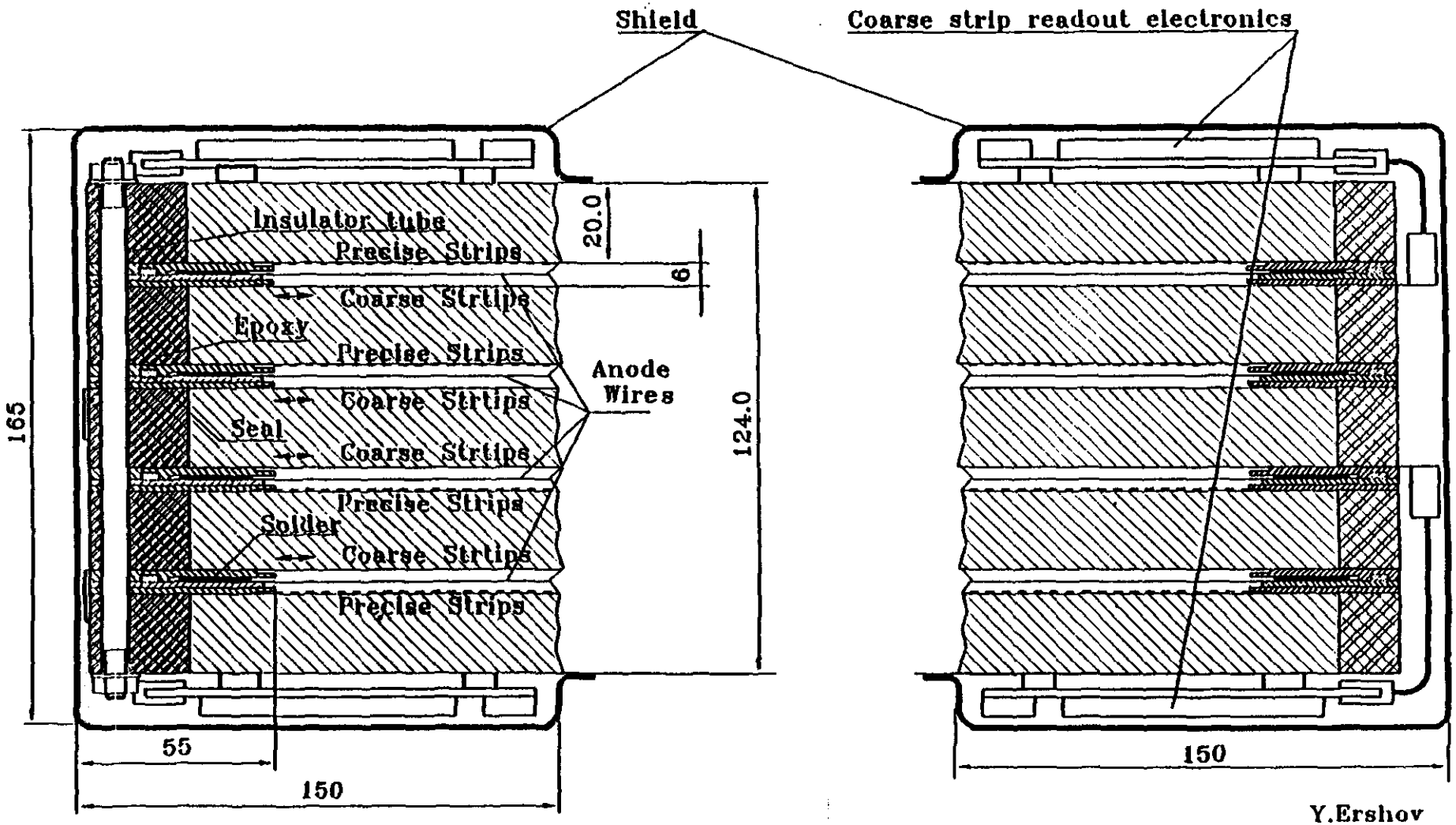

Fig.2.10

Y.Ershov
I.Golutvin
V.Lysiakov
S.Movchan

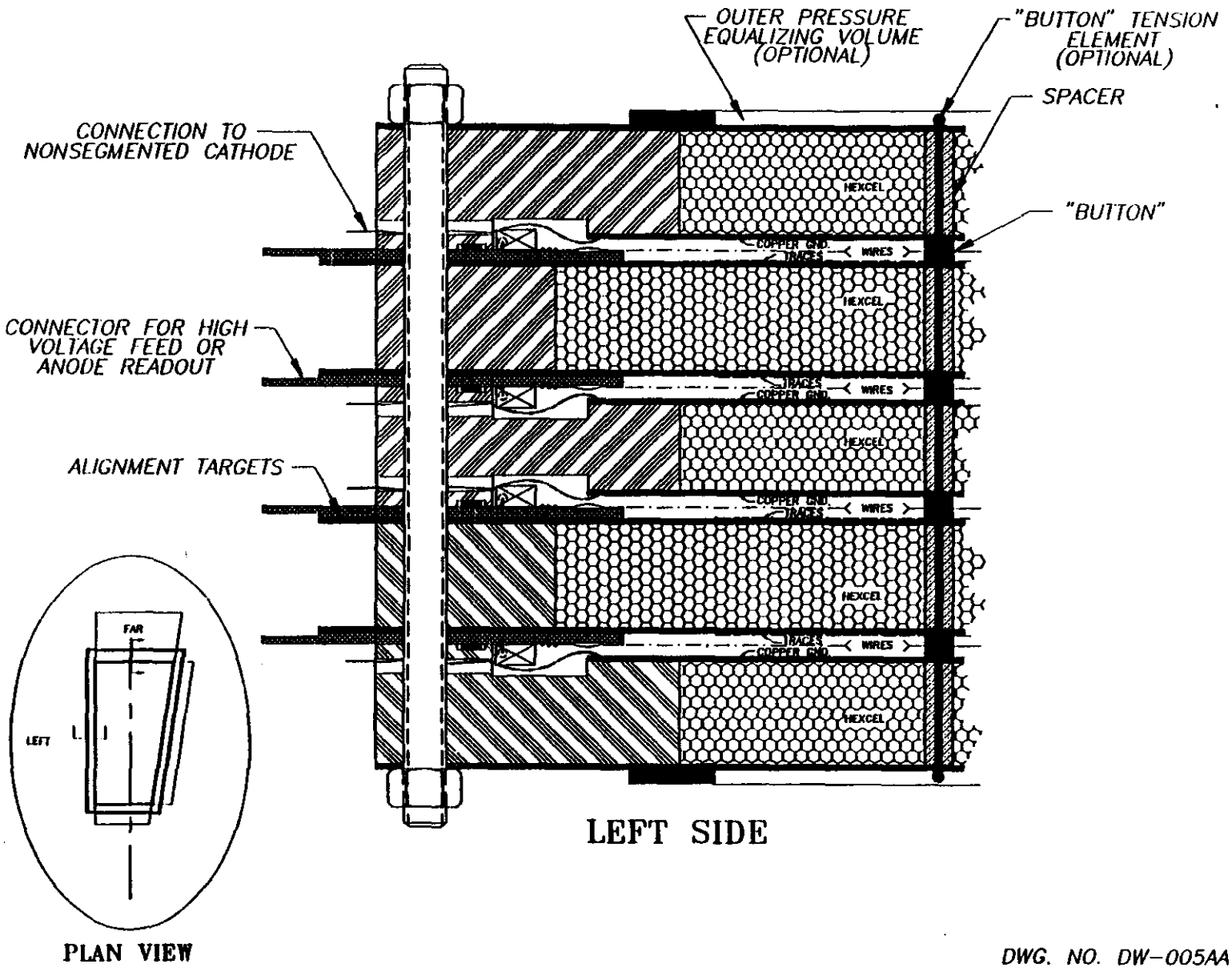

Fig. 2.11 An alternative CSC design concept

An accounting of the mass and radiation lengths in the principal components is given in Table 2.1 for a typical CSC module. Each chamber in the module has an active area surrounded by frames that are taken to be inactive for detecting muons. When the modules are overlapped to avoid acceptance losses, muons will sometimes traverse the frames of one chamber as well as the active area of another. For this (rough) design, muons traversing the active area only will pass through 8% of a radiation length. Approximately 10% of the time a muon would also pass through the frame of an overlapping module, for a total of 51% of a radiation length. The average thickness in radiation lengths, including the overlap, is about 12%.

Table 2.1 Material in a typical CSC

Material Audit for Cathode Strip Chamber Module

Calculation of mass and radiation lengths for a four chamber module

Active area of chamber:
length (m) = 3.0
width (m) = 1.5
total area (m^2) = 5.0

frame material (and dead area):
width (m) = 0.050

(including inactive frames)
fraction of active area overlapped by frames = 0.098

component	material	density	cm/X0	thcknss (cm)	mass (Kg)	normal X0
Hexcel core	Nomex	0.14	485.7	2.5	86.80	0.0257
circuit boards	.031" G10	1.7	19.4	0.079	66.39	0.0406
copper	1/2 oz.ft^2	8.96	1.43	0.0017	7.56	0.0119
frames	~ lucite	1.2	34.4	3.0	82.80	0.4360

total mass (Kg) =	243.5
mass/area (Kg/m^2) =	49.1
average X0's =	0.119
X0's through center =	0.078
X0's, center + frames =	0.514
area-weighted ave X0's =	0.121

<- includes material of overlapping chamber

Wires are strung on printed circuit frames of precision thickness that are glued to the precision cathode. Wires are tensioned to ~170 grams, ~ 2/3 of the elastic limit; they are held by glue and solder and the wire pitch is set by the fixturing during construction. The panel takes the load of the anode wires; the symmetric loading offsets any tendency to distort the panel. The frames are circuit board material of precision thickness. They bus HV and route anode signals to an edge connector. On the non-precision cathode lamination is a frame fabricated with precise moldings produced with pultrusion technology; this frame controls the gas gap and provides access for electrical contact to the non-precision cathode. Gas distribution is achieved through a manifold built into this frame. This approach provides a precise, low-weight, low-cost structure that avoids extensive machining. It allows accurate control of the important parameters and provides access to the precision cathode all around the perimeter for alignment.

One alternative under study is to use Iarocci-type "profile" chambers where the wires are strung in individual channels in a conductive plastic extrusion. This approach has potential advantages in robustness of the chamber and disadvantages in efficiency and attainable wire pitch.

Many of the mechanical issues of chamber design are independent of which approach is used for the wires.

Chambers are assembled to form a module either by gluing the structure together or by bolting the components together with gaskets making the gas seals (strips on the cathodes can be routed around the bolt holes). The disadvantages of a non-openable structure compared to the disadvantages of an openable but potentially leaky structure are under study. It may be necessary to provide a gas volume on the outside of the module to equalize the pressures on both sides of the outermost lamination and avoid deflections. An attractive alternative would be to use spacers in the gas gaps, aligned with spacers imbedded in the laminations; the stack of spacers through the module would be penetrated by a tension element that would constrain the module components in the coordinate normal to the cathode planes. This would regulate the gas gap and prevent bowing under modest pressure imbalances. It would likely also loosen the flatness requirements on the laminations and by tying together the various planes would lead to a much stronger mechanical assembly.

The module is a self-supporting, rigid package. It is mounted kinematically at three points to the support frame. Actuators may be required to allow movement of the modules to maintain their position within the dynamic range of alignment instrumentation.

The intent is that each module be as autonomous as possible, to minimize possible electrical noise problems and to minimize external connections with their cost and complexity. Low and high voltages would be generated on-board from power feeds. Local computers would handle DAQ and monitoring and control functions. Trigger primitives could be calculated and transmitted on a serial optical link. A total of order a dozen optical fibers, along with the power input, would be the cable plant. The only other external connection would be for cooling water; a four-chamber module of typical dimensions will dissipate approximately 100 watts.

2.2.1 Cathodes

The strip cathodes must meet stringent requirements on their accuracy in order for the high precision possible by charge interpolation not to be limited by knowledge and uniformity of strip placement. The gap between strips must be controlled at the 50 μm level, as discussed earlier. In the barrel CSC's, the strips are parallel; in the endcap CSC's, the strips run radially, increasing in width as the radius increases while keeping the gap between strips fixed. This requirement limits the possible technologies for fabricating the endcap CSC cathodes. Possible technologies for cathode fabrication include stan dard printed circuit board photolithography, copper deposition techniques, and mechanical milling of copper-laminated substrate — the last is only appropriate for the parallel strips of the barrel CSC cathodes. Prototypes so far have used photolithography, with very satisfactory results as described below. This approach facilitates customizing the cathode design with floating strips, varying strip widths, including alignment features, and routing signal traces around bolt holes. Disadvantages include difficulties with photoplotting large areas, possible instability of films due to temperature and humidity variations, and sensitivity to details of the etching process such as etchant concentration and duration of exposure. We are actively exploring alternative technologies and are discussing with vendors what are the practical limitations in various approaches.

The non-precision cathode is required to form the electrostatic structure and the mechanical structure, but it plays no role in data acquisition. The only electrical requirement is for frequent

connections to the grounds of both the anode and the cathode readouts to allow low inductance signal return. The non-precision cathode is presently envisioned to be a thin G-10 lamination of the same material as the precision cathode but without the costly photolithographic processing. This is the technique used in prototypes so far. It might also be possible to fabricate the non-precision cathode as a very thin glass cloth lamination on the core, with a coating of silver paint providing the necessary electrical conductivity.

As discussed above, measurement of the second coordinate, determining the polar angle, has been envisioned to be accomplished by readout of the anode wires. The anode wires are connected in groups of 20 wires in the endcap CSCs, and in groups of 40 wires in the barrel CSCs; this limits the number of anode readout channels to an acceptable level while providing sufficient precision in polar coordinate and minimum time jitter. The alignment of the wire groups in the four wire planes of a module is staggered to provide finer position resolution.

2.2.2 Alternative Design Concepts

Several alternative design approaches are possible. The profile chamber design has been discussed above. The determination of the polar coordinate could be achieved by charge measurement on coarse strips running the azimuthal direction on the "non-precision" cathode. This would have the advantage of avoiding readout connection to the anode wires and avoiding the attendant blocking capacitors. A disadvantage is that this approach would require more extensive processing of the non-precision cathode and more extensive electrical connections to it. Another variation would be to pattern both cathodes with strips perpendicular to the anodes, and to join the corresponding strips on the two cathodes together electrically in the readout. This offers better performance in S/N and could allow wider strips and fewer readout channels for the same position resolution. Negative aspects of this approach include increase costs associated with the second precision cathode, mechanical complications due to the necessary precision alignment of the two cathodes of a single gas gap, and poorer two-track resolution for the wider strip width.

2.2.3 Alignment

Alignability is one of the major advantages of the CSC approach. Alignment requirements and design of a system that will meet those requirements are discussed in section 4. The point to be made here is that alignment within a single chamber is accomplished by the precision of the cathode strip technology. Alignment markers are laid down on the precision cathode by the same process by which the strips are created. These markers are available for complete characterization of the cathode before assembly of the chamber, and they are visible and externally accessible after the module has been assembled. There is a single alignment transfer required to establish th eorientation of the cathodes in a module relative to module alignment markers (which may be, e.g. the markers on one of the cathodes). In prototypes, this alignment transfer has been accomplished both by dowel pins inserted in holes drilled in the cathodes and by precision washers that were glued to the cathode and which overlapped the edge so as to be touchable for mechanical alignment.

2.3 Gas Studies: Measurements of Drift Velocities and Lorentz Angles

In order to achieve the required high precision in timing and position measurements and to be acceptable in the GEM muon system environment, the following basic properties for the gas mixture are required:

- high electron drift velocity
- small Lorentz angle
- low ageing and sparkproofness
- small electron diffusion coefficient
- nonflammable, nontoxic, nonexplosive

Gas mixtures based on CF_4 with high drift velocity have been proposed for high rate environments. The mixture of "cool" CO_2 with low diffusion and "fast" CF_4 can be an especially appropriate for use in the CSC chambers. An experimental set-up to measure the electron drift velocity and Lorentz angle for various gas mixtures has been designed and constructed in PNPI. A new method for measurement of the electron drift time by detecting α-decay recoil in coicidence with α-particles was used. The accuracy of the drift velocity measurements was about 1%, and the uncertainty in Lorentz angle was about 0.5 degree. The calibration for 90%Ar+10%CH_4, 50%Ar+50%C_2H_6 and 100%CH_4 were in good agreement with other experimental data.

We have measured drift velocity and Lorentz angle for CO_2/CF_4 mixtures with 0, 30, 50, 70 and 100% CF_4 concentration at B=0.8T (fig.2.12). For 50%CO_2+50%CF_4 results agree with measurements obtained earlier by the BU group . Pure CF_4 has a very high drift velocity and a large Lorentz angle. The addition of a cool CO_2 significantly reduces the Lorentz angle to 6-8 degrees while preserving a high drift velocity. The dependence of Lorentz angle on magnetic field for pure CO_2 and 50%CO_2+50%CF_4 is shown in fig.2.13.

The addition of a noble gas in a CO_2/CF_4 mixture allows us to decrease th operating high voltage, important for electrostatic stability and maximal tension of the signal wires. As shown in fig.2.14, the Lorentz angle for ternary Ar/CO_2/CF_4 and Xe/CO_2/CF_4 gas mixtures is about 8 degrees and practically insensitive to the drift field. The drift velocity at 4-6 kV/cm is 60-80 mm/μsec. Further studies of these promising gas mixtures are necessary.

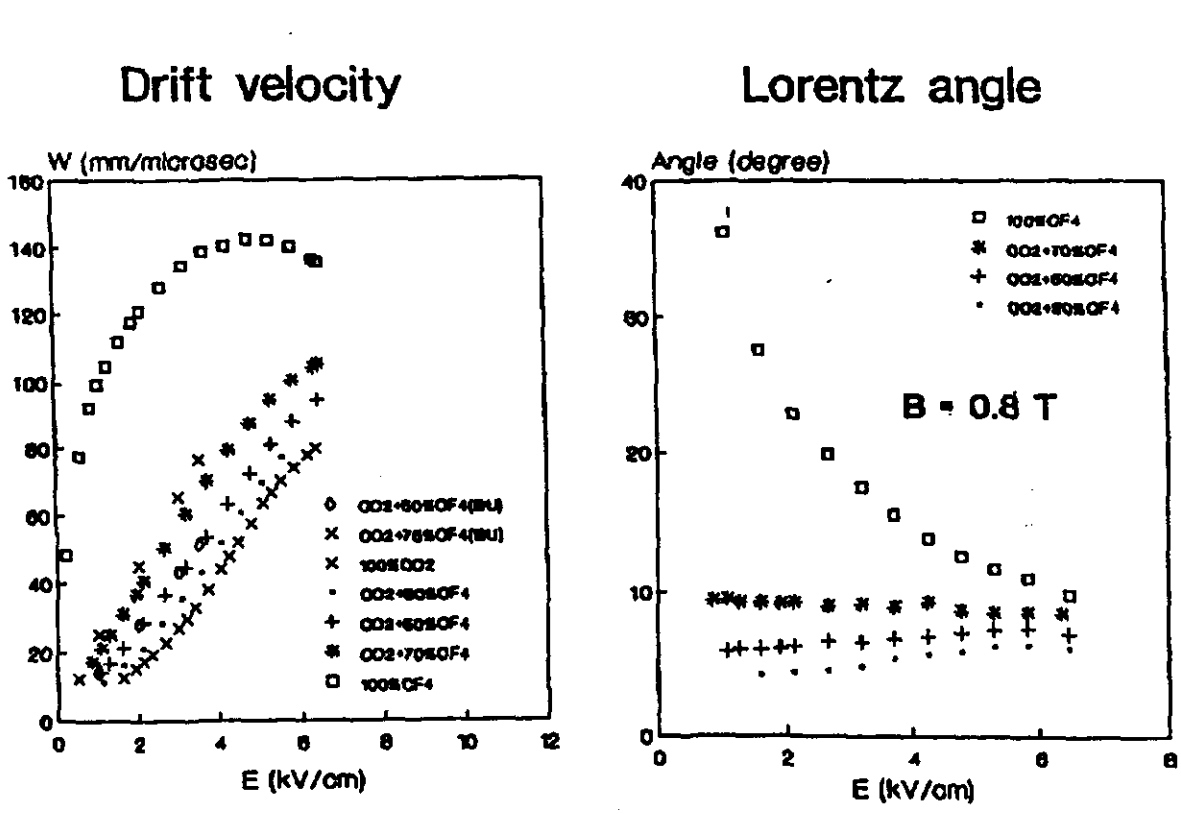

Fig. 2.12 Drift velocity and Lorentz angle of CO2/CF4 gas mixtures.

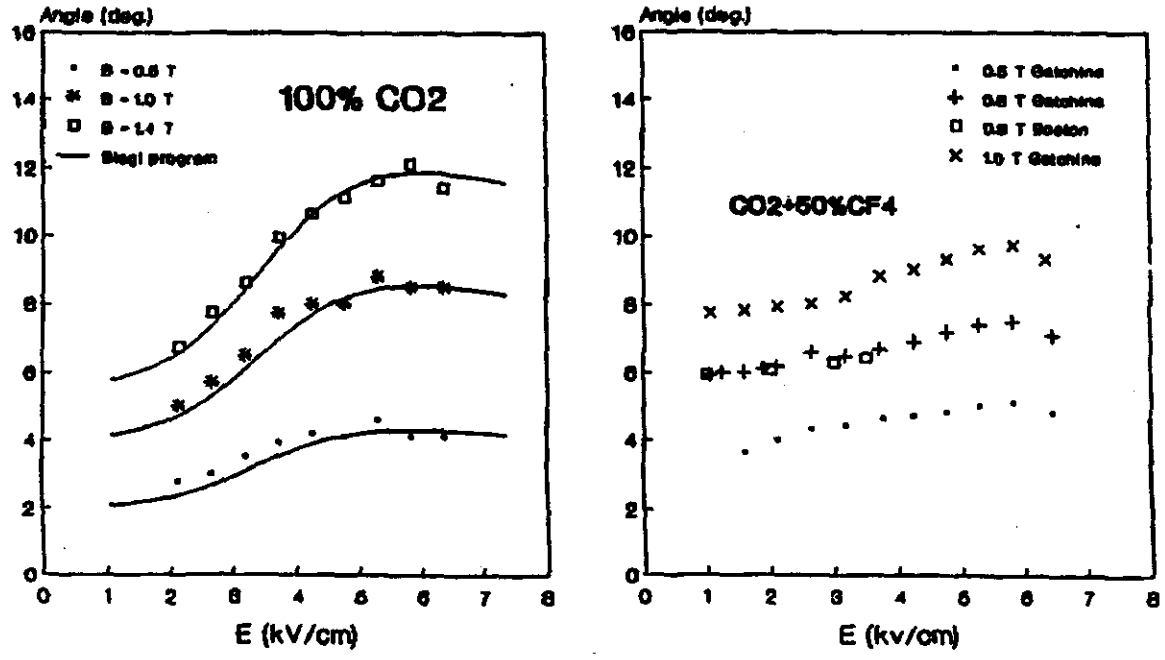

Fig 2.13 Dependence Lorentz angle verses magnetic field for 100%CO_2 and 50%CO_2 + 50%CF_4.

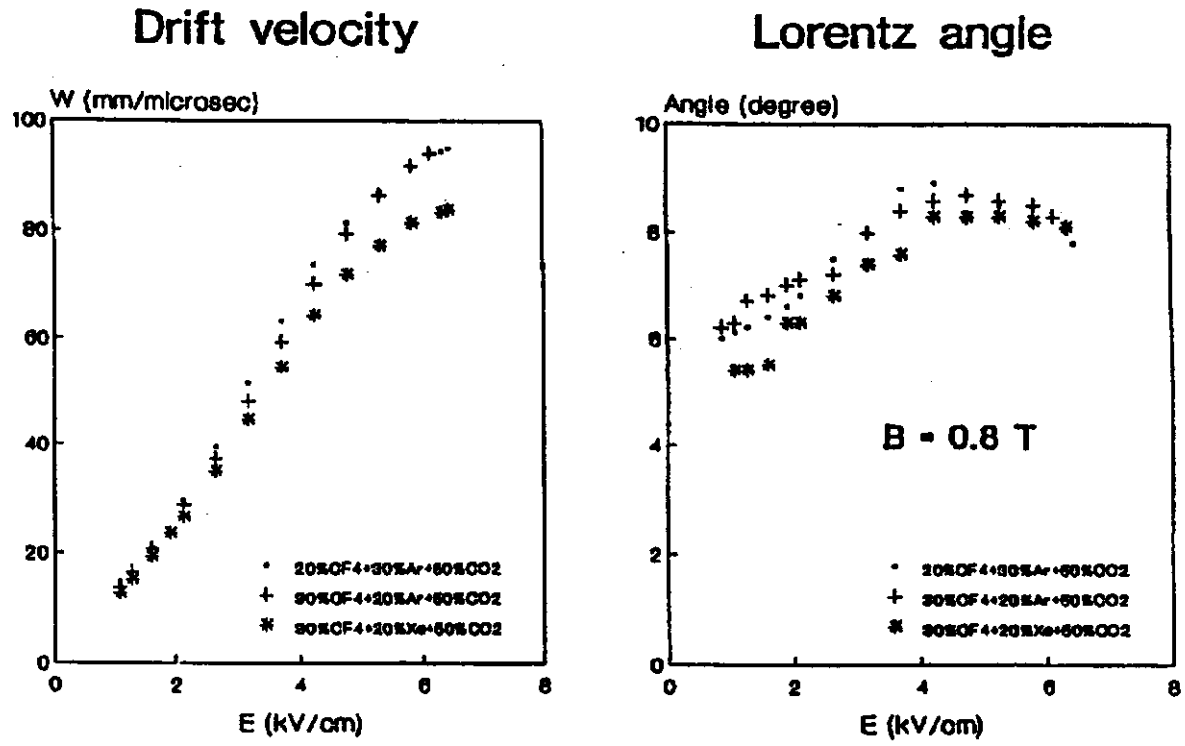

Fig. 2.14 Drift velocity and Lorentz angle for Ar/CO2/CF_4 and Xe/CO_2/CF_4 gas mixtures.

2.4 Results from Prototype CSC Construction

2.4.1 Drawings of prototype chambers

We present here some results from the CSC prototype development effort. Prototypes are being constructed at Brookhaven National Laboratory, at Boston University, at the University of Houston, and at JINR Dubna. Figures 2.15 and 2.16 show some views of the large prototype under construction at BNL and BU; it has an active area of roughly 1m by 2 m and will be tested at the TTR this Fall. Figure 2.17 shows the design details and 2.18 shows the cathode layout for the small prototype constructed at BU; it has an active area of roughly 30cm by 40 cm. Two two-gap modules of this design are now under test in the RD5 beam at CERN. Figure 2.19 shows the design of a CSC prototype constructed at UH with open profile chambers and already delivered for test at the TTR. Figures 2.20 and 2.21 present the Dubna CSC prototype, soon to be delivered to the TTR. This very active prototyping program has explored a variety of approaches to cathode layout, closeouts, gas routing, and other practical aspects of chamber construction. We are now working to combine the best features in a single, manufacturable design.

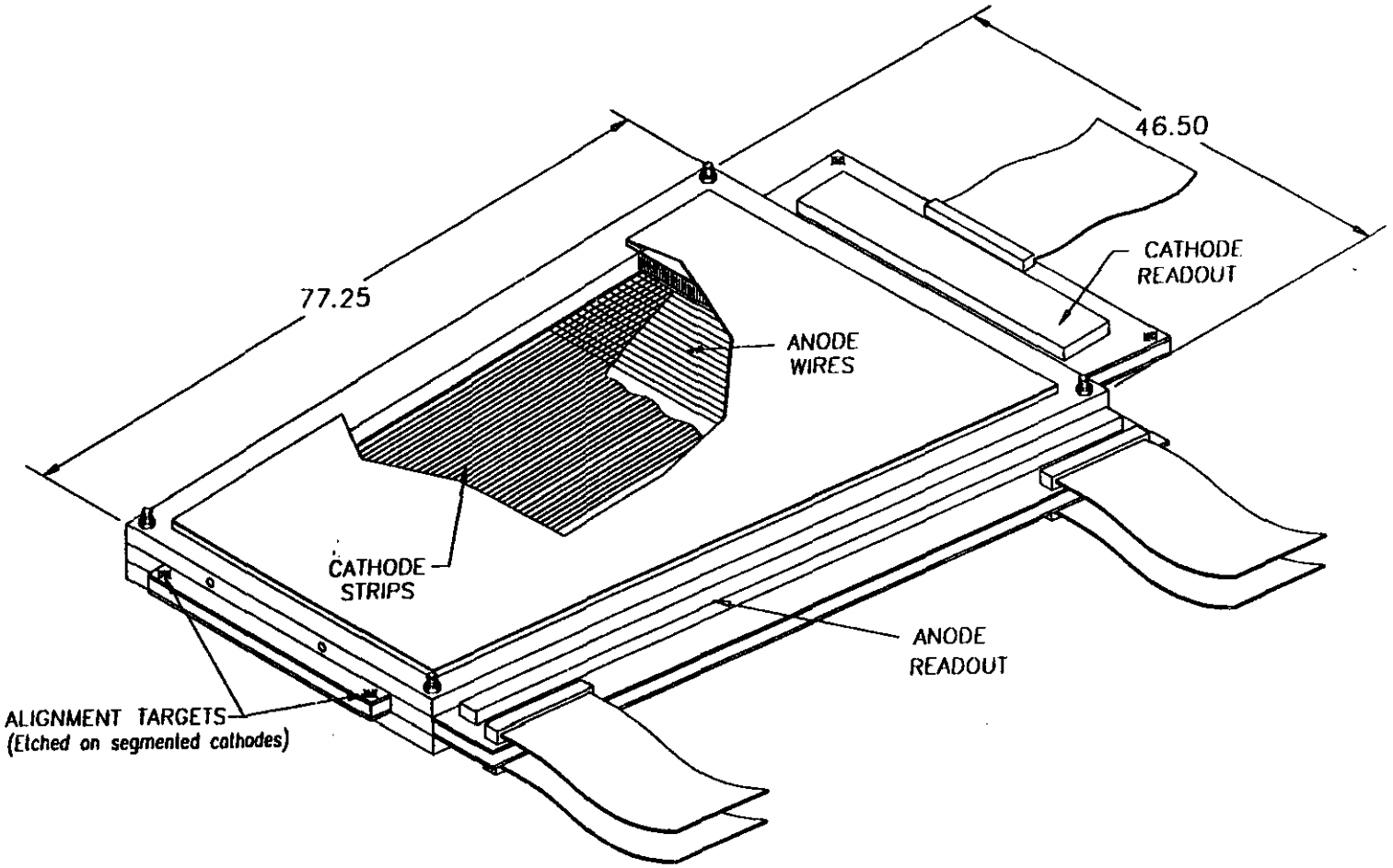
46.50
77.25
CATHODE
READOUT
ANODE
WIRES
CATHODE
STRIPS
ANODE
READOUT
ALIGNMENT TARGETS
(Etched on segmented cathodes)

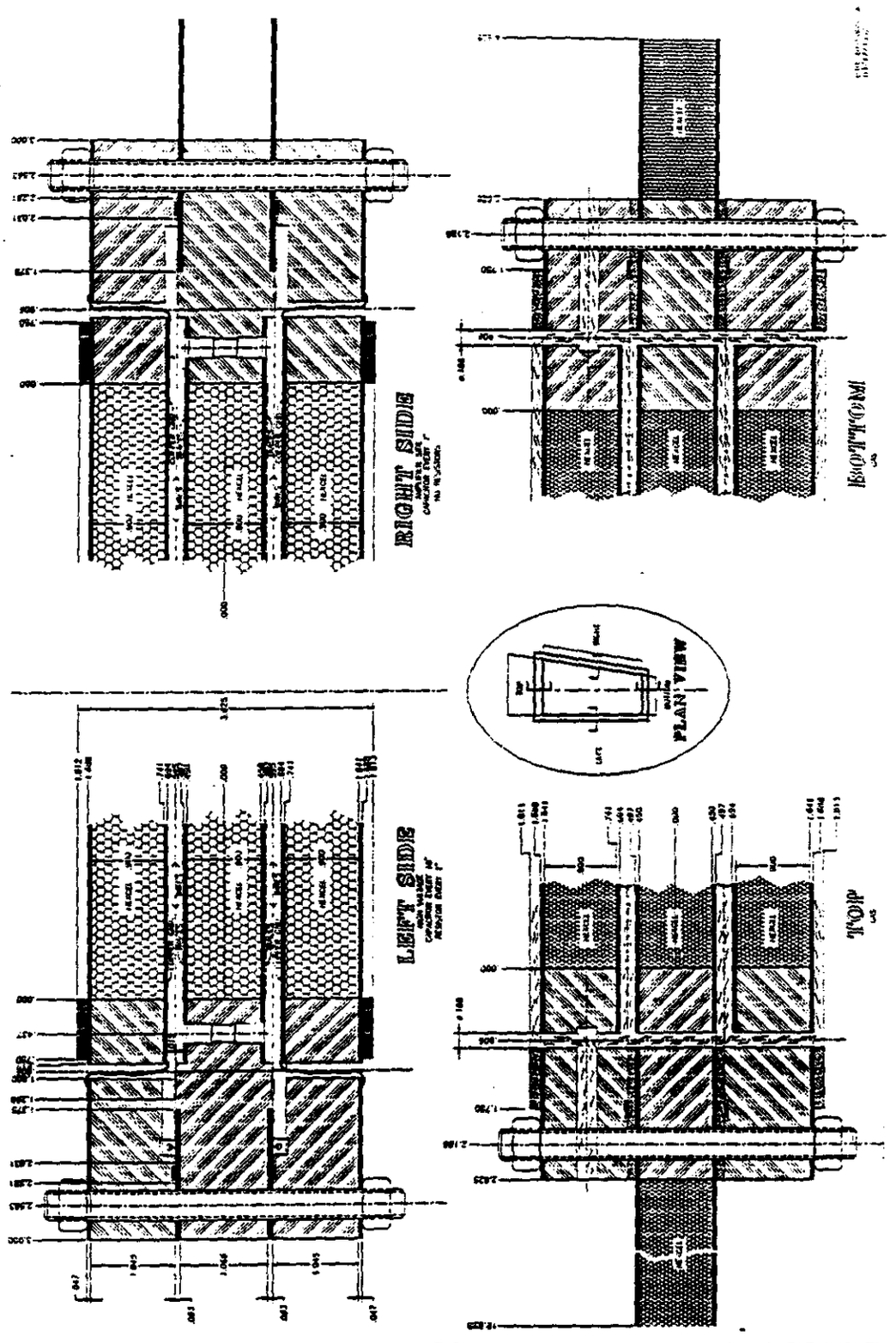
RIGHT SIDE
REAR
PLAN VIEW
LEFT SIDE
FRONT

CSC DOUBLET -- CONCEPTUAL DESIGN

"NEAR" SIDE CUT-AWAY SCALE: 1:3 "FAR" SIDE CUT-AWAY

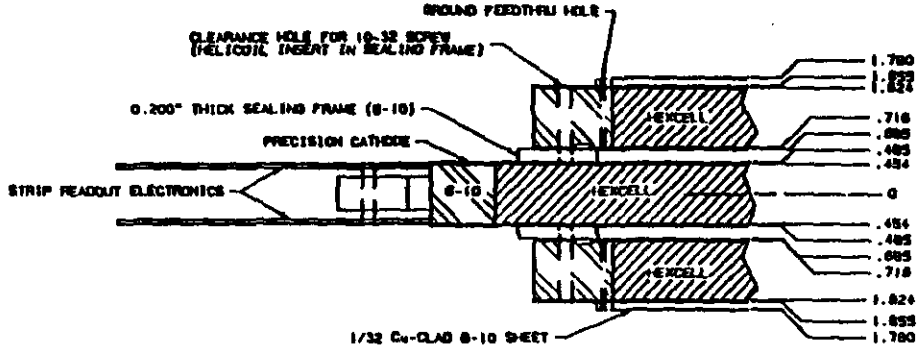

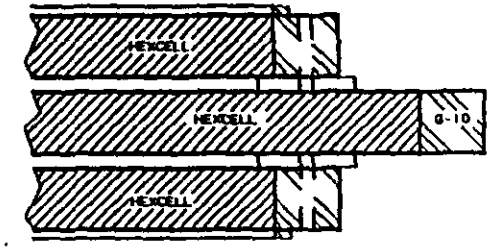

FAR

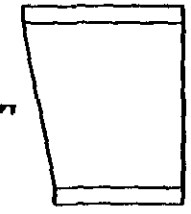

"LEFT" SIDE CUT-AWAY "RIGHT" SIDE CUT-AWAY

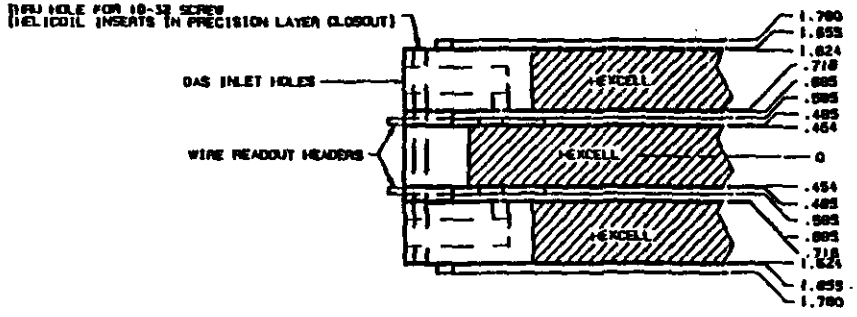

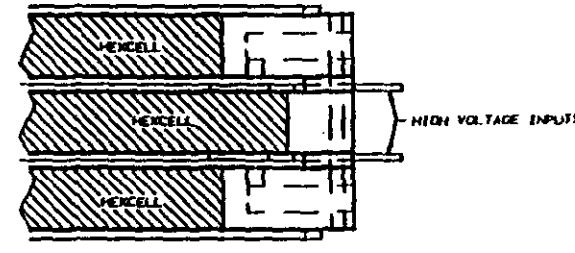

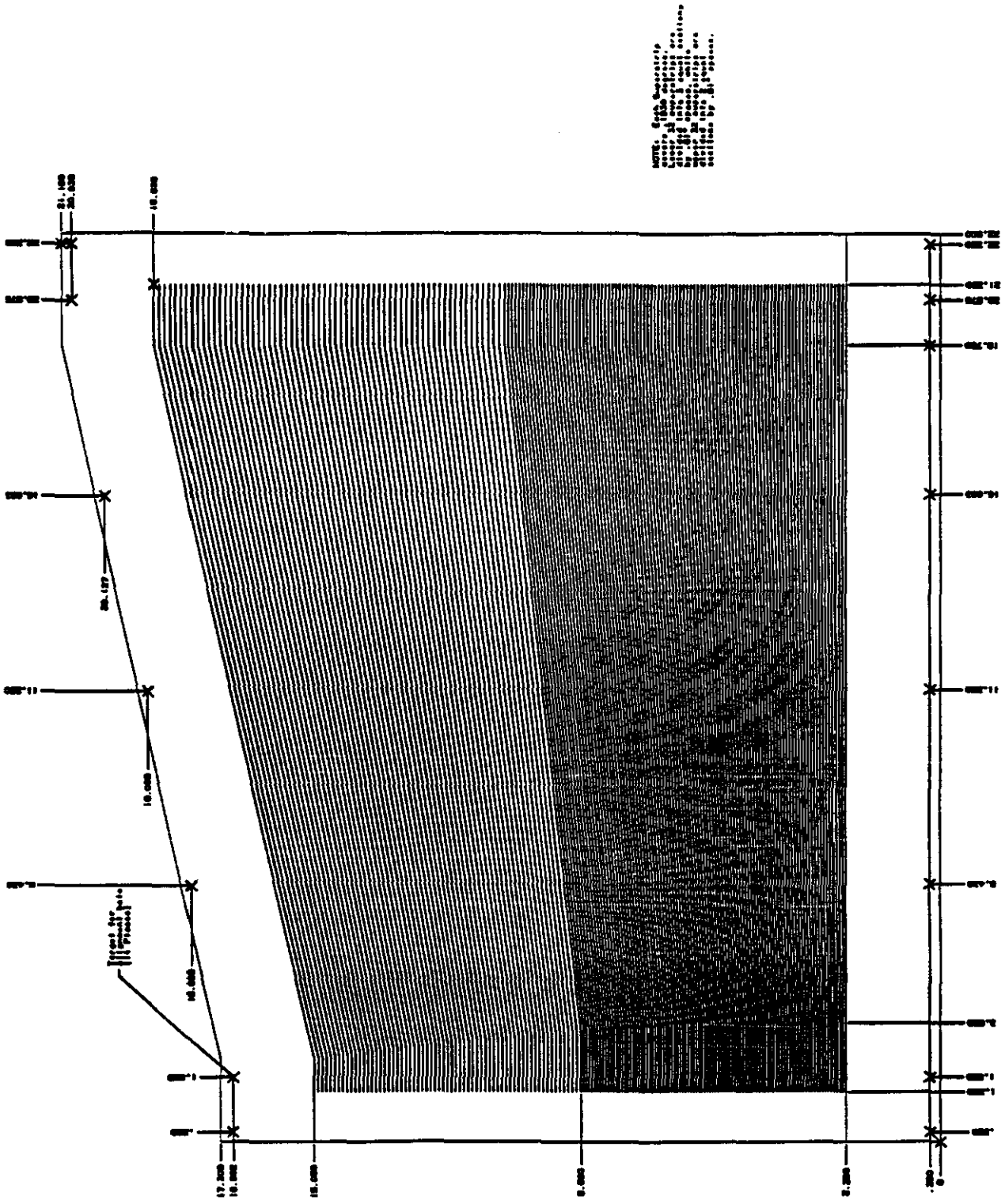

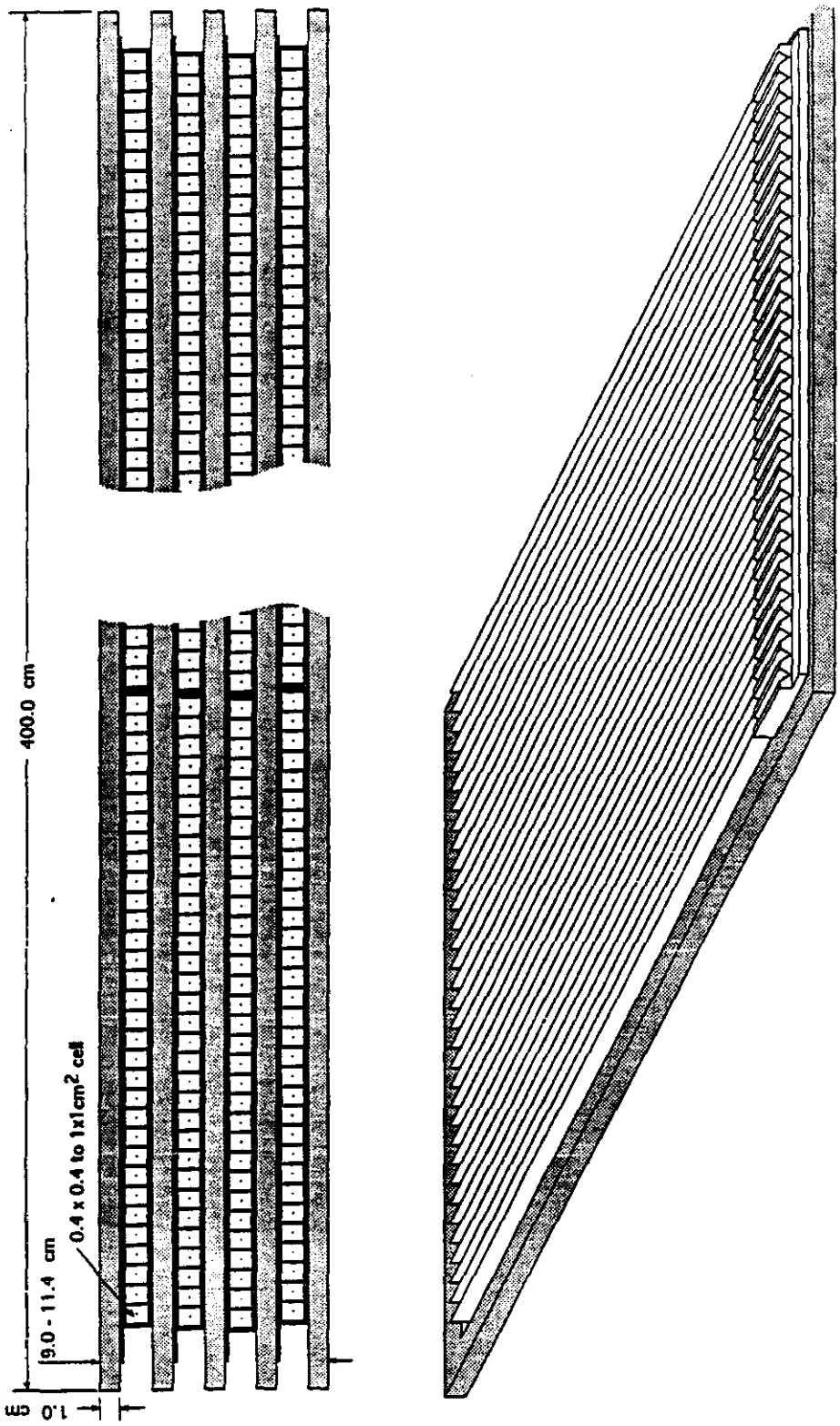
400.0 cm
9.0 - 11.4 cm
0.4 x 0.4 to 1x1cm² cell
1.0 cm

DUBNA CSC PROTOTYPE

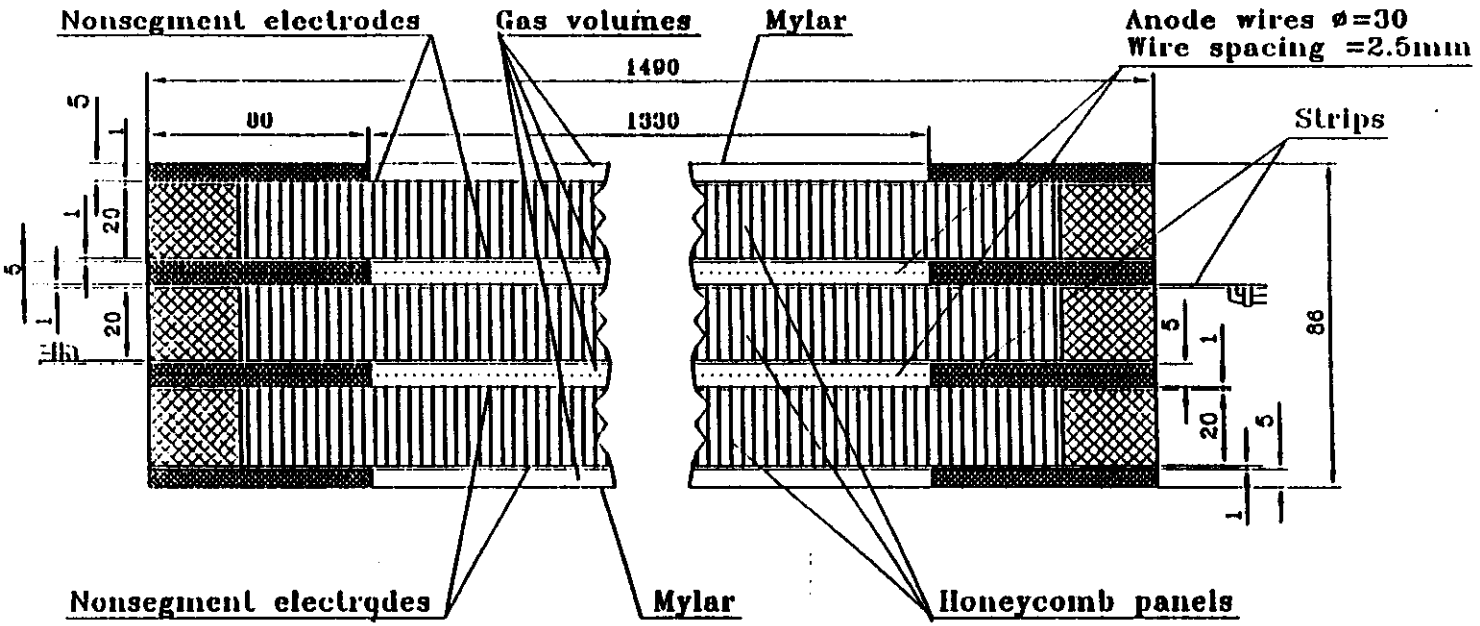

Cross-section of MWPC perpendicular to the wires
(All dimensions in mm)

Fig. 2.20

DUBNA CSC PROTOTYPE

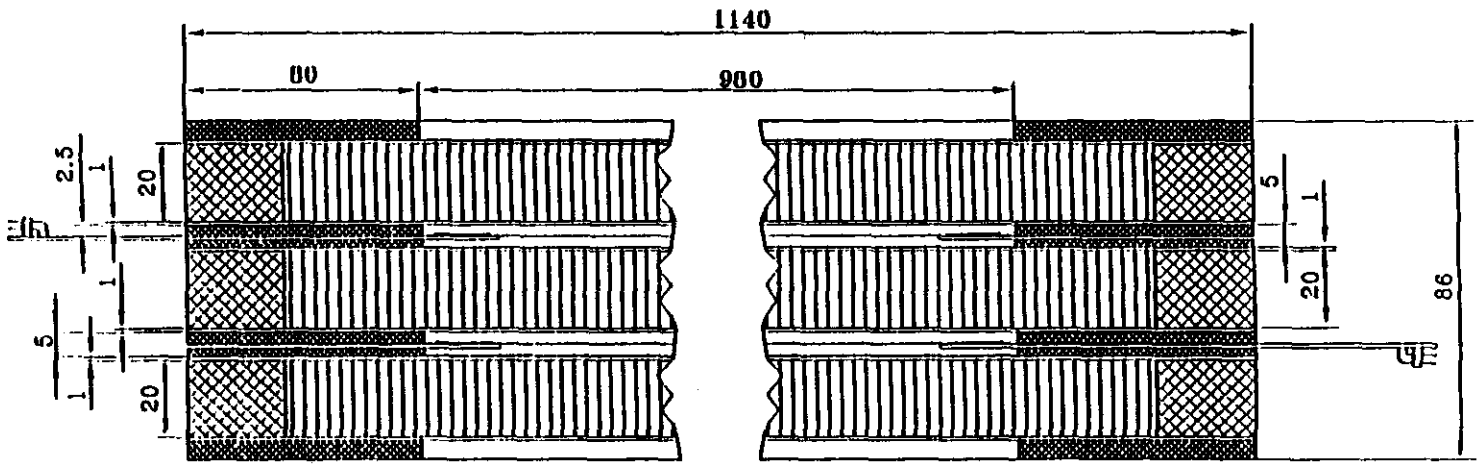

Cross-section of MWPC perpendicular to the strips

(All dimension in mm)

Fig. 2.21

2.4.2 Measurements of Prototype Cathodes

We studied the quality of several cathodes that were fabricated in our prototype program. At both BU and UH, cathodes manufactured by standard etched printed circuit board technology were surveyed with coordinate measuring machines and were found to conform to design dimensions to better than 25 microns. Strip-to-strip capacitances for the one-intermediate-strip and two-intermediate-strip cathode designs were measured on cathodes at BU and BNL; the rms variation of the capcaitances was less than 1% of the mean value, showing that good uniformity was achieved in the gaps between the strips as well as in their average positions. These results from small prototypes are very encouraging; tests of full-scale cathodes will be an important part of our R&D effort for the coming year.

---

[1] E. Gatti et al., NIM, 163 (1979) 83-92.

[2] E. Weber, Electromagnetic fields, Wiley, New York, 950.

[3] E. Mathieson, to be published. (G. Smith, BNL, editor)

[4] A. Zastawny, J. Sci. Inst., 43 (1966) 179, and
A. Zastawny, J. Sci. Instr., 44 (1967) 395.

[5] J.S. Gordon and E. Mathieson, NIM, 227 (1984) 267-276.

3. Electronics

3.1 Cathode Strip Electronics

The large channel count of the combined endcap/barrel system dictates that the readout electronics be simple and compact. This permits chamber mounting, which in turn sharply reduces the cable plant and its attendant costs. Furthermore, the power dissipation must be low enough to keep thermal gradients in the muon system to an absolute minimum. Fortunately, recent advances in microelectronics make it possible to meet these requirements through the implementation of a highly integrated system.

3.1.1 Signal-to-noise Considerations

The front-end section of the strip readout consists of a charge-sensitive preamplifier that drives a slow shaping amplifier optimized for low noise, and a fast-response amplifier optimized for timing for use in the trigger.

For integration times of 300 ns, the total signal charge collected on one cathode plane is approximately

$$Q_S \simeq q_p\, G_{gas}\, f_b f_g \simeq 90e^- \times (2 \times 10^4) \times 0.4 \times 0.4 = 46 \text{ fC}$$

where q_p is the amount of primary ionization in a 6 mm gap of a 50:50 mixture of CO_2:CF_4, G_{gas} is the gas gain, f_b is the "ballistic deficit factor" used to account for the finite integration time of the charge-sensitive electronics, and f_g accounts for the portion of the charge that is induced on the position-sensitive cathode plane.

For 3-meter-long strips with a floating-strip readout scheme[1], the effective parallel source capacitance is estimated to be about 150 pf, which in the ideal case[2] yields an effective noise charge (ENC) of $\sigma_q \sim 1000e^- = .16$ fC.

If one assumes that the signal charge is spread over three strips and that the position of impact expressed in units of the strip pitch, w, is given by the apparent center-of-gravity of the induced charge, i.e.

$$s = \frac{x}{w} = \mu = \frac{Q_3 - Q_1}{Q_1 + Q_2 + Q_3} = \frac{Q_3 - Q_1}{Q_s}$$

then

$$\sigma_s = \frac{\sigma_q}{Q_s}\sqrt{2 + 3s^2}$$

where $-0.5 \le s \le 0.5$. For $w = 5$ mm and $s = \pm 0.5$ this yields an electronic-noise contribution to the resolution of

$$\sigma x = \sqrt{2.75} w \frac{\sigma_q}{Q_s} \simeq 30 \mu m$$

3.1.2 Preamplifier Design

As noted above, the front end IC noise requirement is ENC < 1000 electrons r.m.s. for a detector capacitance of 80 pF and a shaping time of 300-1000 nsec (in the barrel, the strip capacitances will be somewhat larger).

The equivalent noise charge (ENC) of the preamplifier is given by

$$ENC^2 = \frac{a_1 e_n^2 C_T^2}{t_m} + a_2^2 i_n^2 t_m$$

where a_1 and a_2 are shaping-time form factors of order unity, e_n and i_n are the equivalent input voltage and current noise spectral densities, C_T is the total input capacitance, and t_m is the shaping time.

For a MOS transistor

$$e_n^2 = 4kT\left(\frac{2}{3g_m} + R_g\right) + \frac{a_3 t_m K_f}{C_{ox}^2 WL}$$

where

$$g_m^2 = \frac{2WK_p I_d}{L}$$

where I_d is the drain current, Rg is the gate resistance, K_p is the transistor mobility-capacitance product and K_f is the 1/*f*-noise coefficient.

Given the required ENC, form factors, detector capacitance, and technology parameters Rg, K_p, and K_f, we choose I_d and W to meet the performance goals. This leads to a choice of minimum L, maximum permitted I_d, and an optimization of W. For the Orbit 2μm MOS process, the optimization of W and I_d are shown in figures 3.1 and 3.2 respectively. The noise minimum occurs for a very large gate periphery, but is rather shallow. The low ENC requirement leads to a large drain current, comparable to what is typically used in JFET preamplifiers. A charge-sensitive, folded-cascode preamp was designed in this technology (schematic shown in figure 3.3). For fast shaping (~ 30 ns), this preamp will have a noise of around 3000 electrons.

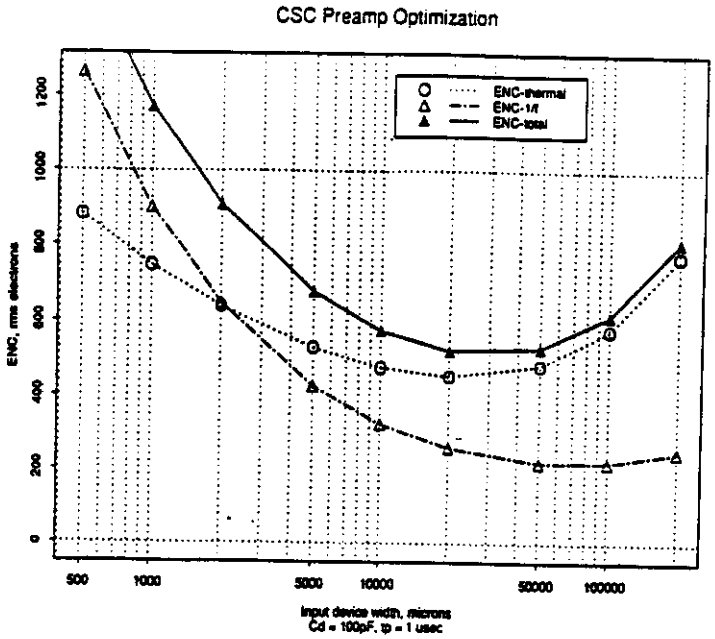

Figure 3.1: Noise versus device width for MOS CSC preamplifier.

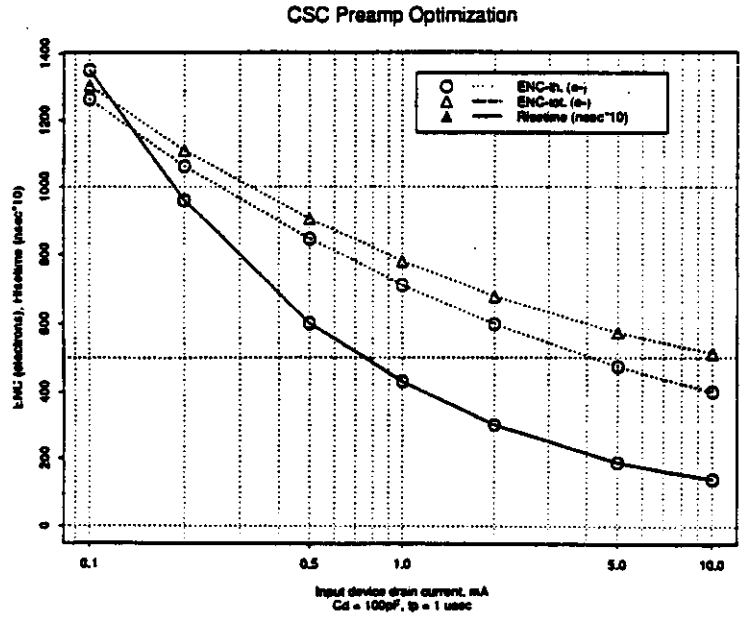

Figure 3.2: Noise versus current draw for MOS CSC preamplifier

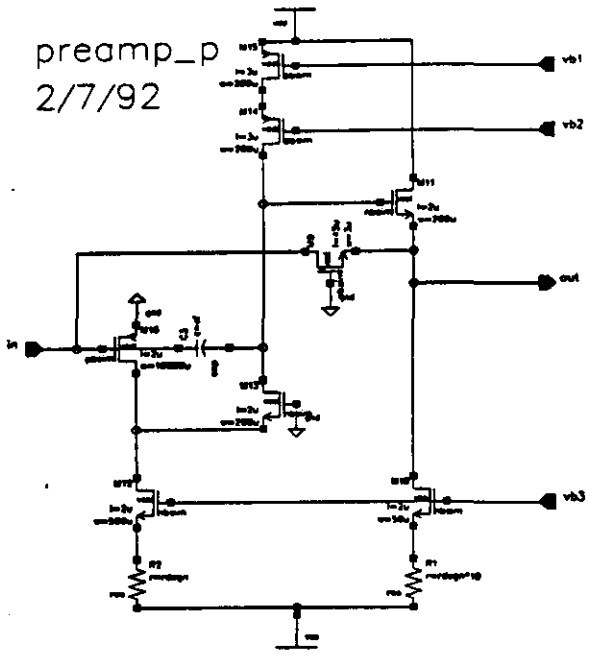

Figure 3.3: Schematic of folded-cascode MOS CSC preamplifier

3.1.3 Shaper Design

We use a passive differentiator followed by two second-order active low-pass sections to achieve a CR - $(RC)^4$ response. The idea of the low-pass section in CMOS is illustrated in figure 3.4 . This configuration gives a peaking time that is tunable by adjusting a bias current, without altering the shape of the response. A shaper using this principle has been designed and fabricated, with a target peaking time of 70 ns. Its step response is shown in figure 3.5, showing a tunability range of about a factor of two. The peaking time varies according to the inverse square-root of the bias current, as predicted.

Using these principles, a shaper with target 1000 ns shaping time has been designed and is expected out of fabrication soon. A layout plot of the chip is shown in figure 3.6.

3.1.4 Readout Architectures

The shaped signals must be sampled and encoded by the on-chamber electronics. At present two basic options are being explored for the sample-and-hold function: i) a double-buffered track-and-hold-capacitor controlled by external data-driven logic, and ii) switched-capacitor array (SCA) sampling.

CMOS Lowpass Section for Semigaussian Shaper

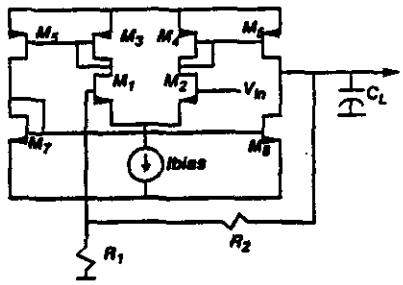

$$\tau_0 = 2g_{m3}/C_i \sim (\text{Ibias})^{1/2}$$

$$Q^2 = \frac{C_i}{g_{m3}}\frac{\beta_5}{\beta_3}\frac{g_{m1}R_1}{(R_1+R_2)C_L} = \sqrt{\frac{\beta_1}{\beta_3}}\frac{\beta_5}{\beta_3}\frac{C_i}{C_L}\frac{R_1}{(R_1+R_2)} \rightarrow$$

- peaking time depends only on (Ibias)
- shape of pulse is determined by component ratios, independent of (Ibias).

Figure 3.4: CMOS low-pass section

Results of Preamp/Shaper Test Chips Designed at BNL

70 nsec variable CMOS shaper

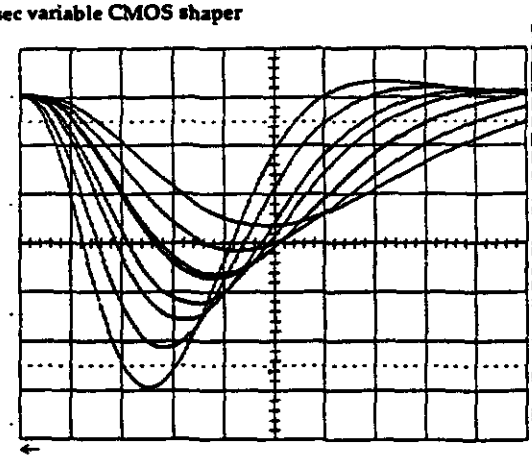

Horizontal: 20 nsec/div

Vertical: 50 mV/div

Figure 3.5: Step response of adjustable shaping amplifier

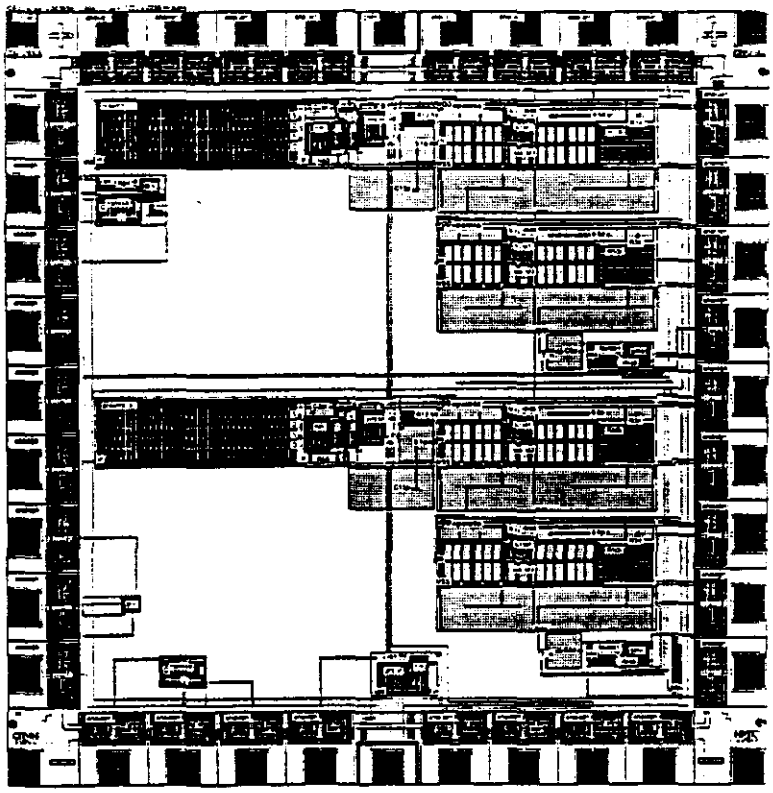

Figure 3.6: Layout MOS CSC shaper IC

3.1.4.1 Track & Hold Readout

The first approach has been simulated in conjunction with a preamplifier, fast (30 ns) shaper, slow (1000 ns) shaper, and track-and-hold (schematic shown in figure 3.7). The output waveforms are shown in figure 3.8. Such a block would form the core a of track&hold-based readout architecture.

3.1.4.1 Switched Capacitor Readout

This approach, which has been extensively described in the literature [3, 4], employs the "virtual pipeline" strategy used in the readout of the GEM central tracker IPC's and the baseline calorimeter electronics. One notable difference, however, is that the longer shaping times and lower count rates in the muon system allow the sampling rate to be reduced to 10 Megasamples per second (MSPS) from the 60 MSPS rate employed in systems that must sample at the bunch crossing frequency.

In the virtual pipeline approach, analog signals are continuously sampled and stored for the 2 μs duration of the Level 1 delay. If the Level 1 accept line is not asserted, samples emerging from the pipeline are discarded. If a Level 1 accept signal is present, however, the next five samples (in practice three or four samples may suffice) to emerge from the end of the Level 1 pipeline are transferred to a Level 2 FIFO buffer, where they await analog-to-digital conversion.

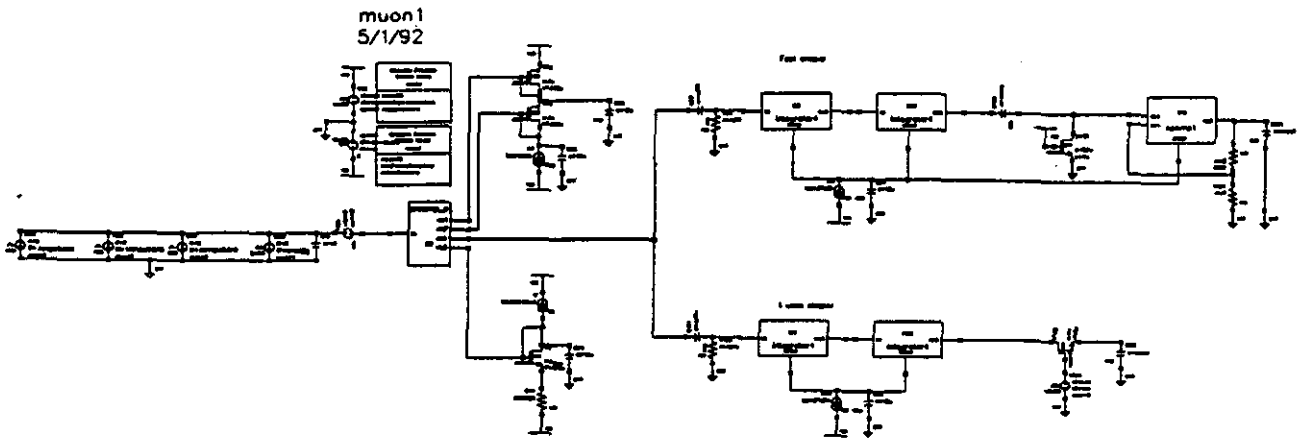

Figure 3.7: Schematic of preamplifier, shaper, track & hold circuit for CSC readout IC

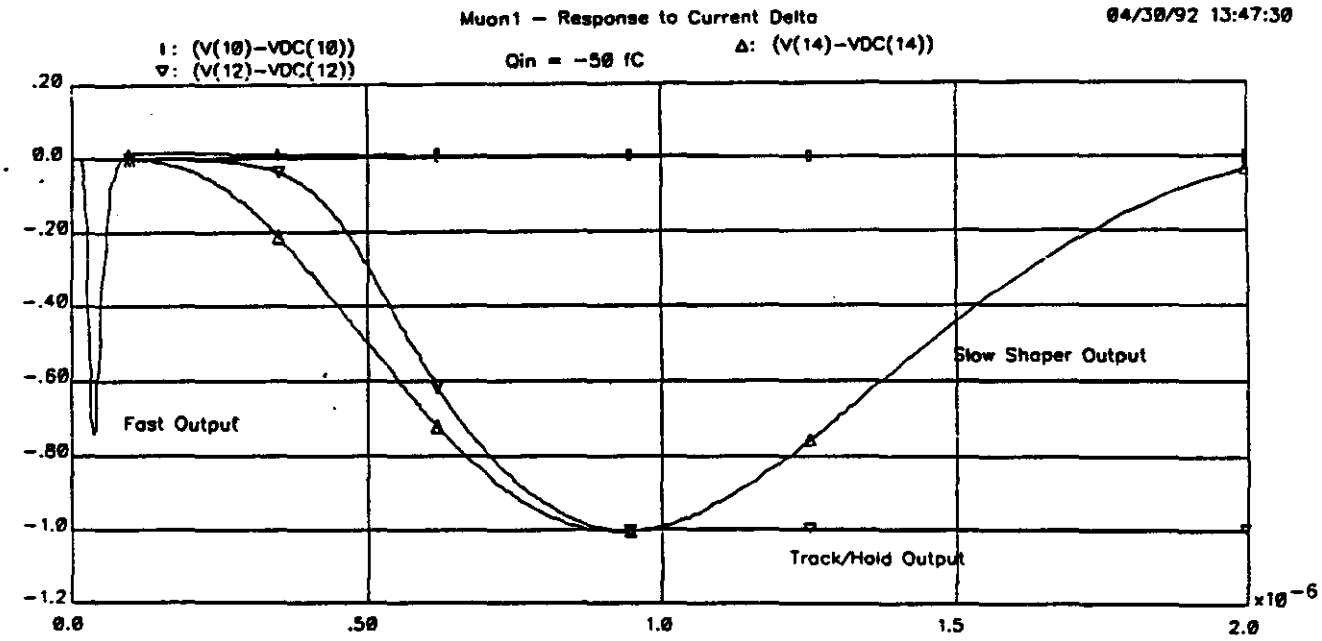

Figure 3.8: Output waveforms of preamplifier, shaper, track & hold circuit for CSC readout IC

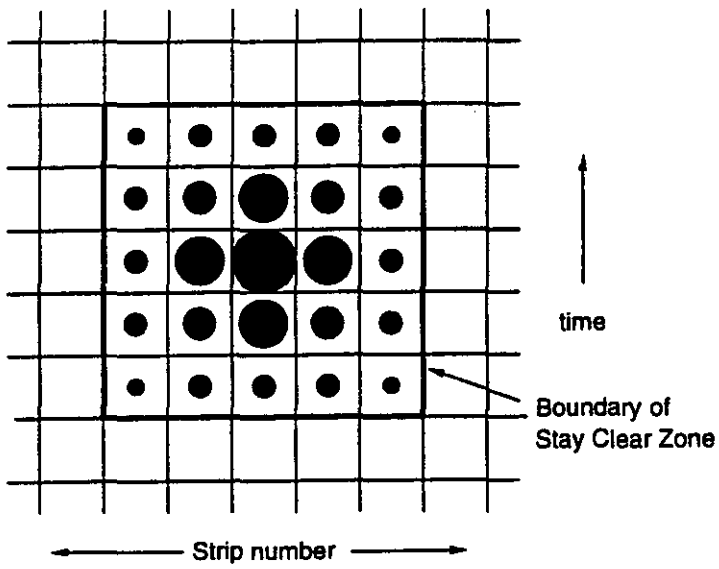

Figure 3.9: Schematic representation of the "space-time" profile of a typical CSC pulse as captured in a CSC array

Although sampling at a rate of less than 60 MSPS may at first seem incompatible with the need to associate hits with their bunch crossing, resolutions that are a fraction of the sampling period can be obtained through interpolation. Indeed, a temporal version of the analysis of section 3.1.1 is applicable for a broad class of pulse shapes.

The SCA approach also offers good immunity against background from accidental pulses. The level at which background becomes a problem can be estimated from figure 3.9, which shows the "space-time" profile of a typical pulse.

The horizontal divisions represent the strips, while the vertical divisions represent the time samples. The size of the circle in each space-time bucket represents the amount of charge. If one assumes that a pulse will be ``spoiled" if a second pulse falls anywhere within the indicated 5×5 stay-clear zone, the probability of spoilage is given by

$$P_{spoil} = 25AT_sR_n = 25\text{x}150\text{cm}^2\text{x}10^{-7}sxr_n \simeq \begin{cases} 0.2\% \text{ for } r_n = 5 \text{ cm}^{-2}\text{ s}^{-1}; \\ 20\% \text{ for } r_n = 500 \text{ cm}^{-2}\text{ s}^{-1}. \end{cases}$$

where A=150 x 0.5 cm^2 is the strip area, T_S is the sample period, and r_n is the *detected* fluence of accidental particles, presumably mostly neutrons. Although a 20% accidental spoilage rate is daunting, we note that this rate corresponds to a highly pessimistic assumption about the neutron backgrounds. Such a scenario presents very serious problems for virtually any muon detection technology. Even so, with CSC's the situation will be salvageable, since it will be known which hits are spoiled and should be dropped from the track fit. The proportion of hits suffering from undetected spoilage, corresponding to hits very close in space and time to the center of figure 3.9 would be approximately one order of magnitude smaller.

As noted above, the SCA approach is also a prime technology candidate for the GEM IPC and calorimeter readouts. SCA development has been the subject of considerable R&D effort in the past few years. In particular, a group at LBL (see references [3, 4, 5]) has developed an SCA that exceeds by a considerable margin the requirements of the CSC readout. Specifically, the LBL devices operate at ≥ 60 MSPS with ≃ 12-bit accuracy. Moreover, for a fixed Level 1 delay time the number of storage elements can be reduced in rough proportion to the sample rate, since each sample effectively provides more delay—i.e. a 60 MSPS pipe uses 120 samples to provide 2 μs delay, whereas only 20 are needed for 10 MSPS operation. Thus the lower sampling rate will not only be less challenging technologically, but will also require less silicon real estate; both simplifications leading to reduced cost.

3.1.5 ADC Dynamic Range and Resolution

Many aspects of the ADC question are common to both the multiple track and hold and the SCA readout approaches. The remarks below will consist of a general discussion of the required ADC resolution and dynamic range, followed by a technology review concentrating mainly ADC's for the SCA approach, since that system places somewhat greater demands on the ADC technology.

Whatever the sampling scheme, the combined accuracy of the sampler/ADC must be one part in 140, or about seven bits. Various other contributions to the overall dynamic range are shown in the table below.

Contribution	Range	No. # bits	See note
Position resolution	S/N = 140:1	7.1	1
dE/dx fluctuations	$40 < N_{ion\ pair} < 230$	2.5	2
Operating margin	×2	1	3

Notes:

1) This contributes ~ 50 μm to the measurement error for the *smallest* energy depositions.

2) This range encompasses ~ 95% of all tracks traversing the 6-mm gap (see figure 3.10).

3) This leaves room for the simple expedient of raising the chamber HV in the event that the electronic noise is larger than anticipated. Since the operating margin contribution is in effect a scale adjustment it is not absolutely necessary to include it in the ADC's dynamic range. Rather, it may prove more economical to employ adjustable-gain buffer amplifiers between the sampling capacitor(s) and the ADC. Even so, ADC's with dynamic range in the range of 9-10 bits will be required.

To be able to sustain the worst-case 100 kHz Level 1 accept rate, the ADC system must be able to convert all samples in less than 10 μs.

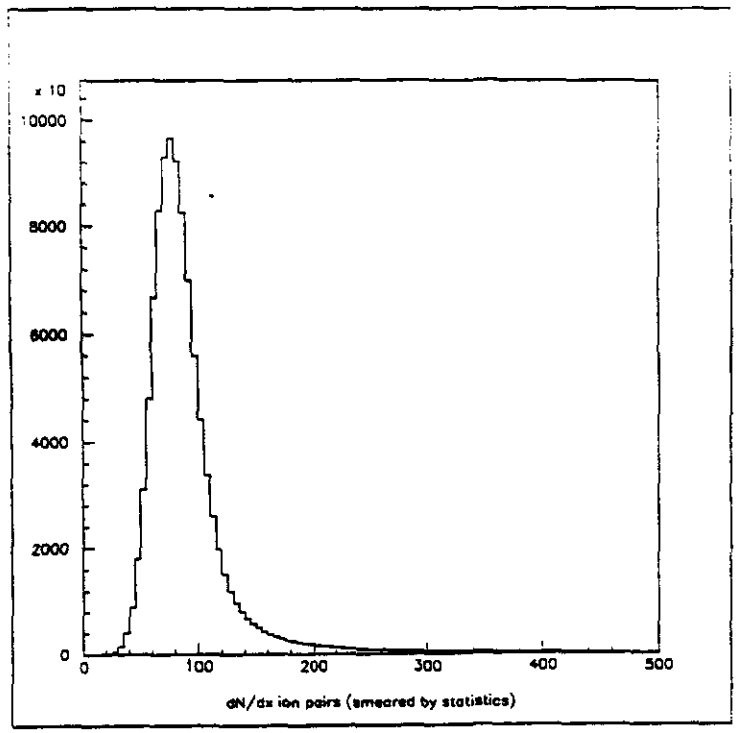

Figure 3.10: Histogram showing dN/dN_{ion} for a 6 mm thickness of CO_2:CF_4

3.1.6 ADC Technology Options

Perhaps the most straightforward option is to equip each channel with its own ADC. Each such ADC must be extremely compact, low in power, and inexpensive. Workers at LBL recently demonstrated a full-custom Wilkinson (ramp down) ADC capable of operating with a 400 MHz clock when implemented in 1.2 μm CMOS process [5]. The LBL design fits 16 channels on a 1.5 $\times$ 4.4 mm^2 chip and consumes less than 10 mW per channel. The maximum conversion time for a Wilkinson ADC is $T_{conv}=2^N T_{clock}$, or 2.5 μs for a 10-bit conversion. However, a 400 MHz rate of operation is near the limit of current CMOS technology. This option appears feasible if just one sample is converted, and with advances in technology may even prove attractive for a five-sample SCA readout.

An orthogonal approach is to use a single high-performance ADC to service several channels. Recently a number of high-speed monolithic ADC's having 10-12 bits of resolution have come on the market. As an example, Signal Processing Technologies offers a 10-bit 40 MSPS device (the SPT9814), which dissipates on the order of one watt and costs $\leq$ \$100 in quantity. Tests at Princeton showed that the SPT9814 can be operated at up to 50 MSPS with only slight loss in resolution. Effective use of such a device requires a high-speed analog multiplexer. Here also suitable devices are commercially available—e.g., Maxim Integrated Products markets a video multiplexer with a 15 ns channel switching time. Assuming five samples per channel and 40 ns per sample, a single ADC could service ~ 50 channels in the allotted 10 μs. It is likely that advances in technology will improve this factor in the next few years.

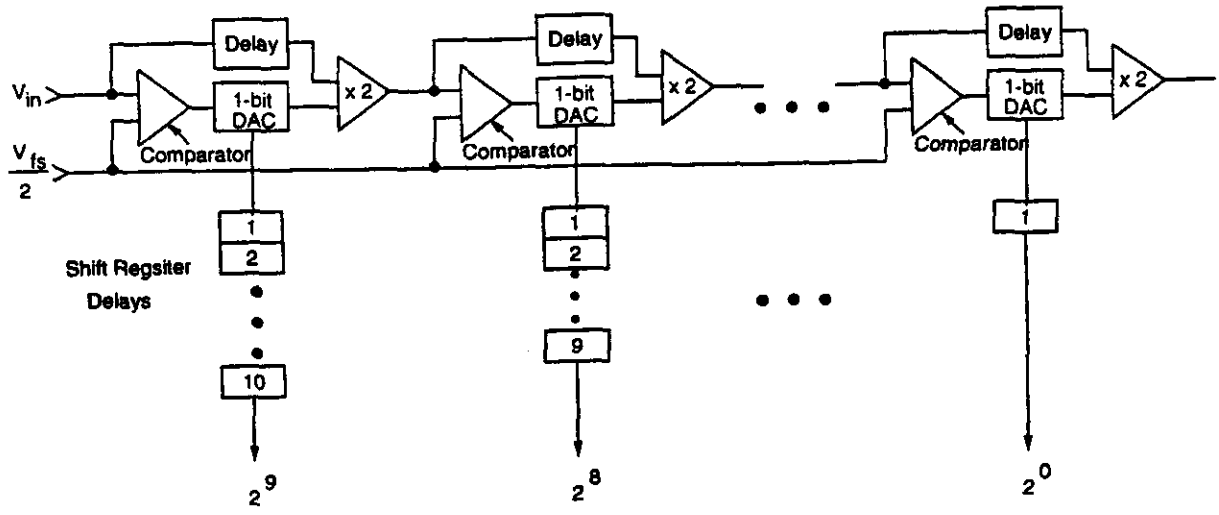

Pipeline ADC Concept

Figure 3.11: Block diagram of pipeline ADC

A third option is to employ "pipeline" ADCs. A simplified block diagram of a pipeline ADC is shown in figure 3.11. The idea is similar to that of the successive approximation ADC, except that the interval-halving approximations are made using independent circuits. An N-bit converter consists of N cascaded stages, each of which compares its analog input to a half-scale reference voltage and generates a residue or "analog remainder" corresponding to two times the difference between its analog input and its (1-bit) quantized digital output. The residue signal is used as the analog input to the next stage. Although the latency between the time an input is first sampled and the time it is fully converted is N T_{clock}, all stages operate simultaneously and produce a new answer every clock cycle. This yields an effective steady-state sample rate of $1/T_{clock}$. Thus even modest (~ few MHz) clock rates result in high throughput rates. A survey of the recent literature reveals designs capable of 12-bit 1-MSPS operation[6,7] as well as a design capable of 9-bit 5 MSPS operation[8]. Although none of these designs is available as a commercial product, all were synthesized as full-custom monolithics, using standard switched-capacitor design techniques. Since SCAs and pipeline ADC's can be implemented in the same technology (CMOS), it should be possible to combine both in a single integrated package, thereby reducing system costs.

Yet another possibility is that with modest improvements in their design, pipeline ADCs can be made to operate with 10-bit precision at 10 MSPS. In this case, "direct encoding" is possible and the need for the SCA and its outboard control logic is eliminated.

In summary it appears that there are a number of attractive options for the backend CSC readout. A detailed evaluation of the relative merits of each is the subject of an ongoing R&D program.

3.2 Anode Wire Readout

The anode wires run in an azimuthal sense in both the barrel and the endcap chambers. The

anode wires are read out to provide measurement of the non-bend coordinate—z in the barrels, r in the endcaps—allowing determination of the polar angle of the track. The anode signals are also used to tag the beam crossing.

The anode wires are operated at high voltage; the cathodes are grounded. Groups of wires are ganged to a single readout circuit; the ganging is by 20 wires (5 cm) in the endcaps and 20 or 40 wires (5 or 10 cm) in the barrel; the slat size is determined by the resolution required to preserve the precision of the momentum measurement and to provide sufficiently precise determination of the polar angle. The appropriate ganging in the barrel is under study by Larry Rosenson. Blocking capacitors couple the anode signals to preamplifiers and shapers. The shapers have a peaking time of order 30 ns, sufficiently longer than the signal propagation time along the roughly meter-long wires that the position dependence of the pulse shape due to reflections etc. is not important. The shaped pulses are discriminated to identify hit anode channels. Due to the variation in muon pulse amplitude, simple threshold discrimination is not adequate to achieve the required time resolution. A number of alternative schemes (dual threshold, zero cross, constant fraction, etc.) are under study.

Electron drift velocities have been measured to be quite high in the CO_2/CF_4 gas mixtures used in the chambers; results are presented elsewhere in this document. With appropriate discrimination, the maximum drift time measured for a single gas gap is expected to be approximately 25 ns. The four chambers in a module will be combined using a ≥ 3 of 4 majority logic requirement. This provides good efficiency for bonafide tracks, while rejecting random backgrounds. In addition, a four-fold OR, gated by the ≥ 3 of 4 signal, will be formed to provide good timing resolution. The logical combinations above will be formed in a way that projects towards the interaction point, reducing sensitivity to random backgrounds. Preliminary results, shown in figure 3.12 from calculations, indicate that the OR of four gaps rises within 12 ns for over 99% of cases, for muons averaged over the impact parameters and angles accepted by a representative module. Calculated distributions for response time from the first, second, third, and fourth chambers in a module are shown in figure 3.12. Tests now in progress at the RD5 test beam at CERN will measure the timing performance of a four-chamber module. Results will be available by early November.

In order to tag the beam crossing it will be necessary to compensate for the position of the track in the active area of the module. This can be accomplished to first order by appropriate delays on the discriminated anode signals. If necessary, it is possible to completely compensate position dependence by mean-timing the anode signals and the fast pickoffs from the cathode signals, which are already being generated for the momentum trigger. The necessity of this correction and ways of accomplishing it are R&D projects for the coming year.

Fig 3.12 CSC timing for the first, second, third, and fourth gaps to fire (out of a four-gap module). Distributions for 1000 muons. traversing the z=11m endcap module covering 11 to 17 degrees in theta.

time (ns)	1st	2nd	3rd	4th
- 4	0	0	0	0
- 3	0	0	0	0
- 2	0	0	0	0
- 1	0	0	0	0
0	270	23	2	0
1	258	118	28	7
2	183	189	55	15
3	92	232	78	40
4	53	148	133	46
5	27	106	110	36
6	27	56	118	45
7	14	35	116	53
8	13	18	72	53
9	8	21	75	62
10	8	15	57	68
11	5	5	35	75
12	2	9	35	61
13	5	12	24	77
14	1	3	27	80
15	3	5	10	53
16	0	4	15	76
17	0	0	7	56
18	1	0	2	45
19	0	0	0	21
20	0	1	1	15
21	0	0	0	10
22	0	0	0	6
23	0	0	0	0
24	0	0	0	0

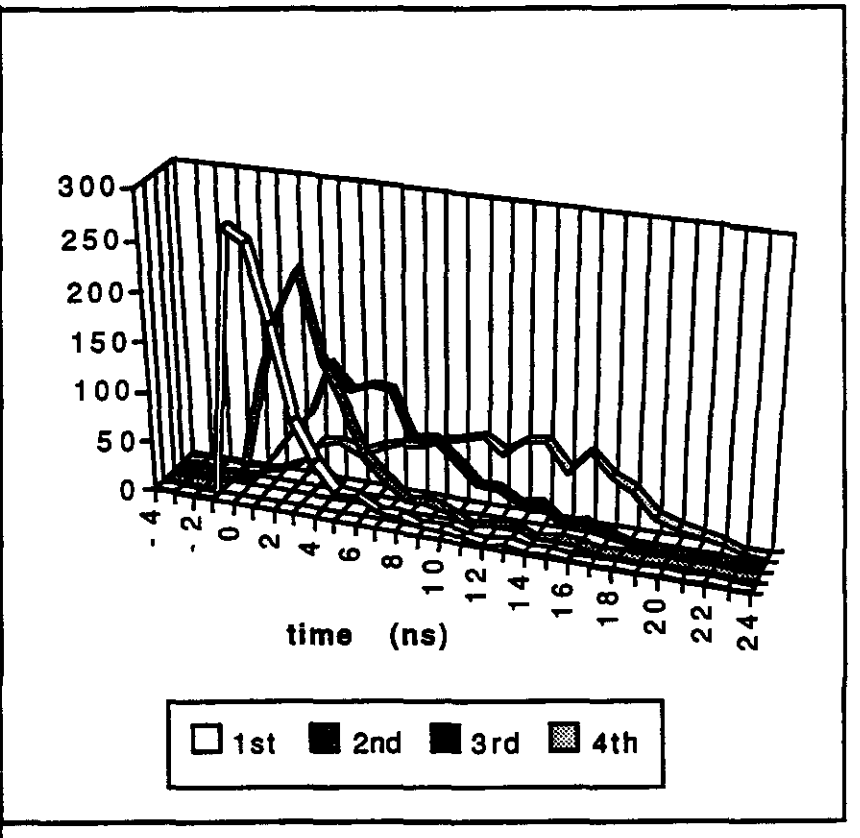

Anode data will be correlated with cathode data of the same timestamp and will be bundled on-board for data acquisition and readout. Details of the data processing will be studied as part of the FY93 R&D program. One alternative approach to non-bend coordinate determination and timing is to read coarse azimuthal strips on the second cathode. The wires then would be operated at high voltage but no blocking capacitors would be required. Readout considerations for the azimuthal strips in this case are otherwise essentially identical to the wire readout scheme discussed above.

3.3 Trigger

An important advantage of the CSC's is their ability to provide information with sufficient spatial and timing resolution for the Level 1 trigger. To a good approximation the CSC's offer the simplicity of scintillator hodoscopes---i.e. good timing resolution combined with low latency and a

spatial resolution set by the physical element size---but at greatly reduced cost and with much less sensitivity to neutrons. These features will result in a trigger design that is simple, robust, and easy to implement. Although some additional circuitry will be needed to reduce the ~ 20 ns time jitter resulting from drift-time variations the gas, this can be readily accomplished using straightforward combinational logic, as discussed in section 3.2.

The basic strategy of the CSC trigger will be to combine the good timing resolution of the anode signals with the fine spatial segmentation of the cathode strips.

3.3.1 Reducing the Time Jitter

The baseline design of the GEM trigger/DAQ system requires that the Level 1 trigger system generate a pulse in time with the bunch crossing of interest. This reduces the effective aperture time of the system and greatly simplifies the overall design of the readout of all systems.

The timing signals for the muon trigger will be derived from the anode planes since their larger pulse heights and smaller capacitances naturally lend themselves to better timing.

The basic idea is to reduce the effects of drift-time variations by generating timing signals based on the arrival time of the first pulse within a superlayer. To suppress potential backgrounds from neutrons, a local ≥ 3-of-4 requirement is imposed and used to gate the timing signal.

Representative logic for a four-plane superlayer is shown in figure 3.13a. The element labeled ≥3-of-4 requires that at least three superlayers within a module fire. The timing properties of its output are poor, however, since its logical requirement is not satisfied until the arrival of the next-to-last (third) pulse. The output of the OR gate is asserted with the first pulse to arrive and exhibits little timing jitter, as shown in figure 3.12. The timing jitter can be further reduced by combining information from a second superlayer, as shown in figure 3.13b. This in effect generates a first-of-eight timing signal.

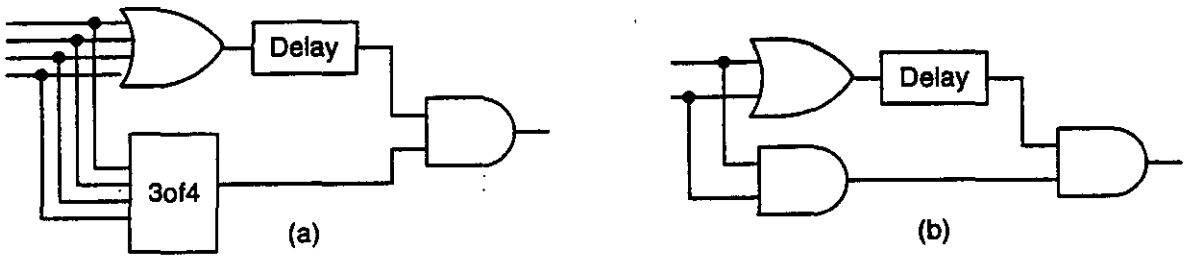

Figure 3.13: Logic for gated timing signals: a) logic to combine four layers of a superlayer; b) logic to combine two superlayers

3.3.2 Imposing the Geometric Requirement

The information from the cathodes strips is used for the momentum-selection part of the trigger. As shown in chapter 5 trigger thresholds up to $P_T^{\mu} > 50$ GeV/c can be imposed with a spatial segmentation of $\simeq 2$ cm, or about four strip widths. As with the anodes, the cathode circuitry must impose some sort of coincidence requirement to eliminate backgrounds from accidental neutron hits. Although a fully optimized design for the Level 1 trigger logic remains to be developed, most designs fall into two broad categories: straightforward brute-force approaches, based on combinational logic; and more sophisticated approaches using content-addressable memories (CAMs). In the paragraphs below a representative version from each category is described. For specificity we assume that a chamber module comprises four planes of 256 strips each and that (for the barrel) each strip is 0.5 cm wide and 300 cm long.

The first step in either approach is to reduce the number of trigger signals per module to a manageable number. In the combinational approach this starts with a bank of four-input OR gates that combine adjacent strips, yielding an effective 2.0 cm segmentation. The remaining superlayer logic is then based on 2-cm-wide "virtual elements" situated between the two middle layers of the superlayer as shown in figure 3.14a. These virtual elements are used in subsequent logic to define P_T^{μ} as described in chapter 5. The superlayer logic, shown in figure 3.14b, requires a coincidence between the OR of the two middle layers and the OR of the outer two layers. This arrangement yields high efficiency—e.g. for a single-layer efficiency of $\varepsilon_1 = 95\%$, the superlayer efficiency is 99.5%—while at the same time providing immunity to neutron-induced singles rates. Each virtual element is matched with a triplet of elements from each of the two outer layers so as to maintain efficiency for inclined tracks. The resulting 64 signals per module are then transmitted to detector-

mounted racks on a pair of high-density flat cables, where they are combined with signals from other superlayers in pair-wise coincidences to form the final P_T^{μ} -defining signal.

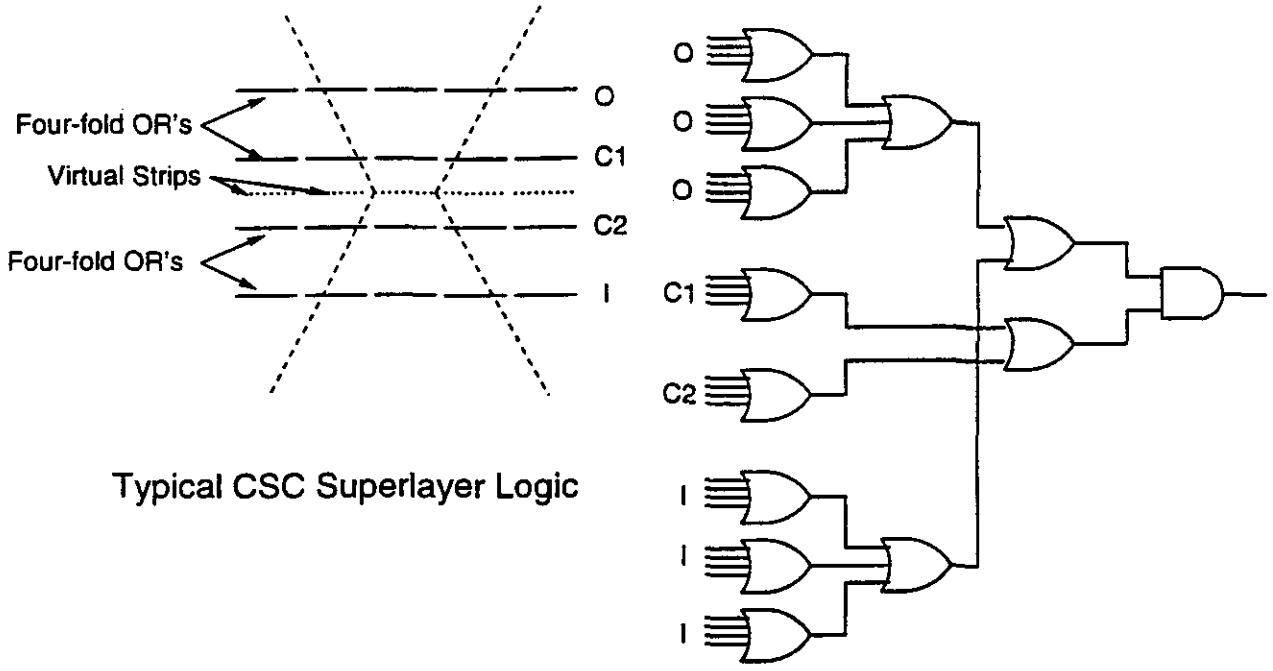

Figure 3.14: Logic of combinational trigger scheme.

Content-addressable or associative memories, here called CAM's, implement logic using table lookups. However, unlike the usual table lookup, where a memory cell is needed for every *possible* input combination, in the CAM, memory cells are implemented only for valid input combinations. In effect one stores a list of only the valid trigger patterns and then checks to see whether or not a given input is on the list. In cases where the number of acceptable trigger patterns is a small subset of the number of possible trigger patterns, the required amount of memory is greatly reduced.

A typical version of the CAM approach is shown in figure 3.15. A ≥ 3-of-4 coincidence on the anode planes is used to strobe the current status of the cathode strip bits into four registers—one for each layer—where the pattern of hits is held for further processing. The latched data are routed to four 256-input priority encoders that determine the eight-bit address of each hit in sequence. Thus each priority encoder generates a list of 8-bit addresses corresponding to the struck strips. The 8-bit addresses from each of the four encoders are combined to form a list of 32-bit addresses that are routed to the CAM memory. The total number of 32-bit addresses presented to the CAM is equal to the number of 8-bit addresses generated by the layer with the most hits. Since the number of hits will in general vary from plane to plane, dummy addresses must be inserted after a plane's address list has been exhausted. The important point is that unlike a sequential tracker finder where the number of "steps" goes like $N_1 \times N_2 \times N_3 \times N_4$, the number of steps in the CAM approach is only max (N_1,N_2,N_3,N_4).

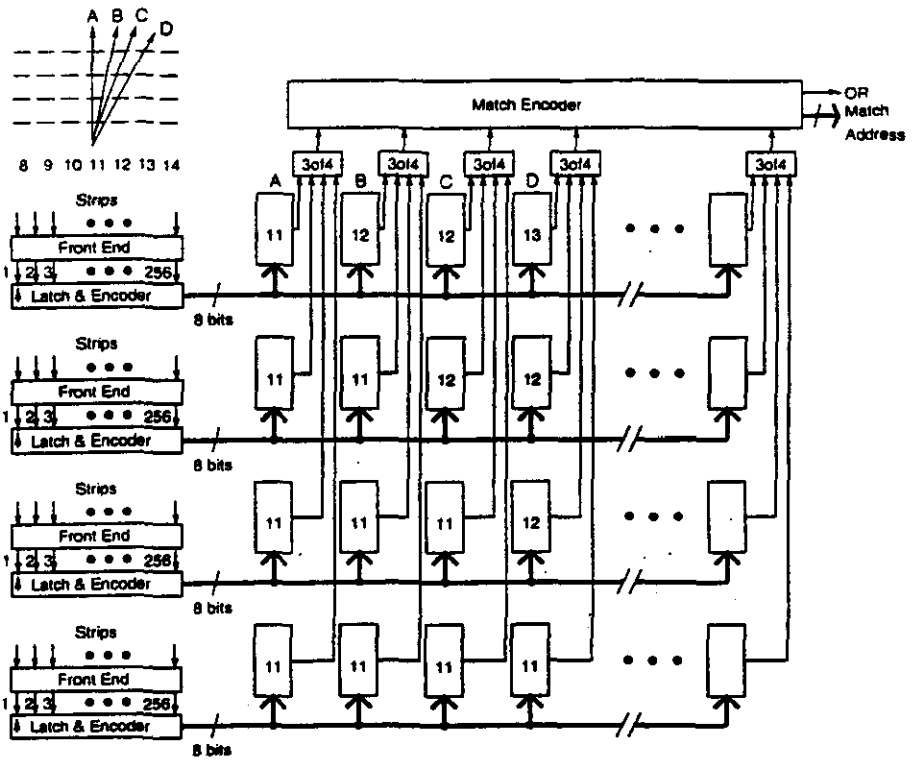

Figure 3.15: Block diagram of content-addressable-memory (CAM) trigger scheme

Inside the CAM (right-hand-side of figure 3.15) each 8-bit subaddress is fed to a series of cells that are preloaded with patterns of valid combinations. Each cell determines whether its eight-bit address matches its contents. The match outputs from the four cells in each column are fed to an encoder that recognizes when three or more of the four cells are matched. The contents of the cells of the first few columns are shown for purposes of illustration. The first term (column) corresponds to a track entering the array at strip # 11 and then proceeding straight through. The next three terms correspond to tracks that are progressively more inclined. To see whether or not a valid track segment is present one merely forms the logical OR of all of the $\geq$ 3–of-4 encoder outputs. To find which term(s) gave rise to the match, the $\geq$ 3-of-4 encoder outputs can be priority encoded. This "match address" information is closely related to the strip number of the strip struck by the track segment, but also carries information about the angle of impact. In the next stage it is then passed on to subsequent layers of the Level 1 muon trigger where it is linked with other track-segment match addresses (using higher level CAM's) to form complete tracks. Note that since the match data is encoded locally it is only necessary to transmit a small amount of data for each match; ~ 10-12 bits, depending on how many bits are added for the angle information. This reduces the amount of data that must be transmitted off chamber.

It appears that either the combinational or the CAM approach will work. The former is straightforward and simple and is fully asynchronous (i.e., it requires no clock). It can be implemented almost entirely using small- or medium-scale integration devices. The latter relies on VLSI techniques and requires some sequential logic, but results in a reduced cable plant and makes more information available to the Level 1 trigger. Detailed studies aimed at determining which option is best are ongoing.

3.4 Calibration

In view of the large number of channels, it is essential that a fully automated calibration system be included as part of the initial design. The CSC readout system lends itself nicely to this since the key parameter of interest is the relative gain of a channel, which can be readily determined with a common pulser and matched capacitors for charge-injection. Experience indicates that with careful layout it will be possible match capacitors on the same chip to the 8-bit level.

The calibration system can also be used for system debugging. By downloading a digital "enable match" bit pattern containing a control bit for each channel, one can turn on arbitrary combinations of channels. The amount of interconnection will be kept to a minimum by serially loading the bit pattern.

3.5 Packaging

The large number of channels and the need to minimize noise pickup dictates that the electronics be chamber mounted. This in turn requires that the electronics be compact and reliable. For planning and costing purposes, we assume that the cathode electronics will reside on standard chamber cards of 64 channels each. A conceptual design for this card is shown in figure 3.16. Although mounted directly on the chambers the cards will be removable for repair.

The amount of cabling will depend somewhat on the trigger scheme, but in all cases will be kept to a minimum (i.e. one or two flat cables or optical fibers carrying digital data per chamber module). This will minimize cost and maximize reliability.

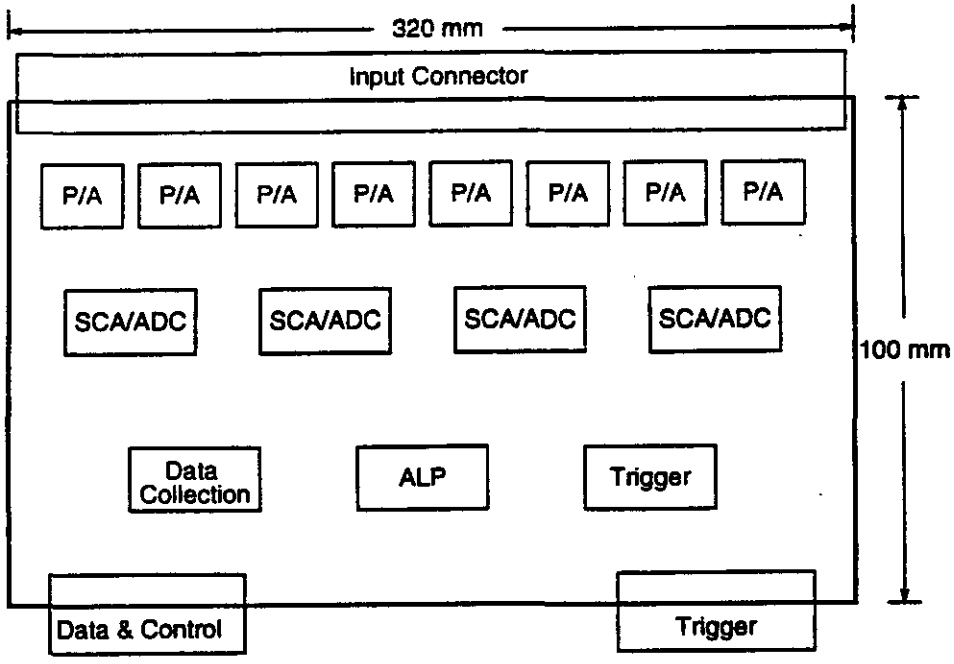

Figure 3.16: General layout of CSC cathode board

3.6 Cost

The cost of the readout electronics will be kept to a minimum by including it as a prime consideration throughout the design process. To this end, the design will be based on full-custom monolithics and incorporates a minimum of number of interconnections.

To date two estimates of the cost of the CSC electronics have been made. The first was done by members of GEM working in collaboration with engineers from LeCroy corporation[9]. The thrust of the LeCroy effort was to make a preliminary determination of the total cost of the complete GEM electronics, trigger, and data acquisition (DAQ) chain. Limitations on the time and resources available for this work and the preliminary state of the designs led its authors to adopt a parametric approach to costs based on a simplified model. The second cost estimate effort---now or soon to be underway for all GEM readout subsystems---employs a "botton-up" methodology, based on better-defined designs. In what follows we present the first results from this process for the CSC electronics.

Since the cost of the cathode-strip readouts dominates the cost of the front-end electronics, that has been the initial focus. The estimate assumes a design based on the SCA readout scheme, with an ADC integrated onto the SCA chip. The chips are mounted on a standard 64-channel readout card, whose basic layout is shown in figure 3.16. In addition to the preamp-shaper and the SCA/ADC, the board includes a digital Address List Processor (ALP) chip for control of the SCA read and write address lines, a Data Collection Chip (DCC) for the first level of data acquisition, and a chip for the first level of trigger processing. Table 3.2 shows a summary of the cost of the various components and the various construction and test steps that are needed for a complete board. The notes associated with each row explain the basis for each estimate.

Item	$/Board	$/Chan	see note
IC's (see table 3.4)	$ 281	$ 4.39	1
PCB Fabrication	$ 48	$ 0.75	2
Connectors (Male & Female)	$ 64	$ 1.00	3
Misc. Parts	$ 20	$ 0.32	4
PCB Assembly	$ 90	$ 1.41	5
Q/A	$ 10	$ 0.16	6
Test	$ 30	$ 0.47	7
Rework	$ 12	$ 0.19	8
LVPS	$ 64	$ 1.00	9
Mounting Hardware	$ 20	$ 0.31	4
Packing and Shipping	$ 20	$ 0.31	4
Subtotal	$ 659	$ 10.30	
Contingency (30%)	$ 198	$ 3.09	10
Total	$ 857	$ 13.40	

Table 3.2 Summary of costs for 64 channel CSC readout board

Notes:

1) IC costs are based on a cost model used by an SDC group from LBL [5]. A second model based on vendor (ORBIT's 1.2 micron CMOS process) quotes makes somewhat different assumptions but yields similar results [10]. The chips areas are based on actual designs, or, in the case of the SCA/ADC on extrapolations from comparable designs.

2) Assumes 8-layer board of dimension 32 x 10 cm^2 and $ 0.25/square inch of layer pair. The latter figure is based on detailed discussions with U.S. and Canadian PCB vendors and is the same as that used by various SDC groups.

3) Based on count of input and output connectors and on actual costs encountered in the preparation of prototype electronics. Actual costs may be lower due to competive bidding on a large-quantity order.

4) Engineering judgment.

5) Assumes 1500 leads per board at $ 0.06 per lead. Our discussions with vendors indicated a cost of $ 0.03 per lead, but we have adopted the higher figure employed by SDC.

6) Assumes 20 minutes per board at $ 30/hour.

7) Assumes one-hour per board at $ 30/hour. Testing will be highly automated.

8) Assumes 20% of the boards require two hours of rework at $ 30/hour.

9) Assumes 200 mW/channel at $ 5/W delivered to the chambers.

10) A detailed element-by-element contingency analysis has not been performed.

SDC IC Costing Rules						
Size	**Area**	**Yield**	**Fab.**	**Pkg.**	**Test**	**Total**
Tiny	6.8 mm^2	70%	$2.05	$1.00	$7.50	$10.55
Small	35 mm^2	65%	$11.17	$1.50	$8.00	$20.67
Medium	50 mm^2	60%	$17.65	$2.00	$8.50	$28.15

Table 3.3 Summary of IC Costing Rules Employed by SDC

Non-recurring expenses (NRE): (not included)

— $25K per design for masks

— $ 5K per design for testing setup

CSC IC's			
Description	**Type**	**Chans/Pkg.**	**$/Chan.**
P/A Shaper	Tiny	8	$1.32
SCA/ADC	Medium	16	$1.75
ALP	Medium	64	$0.44
DCC	Medium	64	$0.44
Trig	Medium	64	$0.44
Total			$4.39

Table 3.4 List of IC's Needed for CSC System.

Tables 3.2 through 3.4 do not include the fixed one-time costs of research, development, and design or the various NRE charges associated with fabrication of IC's and PCB's. The LeCroy estimate for the fixed costs of the endcap CSC cathode readout system is $ 2.7 M including contingency.

There are three items that by GEM convention are included as part of the front-end electronics WBS but are not included in table 3.2. These are the chamber HVPS and cable (one per 1000 channel chamber @ $ 200/set) a fiber-optic data link for connection to the Level 2 trigger and the data acquisition (one per 1000-channel chamber at $ 370/ea), and a 20 m 32-pair cable to the on-detector Level 1 trigger crate (120/ea). Taken together, these items add another $ 0.69 ($ 0.90 with 30% contingency) to the per-channel cost. Including these costs brings the total per-channel cost including contingency to $ 14.30.

The design of the second coordinate readout is not sufficiently well defined to allow for a cost estimate. However, if one assumes that the cost of the anode (or coarse strip) electronics will be the same as that of the cathodes the total production cost of the front-end electronics cost for the CSC system is $ 16.9 M, which when added to the fixed cost of $ 2.7M yields a grand total of $ 19.6 M.

The rest of the trigger and data acquisition electronics are included in separate portions of the GEM electronics WBS. Considerable design effort is needed before bottom-up estimates of the costs of these systems can be generated. Absent detailed designs for the higher levels of either the CSC or the drift-technology Level 1 triggers it is reasonable to assume that the costs for these systems will be the same.

References

[1] See e.g. G.C. Smith, J. Fischer, & V. Radeka, IEEE Trans. Nucl. Sci., NS-35 (1988) 409.

[2] V. Radeka, Ann. Rev. Nucl. Sci. 38 (1988) 217.

[3] "Toward a 60 MHz Analog Virtual Pipeline Integrated Data Acquisition System," Nucl. Phys. B (Proc. Suppl.) 23A (1991), 382.

[4] C. Blocker *et al*, "Front End Electronics Development for SSC Detectors," SSC Subsystem R&D Progress Report and Renewal Request, (1991).

[5] "Calorimeter and Shower Max Electronics: 1992 Progress Report on Conceptual Design, Cost, Schedule, and Critical R&D," SDC Note prepared for the SDC Calorimeter Electronics Review Committee, (unpublished) Sept. 1992.

[6] F. Anghinolfi, *et al*, Nucl. Phys. B (Proc. Suppl.), 23A (1991), 389-394.

[7] B.-S. Song, M.F. Tompsett, and K. R. Lakshmikumar, IEEE J. Solid-State Circuits, Vol 23. (1988), 1324.

[8] S.H. Lewis and P.R. Gray, IEEE J. Solid-State Circuits, Vol SC-22 (1987), 954.

[9] "GEM Electronics Cost Estimate," N. Lau, D. Marlow, R. Sumner, GEM IN-92-12 (June 1992).

[10] Private communication, Ray Yarema, FNAL.

4. CSC Alignment

The position error budget for the CSC's has three components:

- the single layer resolution — 75 μm
- the chamber internal alignment — 50 μm
- superlayer-to-superlayer alignment — 25 μm

where the layer resolution is the random error on a measurement, the internal alignment is the tolerance on distortion of the plane coordinate system, and the external alignment is the tolerance on the average plane position error relative to other modules. The alignment system is required to determine muon hit positions within these tolerances.

CSCs have two important advantages from the point of view of alignment:

1. Internal chamber alignment is integral to the cathodes. The only element with high precision requirements is the strip board, which can be produced by industrial processes. (See section 2 for prototype measurements and section 6 for discussion of industrialization.)

2. CSCs have a minimum number of alignment transfers from precision element (strip board) to alignment devices, and the precision of this transfer can be verified optically during and after production because precision reference marks on a strip board can be placed outside the closed chamber volume.

The precision of CSC chambers can be verified after production in a convenient way using X-rays. Preliminary results show that, by using an X-ray generator or an X-ray source and adding xenon to the gas mixture during chamber tests (for better X-ray absorption in gas), it is possible to verify chamber precision with the required accuracy.

External alignment of the CSC's is similar to other technologies and depends on the details of the chosen alignment scheme. The CSC approach is insensitive to some potentially important sources of alignment error. For example, the orientation and limited length of the CSC anode wires and the limited way in which they participate in the coordinate determination render the contribution of wire sag to the position error negligible. The most nontrivial part of the external alignment is the measurement of the deviation of chambers from their design plane; in the barrel, this could be gravitational sag. The position measurement by cathode strip interpolation is quite insensitive to such a displacement. For example, simulation has shown that in the barrel, gravitational sag of up to 400 μm implies a muon sagitta error of less than 12 μm rms, half the external alignment tolerance. The calculation averaged the error over the module, assuming fixed boundary conditions at the two (strip) ends only. Achievable flatness of the modules in any orientation with respect to gravity will be much smaller than such a gross displacement as 400 μm.

A possible alignment scheme using projective straightness monitors for chamber towers is shown for barrel and end-cap sectors in Fig. 4.1. In this scheme straightness monitor readings can be used for quadratic interpolation inside a tower which allows us to take into account not only

chamber movements, but also some chamber deformations (like torque) and temperature change (in quadratic approximation). This work is discussed in detail in a note by G. Mitselmakher and A. Ostapchuk, "New Approach to Muon System Alignment," in preparation.

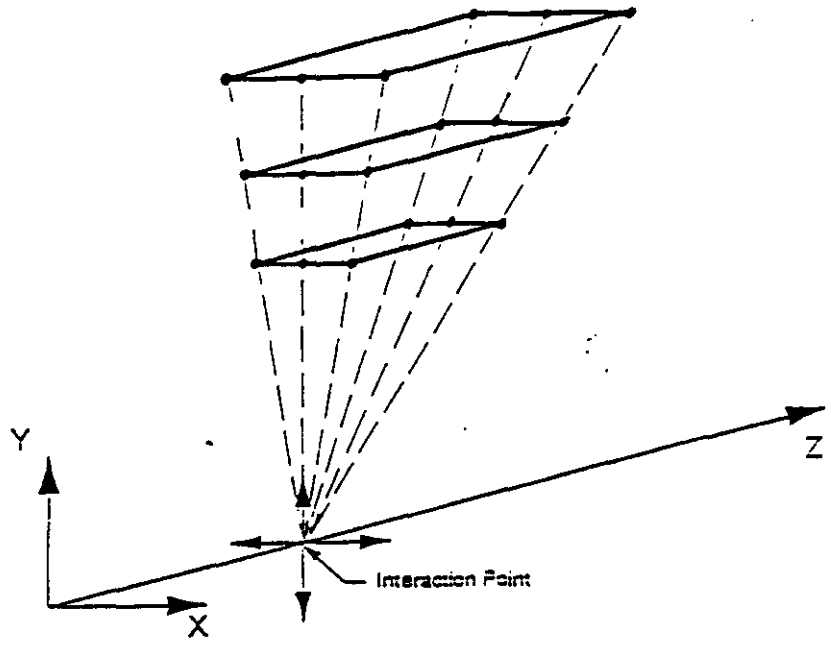

Muon Barrel Module

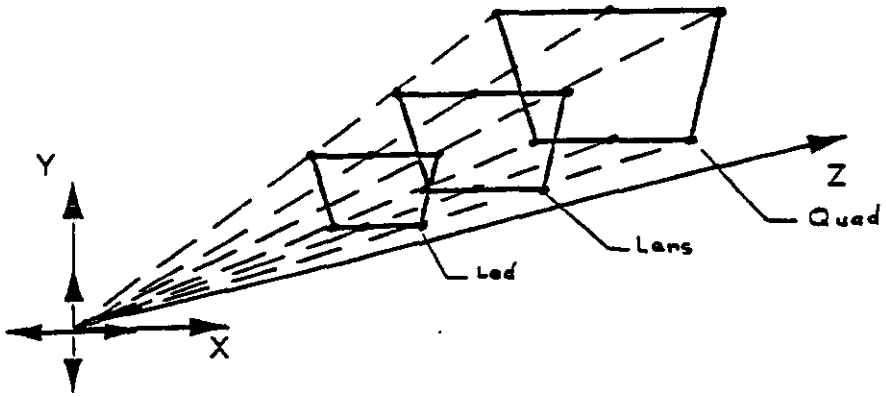

Muon Endcap Module

Fig. 4.1 Projective alignment paths for straightness monitors

5. Performance

5.1 Momentum Resolution

Momentum resolution for a muon system with CSCs in the barrel and in the endcap was studied using a parametric analysis that included chamber measurement error, internal and external alignment errors, multiple scattering, and the nonuniform magnetic field (J. Sullivan). The configuration had 8 layers in the first supermodule and 4 layers in the second and third superlayers. The chamber parameters were the same as for the baseline endcap CSCs: 75 μm chamber precision, 50 μm internal alignment error, and 25 μm external alignment error. The modules were assumed to be overlapped for full coverage of solid angle. A muon passing normally through the active region of a module traverses 0.104 X0; a muon passing through the frame of one module and the active region of another traverses 0.878 X0. Resolution was calculated for each of these two cases. The overlap region comprises about 10% of the total. Figure 5.1 presents the results: fig 5.1a is the momentum resolution vs eta for eight choices of transverse momentum, for the GEM baseline chamber configuration. Figure 5.1b shows the momentum resolution for a CSC muon system, assuning muons do not pass through overlapping modules; figure 5.1c shows the momentum resolution for muons passing through the overlap of two modules. Data for these plots are presented in table 5.1. The calculations show that the CSC system performance is essentially the same as the GEM baseline. It also shows that the resolution degradation due to multiple scattering in the added material where chambers overlap is not severe.

We have also studied the effect on momentum resolution when hits are lost in the first and/or second modules due to overlapping tracks or random background. The calculation described above was carried out while varying the number of hits in the first module from the nominal 8 to either 4 or 1 good hit(s), keeping 4 hits in the second and third modules. It was assumed in this study that spoiled hits could be recognized and rejected (see the discussion of two-track resolution later in this document).The calculation was repeated assuming only 4 hits in the first module, 4, 2, or 1 good hit(s) in the second module, and 4 hits in the third. (In the endcap region, the baseline configuration is 8/8/4 for theta below 11.45 degrees, so in that region there are always 4 more hits in the middle module). The calculation was done for two values of transverse momentum: 100GeV/c and 500 GeV/c.

The results of this study are presented in figure 5.2 and in table 5.2. Loss of hits in the first module has very little effect on resolution. Loss of hits in the second (middle) module degrades the resolution only slowly. This study establishes that the CSC system has momentum resolution that is robust against loss of chambers due to overlapping tracks or random background, assuming the good hits can still be recognized. The pattern recognition aspects of the problem are discussed later.

Table 5.1 ΔPt/Pt vs eta for selected Pt values and different Muon System configurations.

GEM Muon Rev 2: 3/30/92

eta	Pt values 10	25	50	100	250	500	750	1000
0.070	0.010	0.010	0.011	0.013	0.025	0.048	0.071	0.094
0.250	0.009	0.009	0.010	0.013	0.024	0.045	0.067	0.089
0.500	0.009	0.010	0.010	0.013	0.023	0.044	0.065	0.087
0.750	0.010	0.010	0.011	0.013	0.023	0.044	0.065	0.086
1.000	0.011	0.012	0.012	0.014	0.025	0.046	0.068	0.091
1.160	0.013	0.014	0.014	0.017	0.028	0.052	0.076	0.101
1.320	0.019	0.019	0.020	0.023	0.038	0.068	0.100	0.132
1.360								
1.430	0.014	0.015	0.016	0.020	0.037	0.069	0.102	0.135
1.700	0.015	0.016	0.018	0.025	0.051	0.099	0.147	0.196
1.900	0.015	0.016	0.019	0.027	0.060	0.117	0.175	0.233
1.910	0.015	0.016	0.018	0.026	0.054	0.105	0.157	0.208
2.200	0.012	0.014	0.017	0.026	0.059	0.117	0.174	0.232
2.460	0.015	0.016	0.019	0.028	0.061	0.120	0.179	0.238

CSC 8,4,4; 4,4,4; 4,4,4; 4,8,4 Centers

0.070	0.014	0.014	0.014	0.016	0.024	0.042	0.062	0.081
0.250	0.013	0.013	0.013	0.015	0.023	0.039	0.057	0.076
0.500	0.013	0.013	0.013	0.015	0.022	0.038	0.055	0.073
0.750	0.014	0.014	0.015	0.016	0.023	0.039	0.056	0.074
1.000	0.017	0.017	0.017	0.019	0.026	0.043	0.062	0.081
1.160	0.021	0.022	0.022	0.023	0.032	0.052	0.074	0.097
1.320	0.043	0.043	0.044	0.046	0.061	0.098	0.139	0.181
1.360								
1.430	0.012	0.012	0.014	0.018	0.036	0.068	0.102	0.135
1.700	0.013	0.014	0.016	0.023	0.050	0.099	0.147	0.196
1.900	0.012	0.013	0.017	0.026	0.059	0.117	0.175	0.233
1.910	0.013	0.013	0.016	0.024	0.053	0.105	0.156	0.208
2.200	0.010	0.012	0.015	0.025	0.059	0.116	0.174	0.232
2.460	0.012	0.013	0.017	0.027	0.061	0.120	0.179	0.238

"Thick" CSC 8,4,4; 4,4,4; 4,4,4; 4,8,4 Center plus overlapping frame

0.070	0.040	0.040	0.040	0.041	0.045	0.057	0.072	0.090
0.250	0.038	0.038	0.038	0.038	0.042	0.053	0.067	0.084
0.500	0.038	0.038	0.038	0.038	0.042	0.052	0.065	0.081
0.750	0.041	0.041	0.041	0.042	0.045	0.055	0.068	0.083
1.000	0.049	0.049	0.049	0.050	0.053	0.063	0.077	0.093
1.160	0.062	0.062	0.062	0.063	0.067	0.078	0.094	0.113
1.320	0.124	0.124	0.124	0.125	0.132	0.152	0.181	0.215
1.360								
1.430	0.035	0.035	0.035	0.037	0.048	0.076	0.107	0.139
1.700	0.037	0.037	0.038	0.042	0.061	0.104	0.151	0.199
1.900	0.035	0.035	0.037	0.042	0.068	0.122	0.178	0.235
1.910	0.036	0.036	0.037	0.042	0.063	0.110	0.160	0.211
2.200	0.030	0.030	0.032	0.038	0.065	0.120	0.177	0.234
2.460	0.035	0.035	0.037	0.042	0.069	0.124	0.182	0.240

Fig. 5.1a
Momentum resolution in the GEM baseline.

Resolution vs eta for Pt:

1000	GeV
750	"
500	"
250	"
100	"
50	"
25	"
10	"

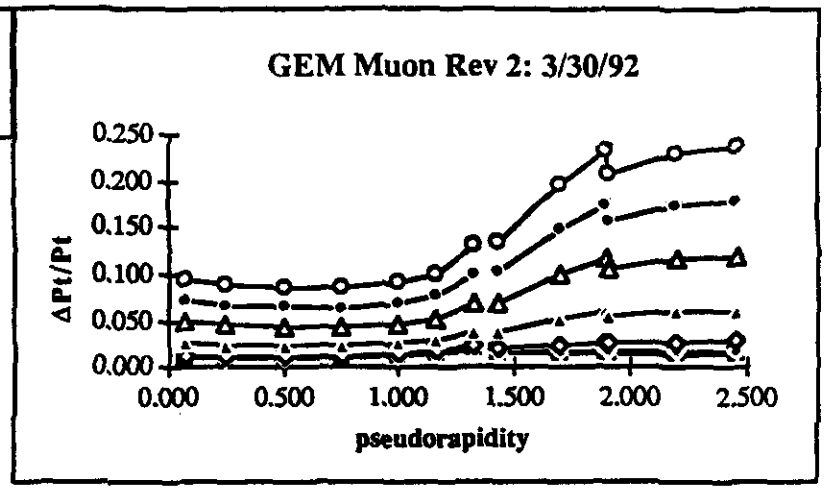

Fig. 5b
Momentum resolution for CSC's -- muons through the centers of the modules.

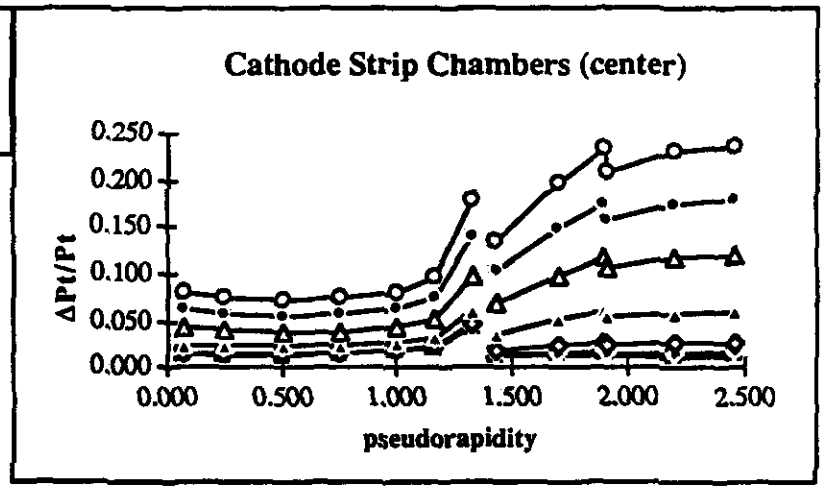

Fig. 5.1c
Momentum resolution for CSC's -- muons through the overlap region: center of one module and frame of another.

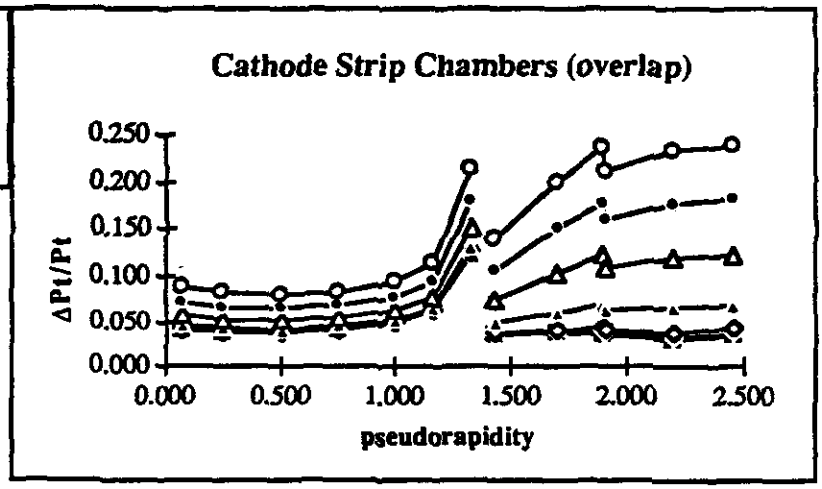

Table 5.2 Momentum resolution for Pt = 100 and 500 GeV versus pseudorapidity, varying the number of useable hits in the first and second modules from the nominal 8/4/4 (except that 8/8/4 is nominal below 12.45 degrees.)

Hits per module	8 4 4 / 8 8 4	8 4 4 / 8 8 4	4 4 4 / 4 8 4	4 4 4 / 4 8 4	1 4 4 / 1 8 4	1 4 4 / 1 8 4
eta \ Pt	100	500	100	500	100	500
0.07	0.016	0.042	0.016	0.044	0.017	0.051
0.25	0.015	0.039	0.015	0.041	0.016	0.048
0.5	0.015	0.038	0.015	0.039	0.016	0.046
0.75	0.016	0.039	0.016	0.040	0.017	0.047
1	0.019	0.043	0.019	0.044	0.019	0.052
1.16	0.023	0.052	0.024	0.053	0.024	0.062
1.32	0.046	0.098	0.046	0.101	0.048	0.116
1.36						
1.43	0.018	0.066	0.018	0.068	0.020	0.081
1.7	0.023	0.095	0.023	0.099	0.026	0.117
1.9	0.026	0.113	0.026	0.117	0.030	0.139
1.91	0.024	0.102	0.024	0.105	0.027	0.120
2.2	0.025	0.113	0.025	0.116	0.029	0.134
2.46	0.026	0.114	0.027	0.120	0.032	0.147

Hits per module	4 4 4 / 4 8 4	4 4 4 / 4 8 4	4 2 4 / 4 6 4	4 2 4 / 4 6 4	4 1 4 / 4 5 4	4 1 4 / 4 5 4
eta \ Pt	100	500	100	500	100	500
0.07	0.016	0.044	0.017	0.053	0.019	0.068
0.25	0.015	0.041	0.016	0.049	0.018	0.063
0.5	0.015	0.039	0.016	0.047	0.018	0.060
0.75	0.016	0.040	0.017	0.048	0.018	0.061
1	0.019	0.044	0.020	0.053	0.021	0.067
1.16	0.024	0.053	0.025	0.064	0.026	0.081
1.32	0.046	0.101	0.048	0.120	0.052	0.151
1.36						
1.43	0.018	0.068	0.020	0.084	0.025	0.108
1.7	0.023	0.099	0.027	0.121	0.034	0.156
1.9	0.026	0.117	0.031	0.144	0.039	0.185
1.91	0.024	0.105	0.028	0.128	0.035	0.166
2.2	0.025	0.116	0.030	0.143	0.038	0.185
2.46	0.027	0.120	0.028	0.126	0.029	0.131

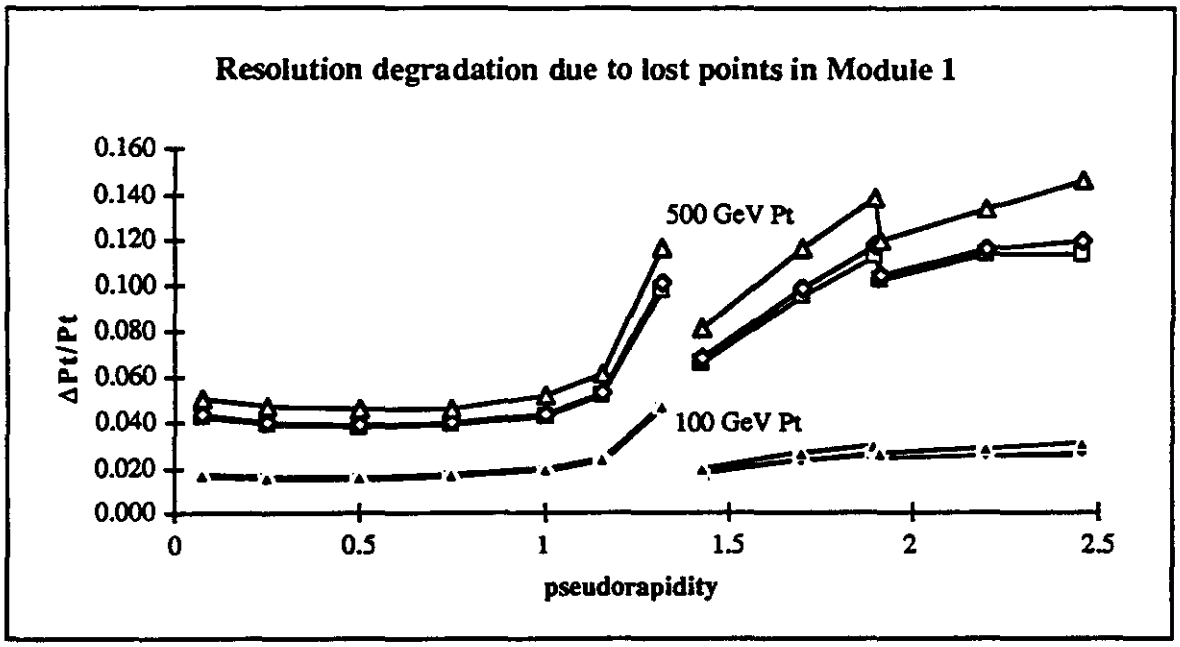

Fig 5.2.a Momentum resolution for 100 or 500 GeV Pt vs eta, for 8, 4, or 1 hits in the first module and 4 hits each in the second and third modules.

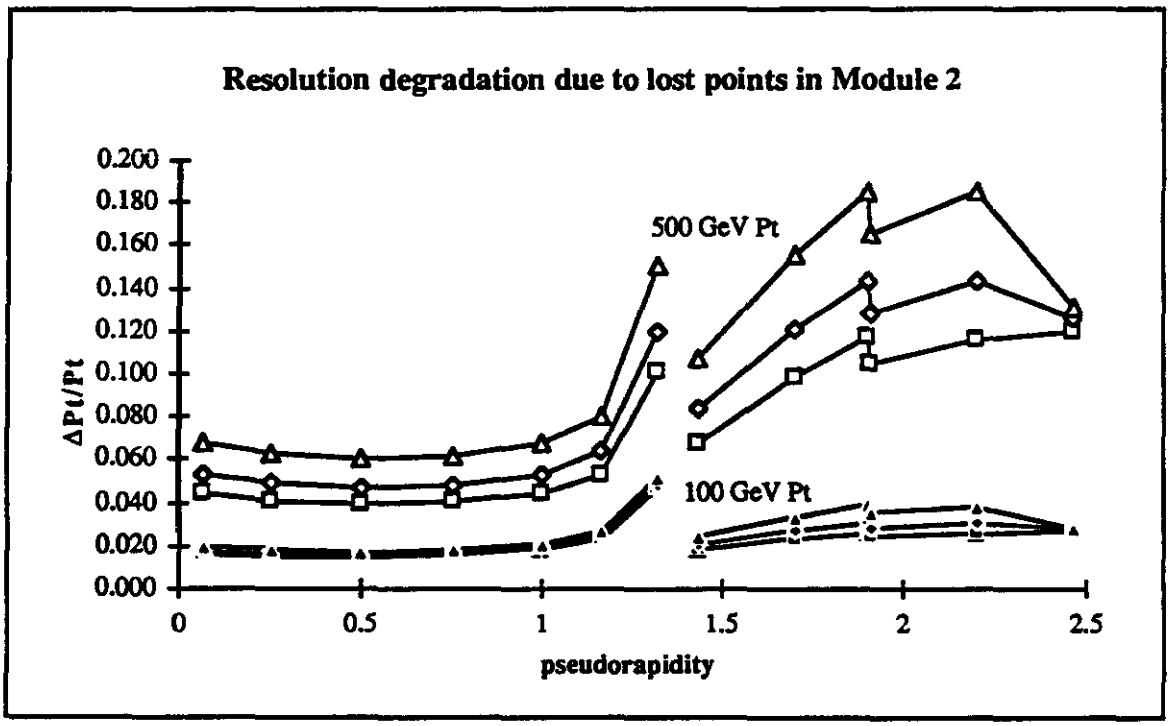

Fig 5.2b Momentum resolution for 100 or 500 GeV Pt vs eta, for 4 hits in the first and third modules and 4, 2, or 1 hits in the second module (8, 6, 5 hits below 12.45 degrees).

5.2 Rate and Occupancy

In this section, we examine the rate of charged particles emerging out of the calorimeter and entering the first superlayer (SL1) of the muon system in the barrel and endcap regions. The other two superlayers are exposed to lower rates of particles as soft charged particles, which make it to SL1, will bend and not reach the others. Although, these particles may turn around and hit SL1 for a second time. From charged particle fluxes, the expected chamber occupancies are calculated.

The Hit-level Monte Carlo simulation package was used for this study.

This package provided trajectories of muons in the muon system in the form of hits in chamber layers. The muon system geometry was based on the parameters of the Baseline 1 [2]. The solenoidal field of 0.8 T was properly simulated including the non-uniformity in the forward regions due to presence of the flux concentrator.

QCD two jet events were generated using ISAJET in the jet Pt range of 4 GeV/c to 2 TeV/c. Decay in flight of pi/K mesons inside the inner tracker volume were simulated using GEANT. Tracks with $|\eta|< 3$ were then passed through a calorimeter modeled in depth to have: flat 12 lambda in the barrel ($|\eta|$=0.0 to 1.5), ramped up to 14 λ($|\eta|$=1.5 to 2.0), and flat 14 lambda in the endcap ($|\eta|$=2.0 to 3.0). The material was a homogeneous mixture of copper and liquid argon for the central and endcap calorimeters. It should be noted that, unlike muons which passed through a full Geant simulation of the calorimeter, the passage of hadrons were simulated using the PCHTHR routine of Roger McNeil [3], which assumed iron as the absorber material and no magnetic field in the calorimeter.

Tracks leaving the calorimeter, which is a cylinder of radius 376 cm and of half length (along Z) 566 cm, were marked by hits placed at the front face of SL1. These dimensions include 10 cm of boron doped polyethylene for neutron shield and 6 cm of air for stay clear area, which were simulated by GEANT. Note that the endcap chambers in SL1 are assumed to be at Z=566, which makes their $|\eta|$ coverage limited to about 2.3

Fig. 5.3a shows the flux of charged particles (in Hz/cm^2) at SL1 as a function of rapidity. Unless otherwise stated, the rates are calculated for a luminosity of 10^{33} cm^{-2} s^{-1}. The turn-around at $|\eta|$=2.5 is due to excluding the tracks with polar angles smaller than the minimum angle covered by SL1 (about 10 degrees). This can be seen from Fig. 5.3b, which shows the charged particle flux as a function of the polar angle theta. The flux changes by more than two orders of magnitude between $|\eta|$=0.0 and $|\eta|$=2.5.

We further examine the rates, this time in terms of the particle composition. Fig. 5.4 shows the charged particle rate (in Hz) in the barrel and forward endcaps as a function of track ID (GEANT convention). Note that exiting particles are predominately electrons and muons. Electrons are always present and have a rather soft Pt distribution, indicating that they are produced in the last layer of calorimeter, hence leaking out. In this sense, additional absorber material will not help reduce the rate of exiting electrons.

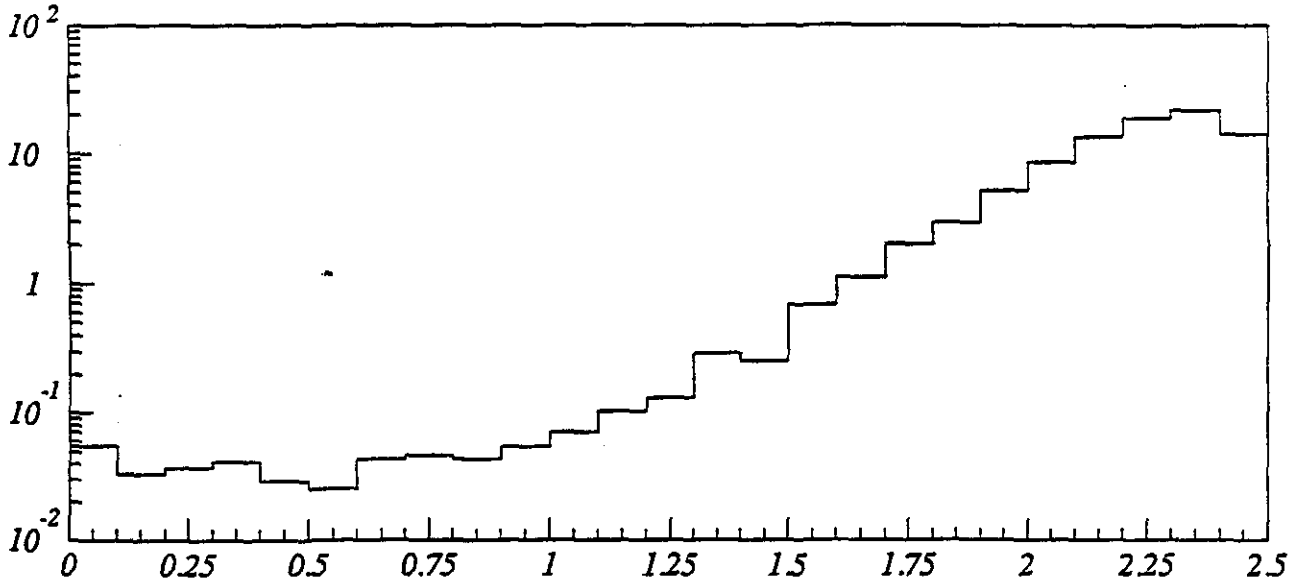

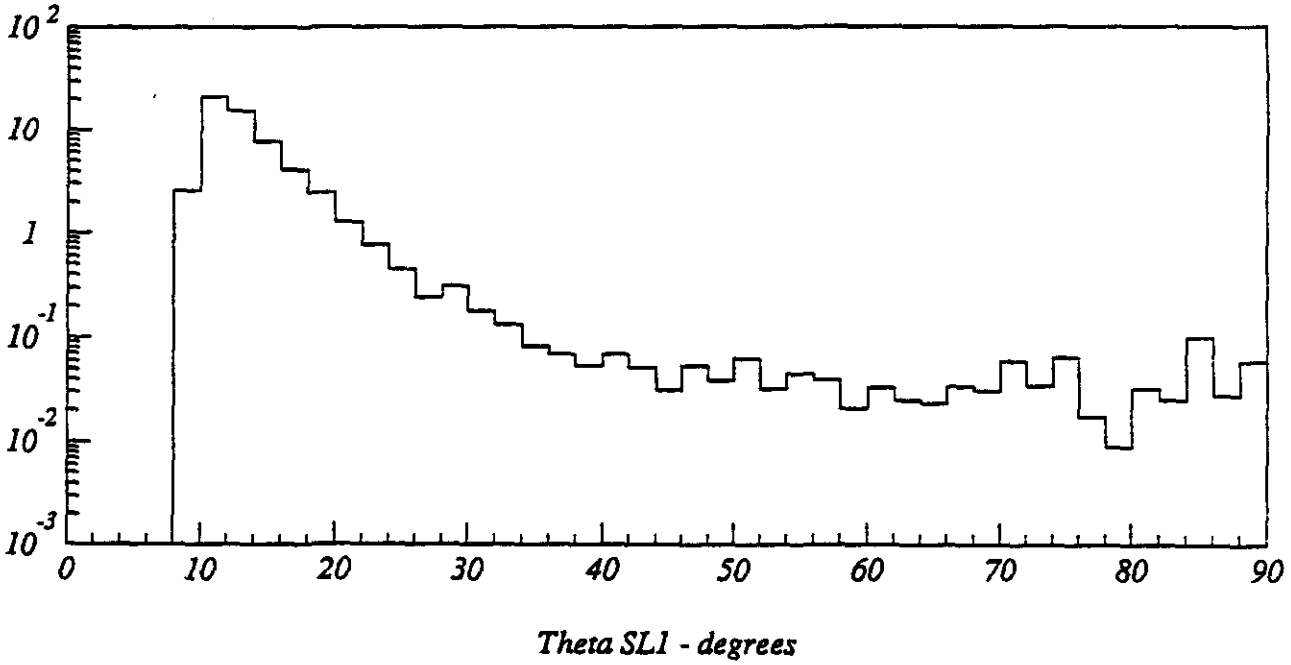

Fig. 5.3: **(a): Charged particle flux (Hz/cm^2) at SL 1 versus rapidity, (b): Charged particle flux (Hz/cm^2) at SL 1 versus polar angle theta(degrees). ($L=10^{33}cm^{-2}s^{-1}$)**

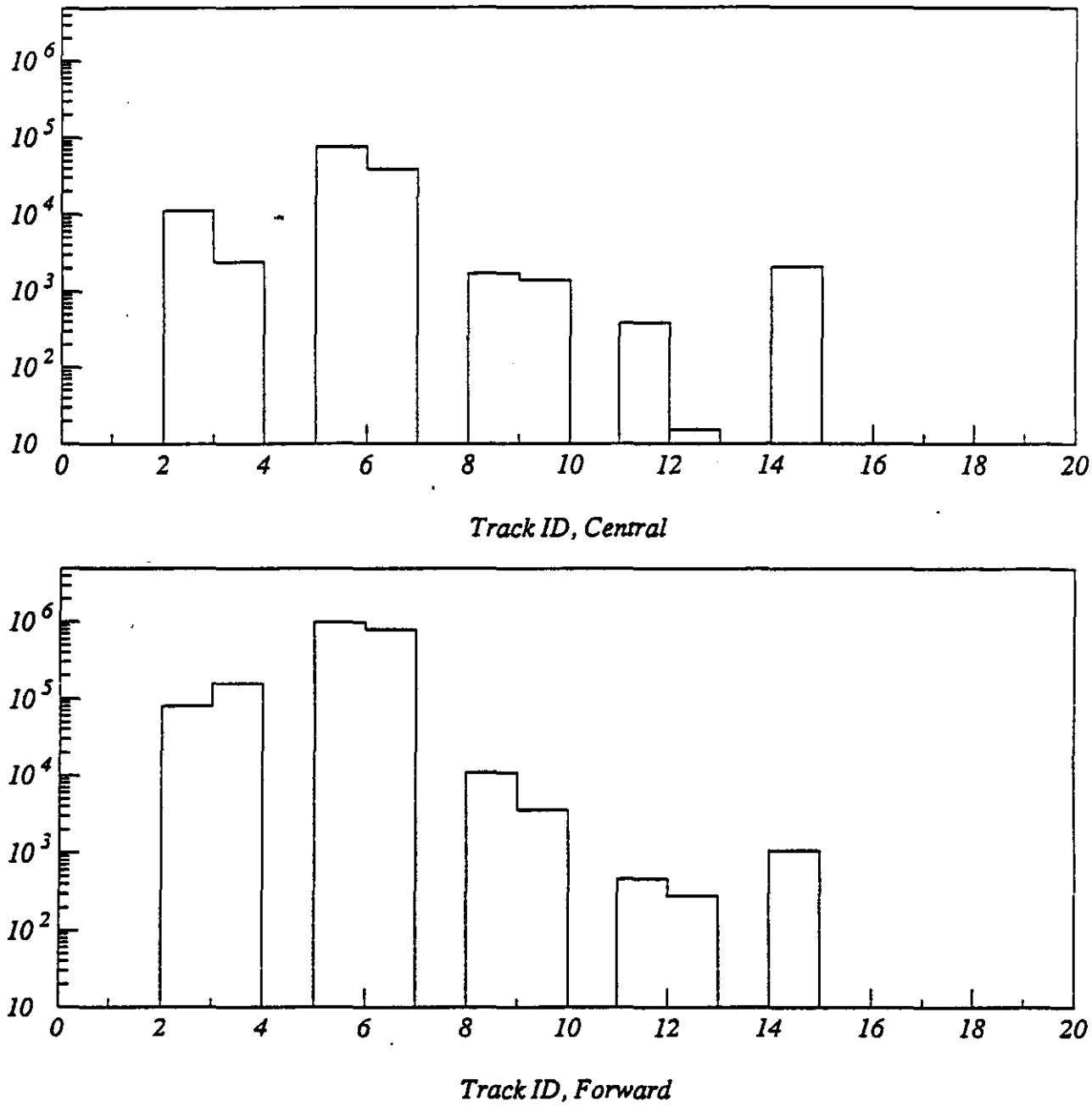

Fig. 5.4: **Charged particle rate (Hz) in the central barrel and forward endcaps versus track ID. The IDs are: 2 or 3 electrons, 5 or 6 muons, 8 or 9 pions, 11 or 12 kaons, and 14 or 15 protons. ($L=10^{33} cm^{-2} s^{-1}$)**

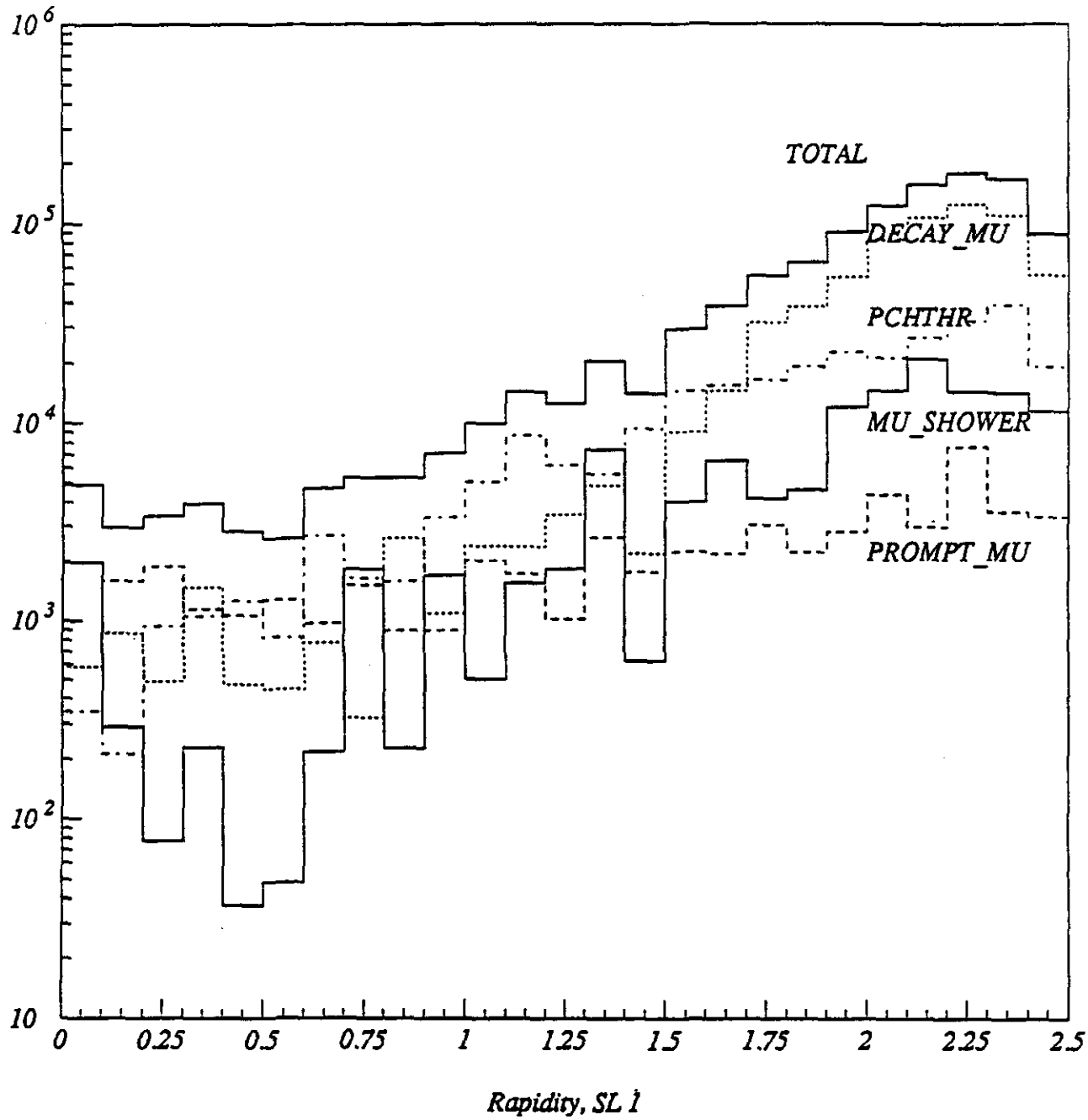

Fig. 5.5: **Charged particle rate (Hz) versus rapidity for decay muons, punchthrough particles, muon induced showers, and prompt muons. The total rate is also indicated. ($L=10^{33}cm^{-2}s^{-1}$)**

Next, we examine the rates in terms of the source of charged particles exiting the calorimeter. Fig. 5.5 shows the rate (in Hz) as a function of rapidity for prompt muons, decay muons, punchthrough particles (including secondary muons), and muon induced showers (excluding the muon itself). The total rate is also shown. Notice that the rapidity distribution of prompt muons is relatively flat, whereas the punchthrough rate increases steadily with increasing rapidity, and the decay rate increases very rapidly in the endcap region. The decay muons, owing to their momentum spectrum and the larger decay path available to pi/K mesons in the forward regions, dominate the total rate in the endcaps. In the barrel, the total rate has similar contributions from all sources.

Table 5.2.1 summarizes the occupancies calculated for a single strip of size typical of a Cathode Strip Chamber strip in the barrel and forward regions. The strip width is assumed to be 5 mm for all strips. **The luminosity assumed for these rates is 10^{34} cm^{-2} s^{-1}.**

Table 5.2.1. Chamber occupancy as a function rapidity.

REGION	BARREL		ENDCAP		
RAPIDITY BIN	0.0-0.8	0.8-1.3	1.3-1.8	1.8-2.1	2.1-2.3
CHARGED PARTICLE FLUX ($L = 10^{34}$ cm^{-2} s^{-1}) (Hz/cm^2)	0.4	0.8	8.6	55.0	161.6
STRIP SIZE (cm^2)	305x0.5	305x0.5	130x0.5	60x0.5	20x0.5
RATE PER STRIP (Hz)	61	122	559	1650	1616
SINGLE STRIP OCCUPANCY ($3X10^{-6}$ s delay)	0.02%	0.04%	0.2%	0.5%	0.5%

The Baseline 1 design requires a chamber occupancy of < 3% at this luminosity. The relevant number to consider may be the 3-, 5- or 7-strip occupancy, as a single particle may induce charge on a number of strips. From Table 1, the occupancies, even for "OR" of 7 strips, are well below the design value of 3% for chambers in the barrel. The endcap chambers have adequate occupancies for "OR" of 5 strips and slightly above 3% for "OR" of 7 strips. It has been pointed out [4] that further rate reduction with increasing the calorimeter depth beyond 14 lambda in the endcaps is not appropriate and cost effective; the chamber rate capability should be rather improved to insure its robustness at high luminosities.

5.3 Pattern Recognition for GEM Muon System

Pattern recognition capability in the muon system can be examined by studying the following two extreme cases which may cause problems in muon reconstruction and identification. The first case is muon-induced shower resulting from passage of energetic (~TeV) muons through the calorimeter material. Such high energy muons can be produced from decays of heavy Z' bosons of the TeV mass range. The second case is tagging of a b-quark from top decay by observing a relatively low Pt muon in a jet from the b-quark semileptonic decay. The muon trajectory has to be reasonably identifiable among other punch-through particles in the jet. In both cases we use the hit level Monte Carlo with the delta-ray generation threshold of 10 keV.

The degree of difficulty in muon pattern recognition can be measured by the amount of the unresolved overlapping tracks near a muon track. Here the definition of the double-hit resolution is the minimum distance between two hits for which the closeness of the hits does not affect the

spatial resolution. As described in other chapter, the double-hit resolution is estimated to be between 5 and 10mm. In the following studies, we use three double-hit resolutions of 6, 8 and 10mm to see how the double-hit resolution affects the pattern recognition problem.

In the studies, we use the number of planes, where the muon hit suffers overlap with another hit within the distance correponding to the double-hit resolution, as a measure of the pattern recognition capability of the muon system. Hereafter these planes will be called bad planes.

To study the first case, we generate single muons with fixed momentum of 1 TeV/c uniformly in space. Tables 5.3.1-3.2 summarize the probabilities of overlap as functions of the number of bad planes. Tables 5.3.1 and 5.3.2 are the cases where all superlayers and only superlayer1, respectively, are used.

An independent study using 1 TeV/c single muons with fixed incident angles was also done to see the difference in the effect of overlaps between 4-plane and 8-plane superlayer1. Table 5.3.3 summarizes the probabilities that there is one or zero good plane where only superlayer1 was used. The two independent studies agree (Tables 3.2 and 3.3).

For the second case of b-quark tagging, we generate top-antitop events with a top mass of 250 GeV/c^2. The b-quark from the top is forced to decay semileptonically into a muon. The pt range for top production is set to pt>50 GeV/c. A similar study to the one for high energy muons is done for the top-antitop events. Tables 5.3.4- 5.3.5 show the overlap probabilities as functions of the number of bad planes. Tables 5.3.4 and 5.3.5 are the cases where all superlayers and only superlayer1, respectively, are used.

The corresponding probabilities for the endcap are summarized in Tables 5.3.6- 5.3.9.

As clearly seen in Tables 5.3.1- 5.3.9, neither 1 TeV/c muons nor top-antitop events pose any serious problem for both the barrel and the endcap muon system as far as the pattern recognition is concerned.

Finally, the effect of finite double-hit resolution on the momentum resolution was also studied by considering a case where the spatial resolutions of all chambers in superlayer1 are worsened by a factor of "r" due to the double-hit. The result is summarized in Table 5.3.10 with and without an alignment error of half the point resolution, where the degree of the momentum resolution degradation is given in terms of a factor by which the momentum resolution degraded as compared to the original momentum resolution.

One of the techniques to resolve two nearby hits is to apply a moment method to the charge distribution on the trips. According to a study based on the moment method, the spatial resolution becomes about 400μm at the worst point due to double-hits (the distance bewteen two hits: 2-4mm), which is about a factor of 5.3 worse than the nominal design value of 75μm. If all eight muon hits in superlayer1 have 5.3 times worse spatial resolution due to double-hits, the momentum resolution is only degraded by a factor of 2. As we have already seen, this worst case scenario happens less than 2%(6%) of time for 1 TeV/c muons in the barrel (endcap). This worst-case degradation of the spatial resolution occurs only when the distance between two hits falls between 2 and 4mm. Outside this narrow region of separation the spatial resolution rapidly becomes smaller as the separation either increases or decreases. Therefore the effect of overlaps on the momentum resolution does not pose any serious problem.

Table 5.3.1 Overlap probability for barrel of single muon events (all superlayers)

# of bad planes	double-hit resolution		
(good)	6mm	8mm	10mm
0 (16)	.188	.181	.175
1 (15)	.334	.312	.309
2 (14)	.206	.197	.182
3 (13)	.123	.117	.132
4 (12)	.083	.083	.079
5 (11)	.043	.060	.051
6 (10)	.011	.011	.020
7 (9)	.011	.013	.022
8 (8)	.007	.011	.011
> 8 (<8)	.009	.016	.020

Table 5.3.2 Overlap probability for barrel of single muon events(only superlayer1)

# of bad planes	double-hit resolution		
(good)	6mm	8mm	10mm
0 (8)	.442	435	.430
1 (7)	.294	273	.267
2 (6)	.134	143	.135
3 (5)	.067	069	.070
4 (4)	.031	036	.042
5 (3)	.018	024	.024
6 (2)	.004	007	.014
7 (1)	.002	002	.004
8 (0)	.009	013	.014

Table 5.3.3 Overlap probability for barrel of single muon events (Only superlayer1) with one or zero good plane (4-plane and 8-plane superlayer)

			????			
# of planes	θ=90 deg		θ=60 deg		θ=15 deg	
	7mm	10mm	7mm	10mm	7mm	10mm
4	0.030	0.039	0.036	0.046	0.117	0.143
8	0.013	0.013	0.018	0.021	0.030	0.038

Table 5.3.4 Overlap probability for barrel of top events (all superlayers)

# of bad planes	double-hit resolution		
(good)	6mm	8mm	10mm
0 (16)	.217	.210	.207
1 (15)	.337	.314	.301
2 (14)	.223	.230	.210
3 (13)	.133	.139	.159
4 (12)	.052	.058	.068
5 (11)	.026	.026	.032
6 (10)	.003	.003	.010
7 (9)	.007	.003	.007
8 (8)	.003	.003	.003
> 8 (<8)	.000	.003	.003

Table 5.3.5 Overlap probability for barrel of top events (only superlayer1)

# of bad planes	double-hit resolution		
(good)	6mm	8mm	10mm
0 (8)	.460	.453	.434
1 (7)	.359	.333	.343
2 (6)	.120	.146	.142
3 (5)	.042	.032	.045
4 (4)	.010	.026	.013
5 (3)	.003	.003	.010
6 (2)	.003	.000	.007
7 (1)	.000	.000	.000
8 (0)	.003	.007	.007

Table 5.3.6 Overlap probability for endcap of single muon events (all superlayers)

# of bad planes	double-hit resolution		
(good)	6mm	8mm	10mm
0 (16)	.151	.151	.151
1 (15)	.227	.211	.195
2 (14)	.205	.216	.222
3 (13)	.157	.135	.130
4 (12)	.097	.081	.092
5 (11)	.043	.070	.043
6 (10)	.011	.022	.054
7 (9)	.032	.005	.000
8 (8)	.016	.027	.027
> 8 (<8)	.060	.081	.087

Table 5.3.7 Overlap probability for endcap of single muon events(only superlayer1)

# of bad planes	double-hit resolution		
(good)	6mm	8mm	10mm
0 (8)	.297	.292	.292
1 (7)	.281	.276	.243
2 (6)	.162	.146	.178
3 (5)	.092	.097	.081
4 (4)	.049	.049	.049
5 (3)	.032	.027	.027
6 (2)	.022	.027	.038
7 (1)	.005	.016	.016
8 (0)	.060	.070	.076

Table 5.3.8 Overlap probability for endcap of top events (all superlayers)

# of bad planes	double-hit resolution		
(good)	6mm	8mm	10mm
0 (16)	.436	.427	.411
1 (15)	.191	.178	.175
2 (14)	.178	.166	.156
3 (13)	.089	.092	.102
4 (12)	.051	.061	.061
5 (11)	.035	.035	.048
6 (10)	.010	.019	.013
7 (9)	.006	.010	.013
8 (8)	.000	.010	.016
> 8 (<8)	.003	.003	.006

Table 5.3.9 Overlap probability for endcap of top events (only superlayer1)

# of bad planes	double-hit resolution		
(good)	6mm	8mm	10mm
0 (8)	.567	.551	.535
1 (7)	.233	.220	.223
2 (6)	.112	.108	.092
3 (5)	.054	.064	.070
4 (4)	.019	.029	.038
5 (3)	.010	.013	.019
6 (2)	.000	.000	.006
7 (1)	.000	.006	.003
8 (0)	.006	.010	.013

Table 5.3.10 Dependence of momentum resolution degradation on worsening of superlayer1 spatial resolution

r =	1	2	3	4	5	6	7
without alignment error	1.00	1.13	1.32	1.54	1.78	2.04	2.32
with alignment error	1.00	1.08	1.19	1.34	1.50	1.69	1.88

5.4. Level 1 Muon Trigger

The level 1 muon trigger is based on a simple trigger logic using hits in superlayer2 (SL2) and superlayer3 (SL3). The logic is to measure the change of phi angle (dphi), which indirectly measures the curvature of a track if the track originates from the origin. dphi is measured in terms of a number of strips. In the following analysis, although the strip width for the endcap is fixed at 5mm, three trip widths (10, 15 and 30mm) are used for the barrel to study the effect of the strip width.

The actual procedure is described as follows:

Pick up a hit in SL2 and extrapolate the line formed by this point and the origin to SL3. The number of strips (Nstrip) between the strip hit by the extrapolated line and the nearest strip hit is the actual measure of dphi: the larger Nstrip, the smaller Pt of a track.

The trigger simulation is done using a simple geometry with three single plane superlayers, which have no material in the muon system.

In order to know the contributions from different parts of the muon system to the trigger rate, we divide the muon system into three parts: the barrel ($|\eta|<1.3$), endcap1 ($1.3<|\eta|<1.7$) and endcap2 ($1.7<|\eta|<2.4$).

For the trigger efficiency study, we generate single muons with fixed pt of 10, 20, 30, 40 and 50 GeV/c. QCD dijet events with jet pt range of 4 GeV/c to 1024 GeV/c are also generated to calculate the single muon trigger rates.

The trigger efficiencies for the barrel are calculated with the strip width of 10, 15 and 20mm, respectively, as functions of the minimum number of strips (Nstrip-min) for the luminosity of 10^{33} cm^{-2} sec^{-1}. Table 5.4.2.1 summarizes Nstrip-min which defines the trigger efficiency of >10%, >50% and >90% for each pt value together with corresponding trigger rates. Table 5.4.2.2 summarizes Nstrip-min for endcap1 and endcap2 which defines the trigger efficiency of >10%, >50% and >90% for each pt value together with corresponding trigger rate.

As the maximum allowed level 1 trigger rate is 10kHz, a pt cut at 20 GeV/c poses no problem. As the strip width increases for the barrel, the separation of pt=50 GeV/c from pt=40 GeV/c becomes almost impossible.

Table 5.4.2.1 Nstrip-min and corresponding rate for barrel for fixed trigger efficiencies

Strip width=10 mm

pt(GeV/c)	>10%		>50%		>90%	
	Nstrip-min	rate(kHz)	Nstrip-min	rate(kHz)	Nstrip-min	rate(kHz)
10	32	2.19	36	2.46	42	3.17
2	14	0.31	15	0.33	17	0.43
3	8	0.08	10	0.14	11	0.15
4	6	0.07	7	0.07	8	0.08
5	5	0.02	5	0.02	6	0.07

Strip width=15 mm

pt(GeV/c)	>10%		>50%		>90%	
	Nstrip-min	rate(kHz)	Nstrip-min	rate(kHz)	Nstrip-min	rate(kHz)
10	21	1.79	24	2.52	28	3.22
2	9	0.27	10	0.34	11	0.43
3	5	0.09	6	0.09	7	0.10
4	4	0.03	5	0.09	5	0.09
5	3	0.02	4	0.03	4	0.03

Strip width=20 mm

pt(GeV/c)	>10%		>50%		>90%	
	Nstrip-min	rate(kHz)	Nstrip-min	rate(kHz)	Nstrip-min	rate(kHz)
10	11	2.40	12	2.67	14	3.22
2	4	0.25	5	0.30	6	0.53
3	2	0.03	3	0.10	4	0.25
4	2	0.03	2	0.03	3	0.10
5	1	0.01	2	0.03	2	0.03

Table 5.4.2.2 *Nstrip-min and corresponding rate for endcap for fixed trigger efficiencies*

Strip width=5 mm
Endcap1

pt(GeV/c)	>10%		>50%		>90%	
	Nstrip-min	rate(kHz)	Nstrip-min	rate(kHz)	Nstrip-min	rate(kHz)
10	30	0.29	40	0.56	50	0.99
2	5	0.07	18	0.13	22	0.21
3	9	0.02	12	0.07	14	0.07
4	7	0.01	.02	11	0.02	
5	5	0.01	.01	8	0.01	

Endcap2

pt(GeV/c)	>10%		>50%		>90%	
	Nstrip-min	rate(kHz)	Nstrip-min	rate(kHz)	Nstrip-min	rate(kHz)
10	15	0.68	18	1.03	21	1.53
2	7	0.23	9	0.30	11	0.47
3	5	0.22	6	0.22	7	0.23
4	3	0.01	4	0.05	5	0.22
5	3	0.01	4	0.05	4	0.05

5.5 Neutron sensitivity

Studies of response of a CSC to neutrons were done by Jim Shank and Scott Whitaker at MIT in Louis Osbourne's lab on May 11 and 12, 1992. The neutron source was 0.1 curies of ^{252}Cf; the source was at the bottom of a 30 cm deep, 10 cm diameter counterbore in a 30 cm-radius cylindrical borated polyethylene holder. The average neutron energy was 2.35 MeV, with a broad peak from 0 to 2 MeV and a long tail at higher energies. Total neutron production, calculated from the source activity, was 1.428×10^8 n/sec (plus lots of photons!). Details of the neutron spectrum are given in the GEM Note by the MIT group reporting their results with LSDTs (GEM Note TN-92-122).

The CSC used in the source test is shown in figure 5.4. All 60 anode wires were ganged and read by a BNL IO323 preamp followed by an Ortec 460 amplifier; unipolar signal shaping was used, with pulse width of approximately 1 μsec. For these tests the operating voltage was 2500 V. The observed gas gain was ~ 1,000 as shown in figure 5.5. Signals were discriminated at 100 mV, corresponding to a threshold of approximately 2 KeV.

The detector sat on lead bricks that covered much of the top of the source holder, the active volume was 24 cm above the top of the holder, so 54 cm above the source. The full active area of 150 cm^2 was illuminated. From this geometry, the neutron flux was calculated to be 0.57×10^6 n/sec through the unshielded detector. The detector position was fixed an absorbers were inserted between it and the source.

Figures 5.6 and 5.7 show the rate vs HV for no absorber and for 4" Pb followed by 2" polyethylene. Figure 5.8 shows the count rate vs HV when the detector was exposed to 6 KeV x-

rays from ^{55}Fe at BU; gives signals somewhat larger than those from muons. The stretched out plateau curves and the gain data from figure 5.5 show that the pulse heights for the source cover a much broader range than the 55Fe and in particular that there are a lot of very energetic interactions that give count rate even at low gas gain.

Figure 5.9 shows the count rate vs thickness of lead absorber interposed between the source and the detector. The data were fit with Minuit to a sum of two exponentials. One component, presumably photons, accounts for 2/3 of the count rate; the attenuation coefficient of 0.84 cm^{-1} in lead corresponds to photon energies of ~ 1 MeV, which is consistent with the flux expected from the source. The other component, 1/3 of the count rate, is attributed to neutrons. The second attenuation coefficient of 0.128 cm^{-1} gives a cross section of 3.9 per Pb atom. This can be compared with the cross section of 5.6b for neutrons in Pb, averaged over a fission neutron spectrum (Kaye and Laby, p. 430). This is the total cross section, almost all due to elastic scattering. The measured cross section is smaller possibly due to neutrons being scattered but still traversing the detector.

From the neutron count rate of 2,670 Hz for the unshielded detector (determined from the fit, figure 5.9) and the calculated neutron flux of 0.57 × 106 n/sec through the detector, the detector has a neutron detection efficiency

$$s_n = 4.7 \times 10^{-3}.$$

The neutron efficiency per cm of path length in the gas is 9.4×10^{-3} cm^{-1}. The neutron count rate per cc of gas is 2,670 Hz/75 cm^3 = 36 sec^{-1} cm^{-3} with no shielding, 54 cm from the source.

From the neutron efficiency we can calculate an effective cross section per gas molecule, assuming the neutron counts are due to interactions in the CO_2 and CF_4. From $s_n = Nx\sigma$, where N is the density of molecules and x is the detector thickness, we find σ =350 barns. This is much larger than the average neutron cross section determined from the fission-spectrum cross sections for C(2.4 b), o(2.8 b) and F(6 b) (cross sections for C and O are from Kaye and Laby, and for F from Louis Osborne's borrowed big book...). Those values give σ (CO_2) = 8 b and σ (CF_4) = 26 b, for an average σ = 17 b. An alternative way of looking at this is that the expected cross section of 17 b would give a neutron detection efficiency of 2.3 10^{-4} rather than the observed 4.7 10^{-3}. The count rate is 20 times larger than would be expected on the basis of fission-spectrum neutrons interacting in the chamber gas.

It is possible that the detector is responding to photons that arise from neutron interactions in the chamber walls, frame, or supports, or that neutron interactions there are knocking ionizing particles into the chamber. Calculations are under way at LLNL (C. Wuest) to study this contribution. Further measurements with sources and different detector configurations will be done as well.

Finally, Figure 5.10 shows the count rate for different arrangements of lead and polyethylene shielding bricks. Neutrons interacting in the polyethylene produce photons that are counter in the chamber; placing lead after the polyethylene knocks down that source of counts.

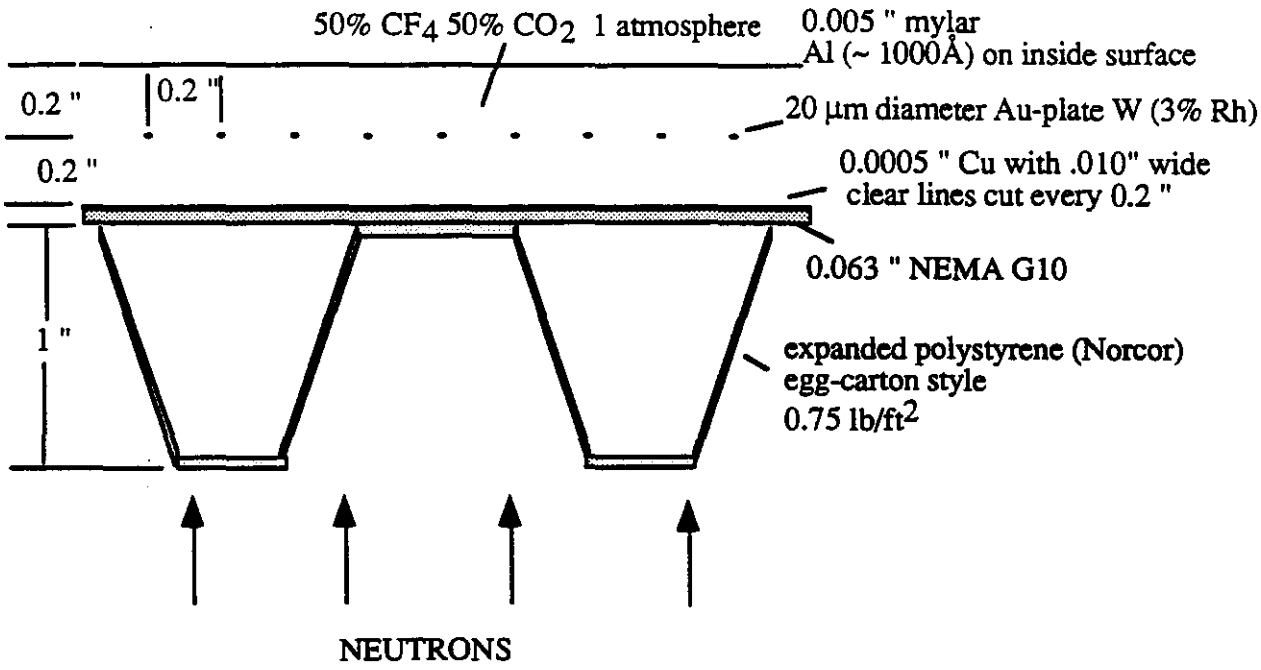

Fig. 5.4 Test chamber layout

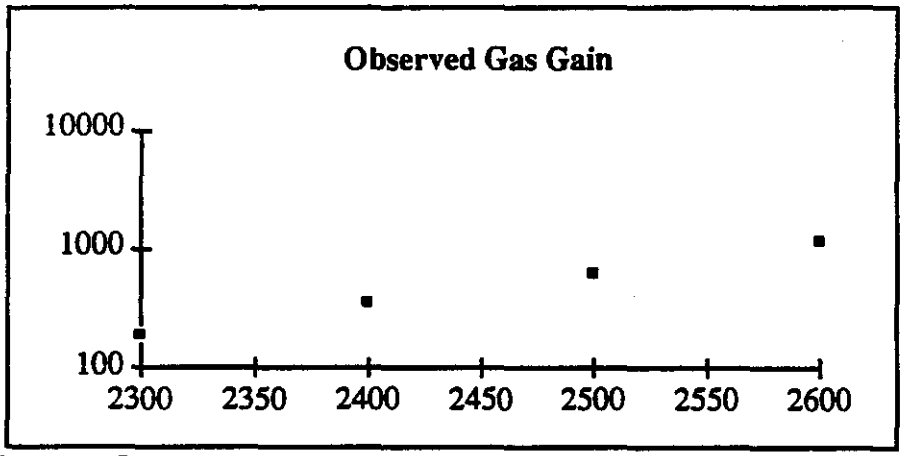

Fig. 5.5 Observed gas gain vs. voltage, for 50% CO_2, 50% CF_4

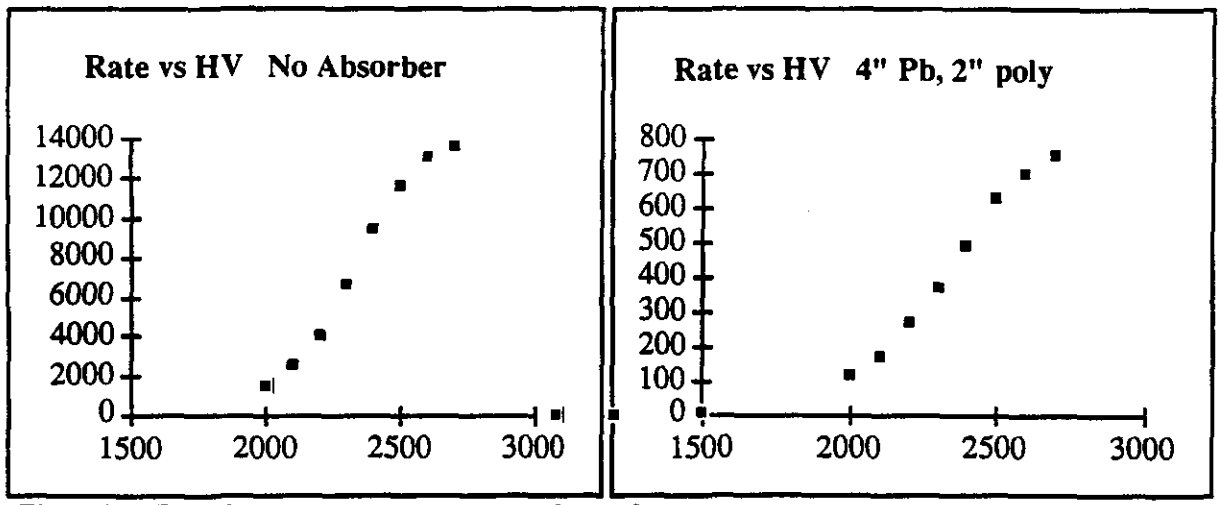

Fig 5.6, 5.7. Plateau curves: rate vs voltage for detector exposed to the neutron source.

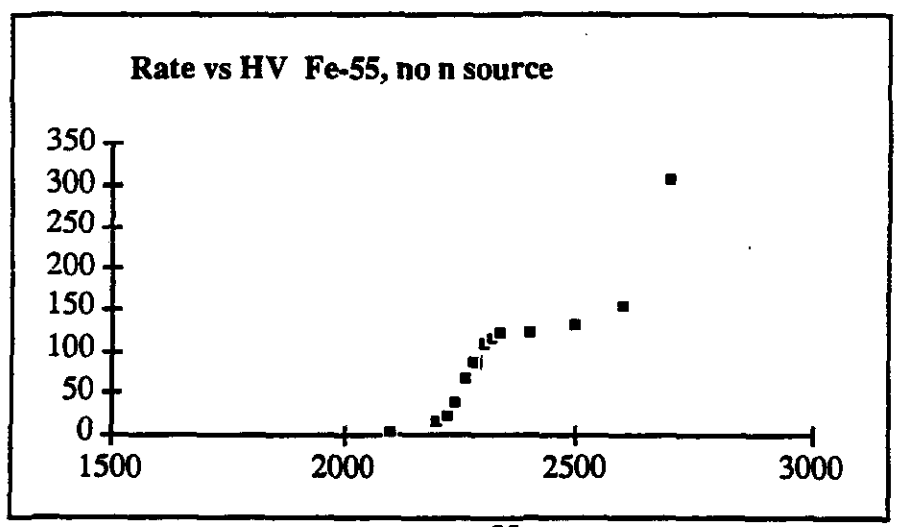

Fig. 5.8 Plateau curve: rate vs voltage for ^{55}Fe x-rays, no neutron source.

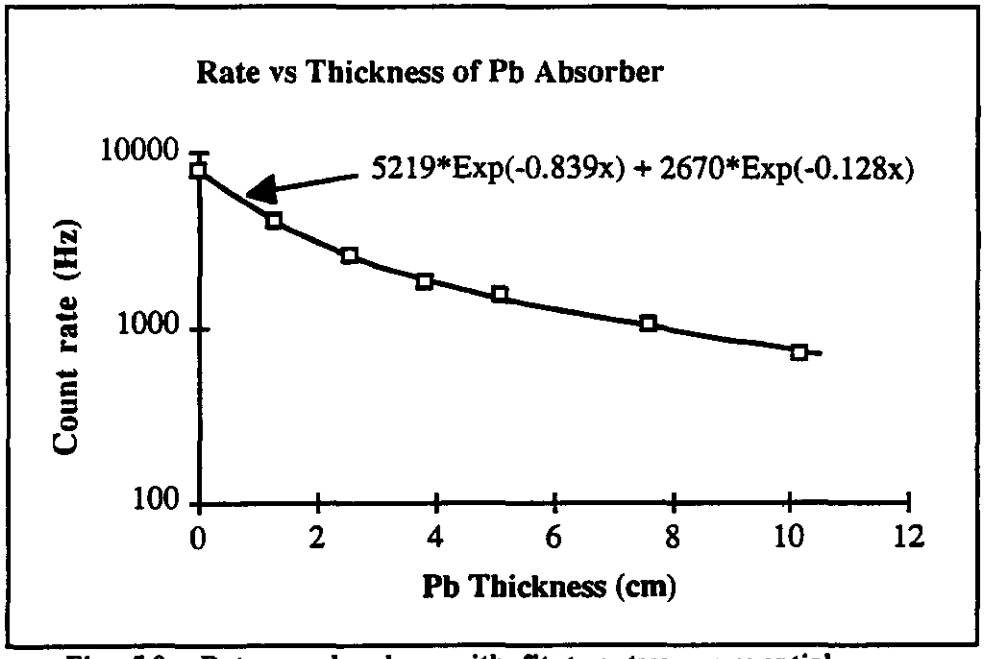

Fig. 5.9 Rate vs absorber, with fit two two exponentials.

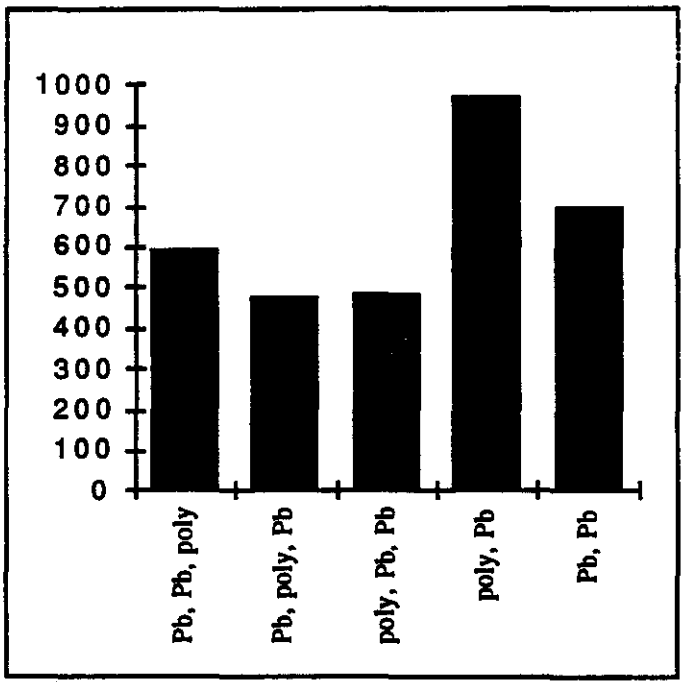

Fig. 5.10 Rate vs ordering of shielding. Two inch bricks of lead and/or polyethylene were placed between the open source and the CSC (whose position was fixed). Ordering of the absorbers is bottom (near the source) to top (near the detector).

References

[1] List of contributors to this Chapter:
Mohammad Mohammadi, Stony Brook
Andrey Ostapchuk , SSCL
Jim Sullivan, MIT
Valerie Tcherniatin , BNL
Scott Whitaker, Boston University
Aki Yamashita, BNL
Chiaki Yanagisawa, Stony Brook

[2] GEM Baseline 1, GEM TN92-76, April 23, 1992.

[3] R. McNeil, "PCHTHR — a fast simulation for hadron punchthrough," GEM TN-92-193.

[4] M. Mohammadi, in GEM TN-92-131, July 8, 1992.

6. Manufacturing

6.1 Technological Process

The key element in CSC production is the industrial production of the laminated panels that are faced with the precision cathode boards. WE discuss at the end of this section progress and prospects for mass production of boards of suitable size and precision. Once these boards are made the remainder of the production process relies on well-established MWPC production techniques, with only a few steps requiring precision fixturing. We list below the major steps in the production process, for the barrel CSC's, in which conceptual design is shown in Fig 2.8, 2.9 and 2.10, and illustrate it schematically in Figure 6.1.

The CSC mass-production technological chain includes following processes:

1. Fabrication of components in industry:
   - stripped cathodes laminated on honeycomb panels,
   - precise thickness bars for the chamber frames,
   - printed circuit boards
2. Purchase various materials and components:
   - gold plated tungsten wire enforced with rhenium,
   - signal connectors,
   - gas connectors,
   - glues, O-rings etc.,
   - capacitors, resistors, etc.
   - others
3. Shipping components and materials to chamber production facility
4. Fabricate parts in general purpose facilities in-site
5. Component acceptance control.
6. Assemble precise positioning monitors on the panel. This operation transfers precise fiducial marks on stripped electrode (internal marks) to positioning monitors (external marks), which are used as references in operation 22.
7. Drill holes in the panels
8. Assemble gas outlets
9. Glue chamber frames to the panels
10. Glue PC boards to the chamber frames
11. Assemble spacers on the panels
12. Assemble resistors on the stripped electrodes
13. Clean cathodes and chamber frames
14. Wind wire areas on transfer frames
15. Wire tension control
16. Cleaning wires

17. Transfer wires from transfer frames to the chamber frames
18. Wire tension control
19. Clean the electrodes
20. Electrode acceptance test
21. Final cleaning of electrodes
22. Assemble and closing the chamber
23. Assemble exterior mechanical parts
24. Assemble ground conductors, signal and HV connectors etc.
25. Flush chambers with gas
26. Chamber HV training
27. Chamber acceptance test
28. Complete test with cosmic rays
29. Storage
30. Crate chambers
31. Safe-keeping
32. Shipping to SSC
33. Acceptance test after shipping
34. Assemble front end electronics
35. Assemble chambers in superchambers if necessary
36. Assemble chamber parts of alignment system
37. Cabling
38. Complete test before assembly into sectors
39. Assemble chambers into sectors
40. Adjustment of alignment system
41. Final test

Specialized equipment or facilities are needed for the following operations:

- Operations 6, 7 require temperature controlled room
- Operations 6,7,8,9,10,11 require special jigs
- Operation 14 require automatically controlled wiring machinery
- Operations 13-22 require clean area
- Operation 22 requires special jigs and tools and should be carried out in a clean temperature controlled area

The total estimated area required for operations 5-28 is approximately 1200 sq. meters

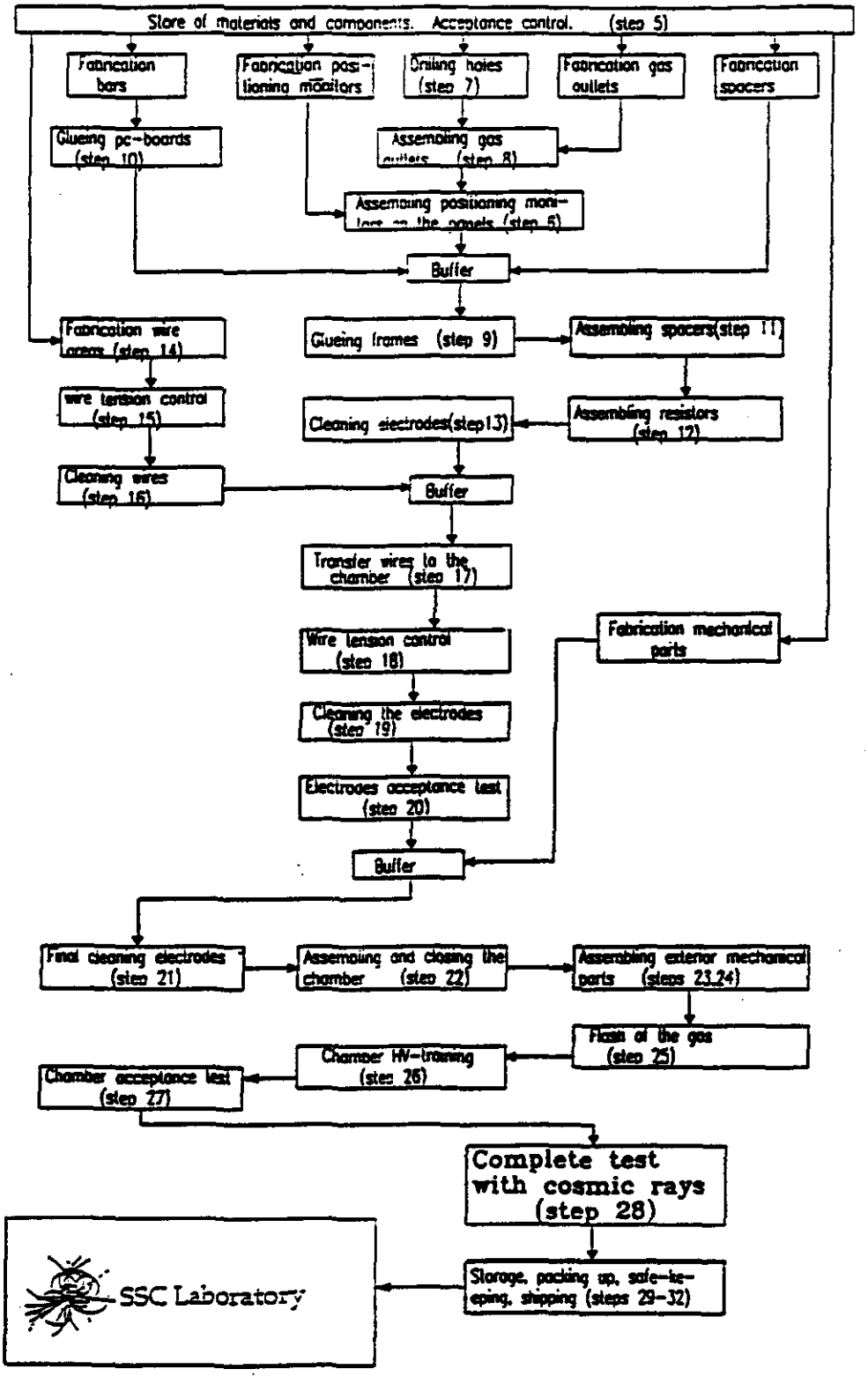

Figure 6.1 CSC Mass—Production Technological Chain

Manpower needed to manufacture barrel CSC's in which conceptional design is shown in Fig 2.8, 2.9, and 2.10 with a rate of 200 per year (4 per week + 25% contingency) is listed below.

Operation 5	2 persons
Operation 6	3 persons
Operation 7	4 persons
Operation 8	1 person
Operations 9-11	7 persons
Operation 12	6 persons
Operation 13, 16	2 persons
Operation 14	3 persons
Operation 15, 18	2 persons
Operation 17	8 persons
Operations 19-22	6 persons
Operation 23	2 persons
Operation 24	2 persons
Operations 25-28	3 persons
Operations 29-32	2 persons
Total	**53 persons**

6.2 Cathode Prototype Program

The objective of the program is to establish the ability to manufacture parts that can be built into CSC chambers of the optimum size for GEM with adequate precision and tolerance. The specific parts to be manufactured are panels that have copper circuits on both faces. The panels will be very stiff and as light as possible. The circuits will be different for the two faces: one face will have accurate, narrow strips running the long direction of the face and the other will have broader strips of less accuracy running across the narrow direction (or possibly only blank copper with no strips). The physics requirements for the chambers require the long, narrow strips to be placed accurately to with 50 microns in any dimension transverse to the long or bending direction dimension of the panels. The 0.2 mm gap between adjacent strips must be accurate to the same tolerance. Fiducials that are visible from outside of the finished chambers must be provided that are accurately located with respect to the strips. The other major constraint on the panel is that the face bearing the accurate strips must be flat to the same 50 microns. This is a measure of the need for the "cell" within the chamber to be of a constant dimension. The working definition of this is that an accurate straight-edge of about one meter length will not be farther away from the surface than the 50 microns. The remainder of the panel construction involves a light weight core of material like paper honey-comb and edge sealing frames the help with stiffness and provide material for attachments.

The geometry of the muon system and likely support structure schemes leads to a preference for chambers with widths, in the bend direction, that approach 1.75 meters. The same realities also lead to a preference for chambers to be up to 4 meters long. The initial contacts with industry indicate that there are limitations in both of these directions that could make it difficult to achieve these dimensions. The purpose of the prototype program is to determine the dimensional range over which we can manufacture these panels meeting the physics limitations.

There are at least two competing technologies available for creating the circuit strips on the faces and at least two others for laminating the honey-comb filled panels to the faces. We are trying to establish a sensible matrix of prototypes that will allow us to choose the best combination of technologies for producing panels. It is proposed that we follow a panel manufacturing technique that uses very flat vacuum tooling to hold the faces as flat and as accurately spaced as possible while the adhesive bonding them to the core and frame materials is setting up. We expect to procure an immediate panel from MC Gill Co. in the next few months for initial evaluation of this vacuum chuck system and their adhesive system. The evaluation criteria would be the resultant surface conditions of the faces and the stability of the mini-panel. This would be followed with a development contract to MC Gill to create the necessary tooling to produce full sized panels.

The circuit manufacturing techniques available are the classical metal removal techniques and the newer metal addition technique. Both techniques are limited by the optical master that is used to expose the photo-resist material prior to metal removal or addition. The available sizes and accuracy' of the machines that make these optical masters must be followed down both paths. Buckbee Mears has provided some small prototypes to BNL and will provide an initial prototype of the barrel configuration. It will be as large as they can manufacture with existing capabilities and will be evaluated for dimensional accuracy. Another manufacturer that adds copper will provide a similar board. The additive process will also be evaluated for strip thickness, resistivity and strip to strip resistivity and will then be asked to provide the largest possible face with their existing equipment. The most attractive current concept is to have MC Gill produce a panel with blank faces and have the copper additive people add the circuits.

Faces that have been manufactured by both processes will be butt joined to manufacture panels of the final desired dimensions. These will be used to prove out chamber construction techniques and provide a working chamber that can be tested for performance limitations other than precison of the boards themselves. Based on the experience with these initial prototypes, final optimization of the process and sizes of the chambers will be determined. It is expected to have a full scale prototype of the largest barrel chamber produced with final technology within a year.